Development of electrochemical sensors for sensing of Dopamine

Dissertation

der Mathematisch-Naturwissenschaftlichen Fakultät

der EBERHARD-KARLS-UNIVERSITÄT Tübingen

zur Erlangung des Grades eines

Doktors der Naturwissenschaften

(Dr. rer. nat.)

Vorgelegt von

Tanja Martin

Tübingen

2017

Gedruckt mit Genehmigung der Mathematisch-Naturwissenschaftlichen Fakultät der Eberhard-Karls-Universität Tübingen.

Tag der mündlichen Qualifikation:	07.06.2018
Dekan:	Prof. Dr. Wolfgang Rosenstiel
1. Berichterstatter:	Prof. Dr. Boris Hofmann
2. Berichterstatter:	Prof. Dr. Tilman Schäffer

Ich erkläre hiermit, dass ich die zur Promotion eingereichte Arbeit mit dem Titel: „Development of electrochemical sensors for sensing of Dopamine“ selbständig verfasst, nur die angegebenen Quellen und Hilfsmittel benutzt und wörtlich oder inhaltlich übernommene Zitate als solche gekennzeichnet habe. Ich erkläre, dass die Richtlinien zur Sicherung guter wissenschaftlicher Praxis der Universität Tübingen (Beschluss des Senats vom 25.05.2000) beachtet wurden. Ich versichere an Eides statt, dass diese Angaben wahr sind und dass ich nichts verschwiegen habe. Mir ist bekannt, dass die falsche Abgabe einer Versicherung an Eides statt mit Freiheitsstrafe von bis zu drei Jahren oder mit Geldstrafe bestraft wird.

Tübingen, den 08.06.2018 Tanja Martin

I. Contents

II. Abstract

In this thesis the development of an electrochemical sensor for sensing of Dopamine on the basis of redox cycling was pursued. A 3-dimensional, plane-parallel electrode array was designed, consisting of bottom and top electrodes, where pores provide a spatial confinement and electrode interface to the measurement solution. In a micromechanical bottom-up process, a multi-layered formation of electrically conducting gold structures and insulating silicon nitride passivation was created by optical lithography, vapor deposition and plasma-enhanced chemical vapor deposition. Pore-channels of 5 µm diameter were opened by reactive ion etching. The produced sensors were evaluated by redox-cycling measurements on potassium hexacyanoferrate via cyclic voltammetry and amperometry. Stable sensors could be produced with an inter-electrode distance of 300 and 400 nm and were further evaluated by amperometric measurements in a fluidic setup, investigating the temporal and spatial resolution on concentration-changes of dopamine in solution. The electrode fouling process of dopamine on gold electrodes could be shown for a concentration of 1 mmol/l dopamine. Repetitive potential switches between oxidative and reductive potential could not initiate a reversal of the process. For an in-vitro evaluation of the produced sensors dopaminergic PC12 cells were cultivated on the sensor surface and the release of physiological dopamine by the cells was induced by potassium chloride and dopamine. The designed sensor could be evaluated to a sensitivity for dopamine of 10 µmol/l, a fast response time and a cycling efficiency larger than 84 %. To further enhance the sensitivity, a modification towards smaller pores was done by nanosphere lithography. Polystyrene nanospheres of 500 nm diameter were deposited on the sensor by spin-coating and air-water-interface self-assembly and served as a shadow mask for the pore etching. Pore structures in the range of 202 nm and 141 nm mean pore diameters could be created. For the modification towards a flexible sensor array, the existing design was transferred to a polymer-based insulation and substrate material by exchanging silicon nitride with polyimide, resulting in a functioning flexible electrode array embedded in polyimide.

III. Zusammenfassung

Die Entwicklung eines elektrochemischen Sensors für die Erfassung von Dopamin durch Redoxcycling ist die wissenschaftliche Zielsetzung dieser Arbeit. Ein dreidimensionales, planparalleles Elektrodenarray wurde designt, bestehend aus einer Boden- und Top-Elektrode, wobei Poren eine räumliche Eingrenzung und Grenzfläche zwischen Elektrode und Messlösung herstellen. In einem mikromechanischen Bottom-Up-Prozess wurde ein mehrlagiger Aufbau aus elektrisch leitenden Goldstrukturen und isolierender Siliziumnitrid-Schicht mittels optischer Lithografie, Gasphasenabscheidung und Plasmaverstärkter-Chemischer-Gasphasenabscheidung hergestellt. Porenkanäle von 5 µm Durchmesser wurden durch Reaktives Ionenätzen geöffnet. Die hergestellten Sensoren wurden durch Redoxcycling-Messungen an Kaliumhexacyanidoferrat(II) mittels zyklischer Voltammetrie und Chronoamperometrie evaluiert. Stabile Sensoren konnten mit einer Zwischenpassivierung von 300 und 400 nm hergestellt werden und wurden weiter durch Messungen in einem Fluidik-Versuchsaufbau auf die zeitliche und räumliche Auflösung der Reaktion auf veränderliche Konzentration von gelöstem Dopamin bewertet. Der Prozess des Elektroden-Foulings von Goldelektroden durch Dopamin konnte an 1 mmol/l Dopaminlösung gezeigt, jedoch durch wiederholten Potentialwechsel zwischen Oxidations- und Reduktionspotential nicht rückgängig gemacht werden. Um eine Bewertung produzierter Sensoren in in-vitro-Bedingungen vornehmen zu können, wurden Dopamin-produzierende PC12-Zellen auf dem Sensor kultiviert und die physiologische Ausschüttung von Dopamin durch die Zellen mittels Kaliumchlorid und Dopamin ausgelöst. Für den entwickelten Sensor konnte eine Nachweisgrenze für Dopamin von 10 µmol/l, eine schnellen Reaktionszeit und eine Cycling-Effizienz größer 84 % bestätigt werden. Um die Sensitivität des Sensors weiter zu erhöhen wurde eine Modifikation hin zu kleineren Porendurchmessern mittels Nanosphären-Lithographie vorgenommen. Polystyrol-Nanosphären von 500 nm Durchmesser wurden durch Aufschleudern und Grenzflächen-Selbstanordnung auf die Sensorfläche aufgebracht und dienten als Schattenmaske für das Porenätzen. Porenstrukturen zwischen 202 und 414 nm im Mittel konnten hergestellt werden. Für eine Modifikation hin zu flexiblen Sensoren wurde das bestehende Design auf ein polymerbasiertes Isolations- und Verkapselungsmaterial überführt durch den Austausch von Siliziumnitrid durch Polyimid und ein funktionierendes flexibles Elektroden-Array hergestellt.

IV. List of Abbreviations

A

AWISA: Air-Water-Interface-Self-Assembly 49

B

BioMEMS: Bio microelectromechanical system 1

C

CAD: Computer assisted design 37
CCD: Charge-coupled device 48
CE: Counter electrode 12
CV: Cyclic Voltammetry 19
CVD: Chemical vapor deposition 31

D

DA: Dopamine 10
DAC: Dopaminechrome 10
DAQ: Dopamine-o-quinone 10
DBS: Deep Brain Stimulation 6
DMEM: Dulbecco`s Modified Eagle Medium 46

F

FIB: Focused ion beam 51
FSCV: Fast-scan cyclic voltammetry 21

G

GPi: Globus pallidus internus 8

H

HCP: Hexagonally close-packed 34
HF: High frequency 30
HIM: Helium-Ion-Microscopy 64
HMDS: Hexamethyldisilazane 37

I

IBE: Ion beam etching 33
IDA: Interdigitated array 23
IHP: Inner Helmholtz plane 17
IPA: Isopropyl alcohol 38

L

LISA$^+$: Center for Light-Matter Interaction, Sensors & Analytics 37

M

MEA: Multi electrode array 23
MEMS: Microelectromechanical system 1
MIBK: Methyl isobutyl ketone 51
MRI: Magnetic resonance imaging 8

N

NA: Numerical aperture 30
NS: Nanospheres 48
NSL: Nanosphere lithography 33

O

OHP: Outer Helmholtz plane 17

P

PBS: Phosphate buffered saline 44
PD: Parkinson`s Disease 5
PDMS: Polydimethylsiloxane 25
PECVD: Plasma-enhanced chemical vapor deposition 31
PPX: Polyparaxylene, Parylene 25
PS: Polystyrene 48
PVD: Physical vapor deposition 30

R

RE: Reference electrode 12
RF: Radio frequency 39
RIE: Reactive ion etching 31
rpm: Rounds per minute 37
rps: Rounds per second 106

S

SEM: Scanning electron microscopy 33
SiC: Silicon carbide 131
SLPM: Standard liter per minute 39

V. List of Symbols

Symbol	Unit	Description
A	cm^2	Area
Å	m	Angstroem (10^{10} m)
AC	A	Alternating current
C_d	F	Capacity
c	mol/l	Concentration
C_0	mol/l	Concentration at t=0
D_0	cm^2/s	Diffusion coefficient
E	V	Potential
f	Hz	Frequency
F	C/mol	Faraday constant
F_c	N	Capillary forces
F_d	N	Hydrodynamic force
h	m	Height
I	A	Current
J_s	m/s	Hydrodynamic flux
k^0 ; k_S	-	Standard transfer rate constant
k_1	-	Imaging technology constant
M	g/mol	Molecular weight
M		Molar, concentration [mol/l]
n	-	Number of charge transferred
ŋ	V	Overpotential
Ŋ	-	Cycling efficiency
O	-	Oxidized species
R	-	Reduced species
R	Ω	Resistance
R	J/mol·K	Gas constant (8.3144598 J/mol·K)
R	m	Rayleigh diffraction, optical resolution
T	°C	Temperature
t	s	Time
V	V	Voltage
v	V/s	Velocity, Sweep rate
Z_w	Ω	Diffusion impedance (Warburg)

1 Introduction

"As long as our brain is a mystery, the universe, the reflection of the structure of the brain, will also be a mystery." Santiago Ramon y Cajal

To solve a mystery has been the fundamental driving force for all scientific endeavors. In medical sciences, the curiosity for the workings of the body is paired with the need to repair and cure. Since the rise of modern medicine, science and technology, astonishing progress in medical technology has been achieved. Organs can be transplanted, even grown in a lab, be paired with or replaced by artificial implants like heart valves, artificial spinal disks or complete joints. Even the most complex organs like the eye can be repaired by active neuronal implants, which translate signals, bypassing the defect structure [1] and hearing can be restored by cochlear implants [2]. The brain, more inaccessible as it is the control center of the entire body and the most complex organ, has been slow to reveal its structural functionality and investigations mainly rely on external imaging technologies and a cure for neurological diseases is mostly founded in pharmacological treatment. With the successful establishing of the invasive technology of Deep Brain Stimulation, where a neurostimulator is permanently implanted in the brain and an electrical current is applied to the target region, diseases like Parkinson`s, Tourette Syndrome, Epilepsy and Dystonia can effectively be alleviated [3]. For Parkinson`s disease as the second most common neurodegenerative disease after Alzheimer`s disease [4], a direct correlation between symptoms and neurotransmitter concentration could be established [5]. Next to the electrical signaling, the biochemistry of the brain is of paramount importance for understanding the functioning of the brain, were neurotransmitters are the chemical communication system. Many neurotransmitters like Dopamine, Serotonin, Epinephrine and Norepinephrine are electro-active and undergo electron-transfer reactions, which can be used to infer the concentration by the electrical current induced [6].

Progress in microfabrication technology has made microelectromechanical system (MEMS) devices an attractive tool for electrical and chemical investigation and a wide field of devices and research areas has developed around microelectrodes and their use in diagnostics, drug delivery, minimally invasive surgery or neuro prosthesis. One of the most successful applications is the Blood Glucose Monitor, a BioMEMS utilizing a chemical reaction to induce an electric current for measurement of the amount of glucose in a blood sample. [7]

The current application of Deep Brain Stimulation is an open-loop stimulation without feedback from the underlying brain activity and the success is measured by the alleviation of motor symptoms. In 2012, the first real-time concentration measurement of Adenosine during a DBS implantation surgery was performed [8]. In the ongoing attempt to create a closed-loop, feedback driven neurochemical monitoring and stimulation system, successful developments could be made with a wireless instantaneous neurotransmitter concentration system device (WINCS) [9] and a responsive neurostimulator for treatment of epilepsy, which induces stimulation prior to a seizure to prevent its onset [10]. To further the progress of intelligent closed-loop DBS, not only to optimize the electrode placement, but to help understand the functioning of brain on a biochemical level by measuring change in brain chemistry, stable, implantable, smart electrode systems are needed.

Therefore, the objective of this thesis was the development of an electrochemical sensor for sensing of Dopamine on the basis of redox cycling. A 3-dimensional electrode array was designed, containing a bottom and top electrode, where pores provide a spatial confinement and electrode interface to the measurement solution. In a micromechanical bottom-up process, a multi-layered formation of electrically conducting gold structures and insulating silicon nitride passivation was created by optical lithography, vapor deposition and plasma-enhanced chemical vapor deposition. The successfully produced sensors could be evaluated by redox-cycling measurements on potassium hexacyanoferrate via cyclic voltammetry and amperometry. Functioning sensors could be produced with an inter-electrode distance of 300 and 400 nm and were further evaluated by amperometric measurements in a fluidic setup, investigating the temporal and spatial resolution on concentration-changes of dopamine in solution. The known electrode fouling process of gold electrodes by dopamine could be shown for a concentration of 1 mmol/l dopamine and repetitive potential switches between oxidative and reductive potential could not initiate a reversal. For an in-vitro evaluation of the sensors, dopaminergic PC12 cells were cultivated on the sensor surface and the release of physiological dopamine was successfully induced by potassium chloride and dopamine in solution. The designed sensor could be evaluated to a sensitivity for dopamine of 10 µmol/l, a fast response time and a cycling efficiency larger than 84 %. To further enhance the sensitivity, a modification towards smaller pores was done by nanosphere lithography. Polystyrene nanospheres of 500 nm diameter were deposited on the sensor by spin-coating and air-water-interface self-assembly and served as a shadow mask for the pore etching. Pore structures in

the range of 202 to 141 nm median pore diameter could be created. For the modification towards a flexible sensor array, the existing design was transferred to a polymer-based insulation and substrate material by exchanging silicon nitride with polyimide, resulting in a functioning flexible electrode array embedded in polyimide.

2 Theory and Background

This thesis work covers various subject areas, ranging from basic physics and micro-technology to biochemistry, biology and medical application. A general overview of required theoretical knowledge and background information, as well as processes applied and materials used is given in this chapter.

2.1 Parkinson`s Disease and Deep Brain Stimulation

In this chapter Parkinson`s Disease and therapeutic approaches, like modulation of brain activity by Deep Brain Stimulation, are introduced.

2.1.1 Parkinson`s Disease – Cause and Therapy

Parkinson`s Disease (PD) is one of the most prevalent afflictions of the central nervous system. In Germany alone, approximately 300 000 people are affected, with 20 000 new incidences every year and the main occurrence in the age range between 50 to 79 years [11]. Named after the English physician James Parkinson, who was the first to describe the symptoms in 1817 [12], the disease has been studied at length but remains incurable to this day.

The origin of the disease can be hereditary, acquired or idiopathic, meaning no cause is known and the onset is spontaneous. The idiopathic version is by far the most frequent, with 80 % of all cases [11]. The cardinal symptoms include resting tremor, bradykinesia (slowed movements), rigidity (increased muscular tone), postural instability and gait impairment [13], which can be ascribed to disruptions of the motor cortex. These movement disorders are attributed to a progressive loss of dopaminergic neurons in the midbrain, involving the basal ganglia, thalamus and cortex. Figure 1 shows the motor circuit for the modulation of leg movement with areas involved on a cross section of the brain as a schematic display.

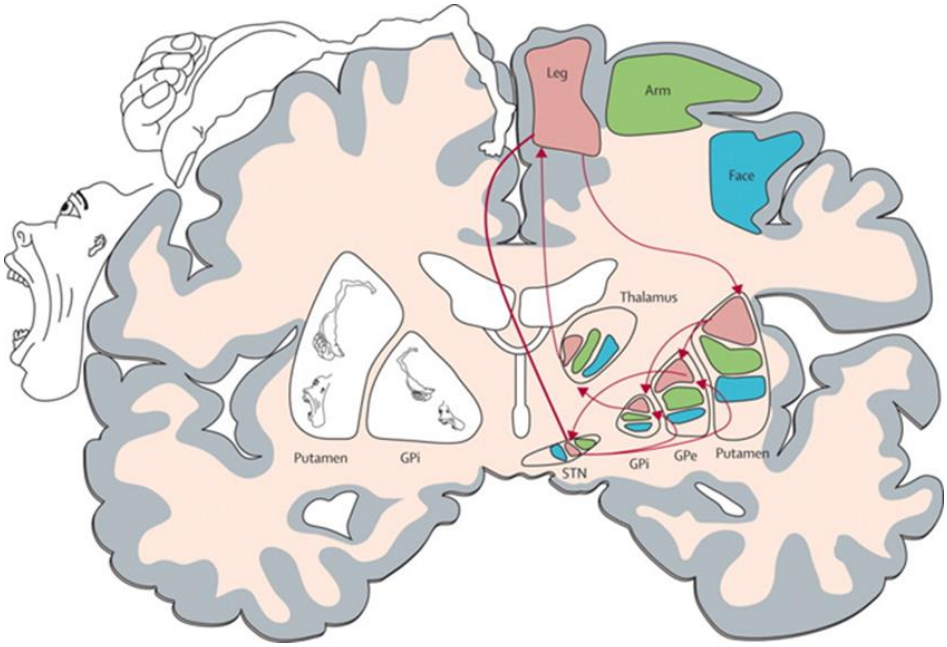

Figure 1: The motor cortex and circuit for modulation of leg movements. [14]

The suppression of movements by inhibition of transition combined with a disrupted suppression of transition result in the parkinsonian motor symptoms [15] .

In addition to the degeneration of dopaminergic cells, an abnormal accumulation of proteins in neurons (Lewy pathology) is found to be responsible for the non-motor symptoms like depression, sleep disorder, olfactory dysfunction, constipation and rapid eye movement [16].

Pharmacological dopamine replacement therapy by orally administering levodopa (L-Dopa), the precursor to dopamine and norepinephrine, or dopamine agonist substances, is the major approach to treating early stage PD. These substances are very effective in treatment of motor symptoms but about 60 % of patients develop serious complications due to response fluctuations and a wearing-off effect after 5 years of levodopa therapy [13]. Most non-motor symptoms show no response to a dopamine replacement therapy [17] and are known to contribute largely to the quality of life in PD patients [3]. Therefore, the direct modulation of basal ganglia activity by an implanted stimulation electrode has become the therapy of choice in advanced PD.

2.1.2 Modulation of Brain Activity by Deep Brain Stimulation

Deep Brain Stimulation (DBS) is a procedure, where a neurostimulator is permanently implanted in the brain parenchyma (functional tissue area) and a chronic, high-frequency

electrical current is applied to the tissue. The neurostimulator electrode rod, called lead, is connected via extension wires, which are tunneled subcutaneously to an implanted pulse generator, located below the collar bone. Figure 2 shows a schematic of the DBS system in place.

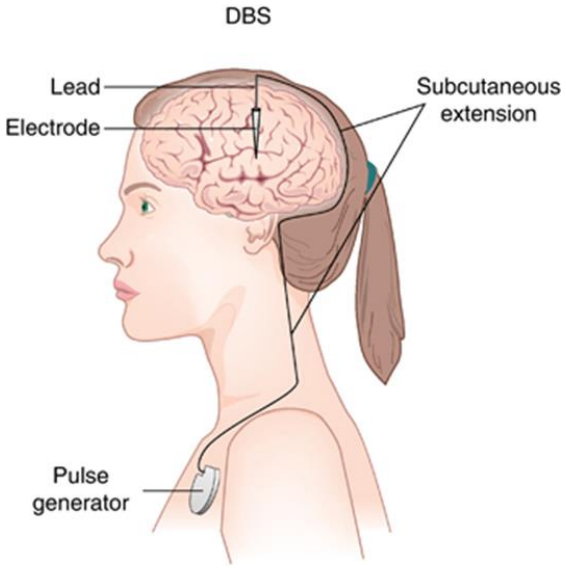

Figure 2: DBS system composed of electrode lead, extension wires and pulse generator. [18]

The pulse generator is powered by a battery and sends electric signals of a preset frequency, amplitude and pulse width to the stimulator electrodes. The current lead model (3389) and neurostimulator (Activa PC) by *Medtronic Inc.* are shown in Figure 3.

Figure 3: a) Lead model 3389 and b) neurostimulator Activa PC by Medtronic PLC.

The electrode is made of a flexible urethane cylinder with 1.27 mm diameter and 4 platinum/iridium circumferential cylindrical contacts at the end. The neurostimulator *Activa PC* offers a current-controlled stimulation mode, which is preferable to a voltage-controlled stimulation, in which the stimulation effects could be involuntary variable. [19]

The lead positioning is crucial for the therapeutic success and the electrode is positioned via image guidance by magnetic resonance imaging (MRI), to locate distinctive landmarks in the brain as well as blood vessels and ventricles, which need to be avoided. The established target areas for DBS in PD are the subthalamic nucleus (STN) and globus pallidus internus (GPi) [20],[21],[22] . In combination with a brain atlas and MRI imaging, the electrode trajectory is planned and verified by a microelectrode, which proceeds the stimulation electrode and is used for local recording of tissue activity to help locate the exact position [23], [24]. The surgical procedure also requires the direct feedback of the awake patient once the stimulation electrode is positioned and tested, to confirm the successful targeting and placement as well as the absence of side effects. After fluoroscopy confirmed the placement of the lead, surgery is completed and postoperative MRI and computed tomography are used to further verify the correct positioning. Misplaced stimulation electrodes and tissue damage by the microelectrode can be cause for serious side effects [25], [26] . Section based on [10]

In general, DBS uses a continuous frequency pulse train in the range of 100-250 Hz. Parameters like amplitude, pulse width and frequency need to be programmed postoperatively in a timely trial-and-error process involving the patient and physician. In the last few years, computer models have also been used to determine the optimal parameters with regard to location and current spread. Section based on [27].

Uni- and bilateral stimulation, with 1 lead in each brain hemisphere, is possible. The electric field can be shaped, the flow of current directed and the area of stimulation limited by using the neurostimulator as anode and the lead as cathode or by performing bipolar stimulation, which can be achieved when another electrode contact serves as anode [28], [29]. The latter is possible with segmented electrode arrays instead of circumferential cylindrical contacts. Figure 4 shows a schematic of segmented DBS electrodes.

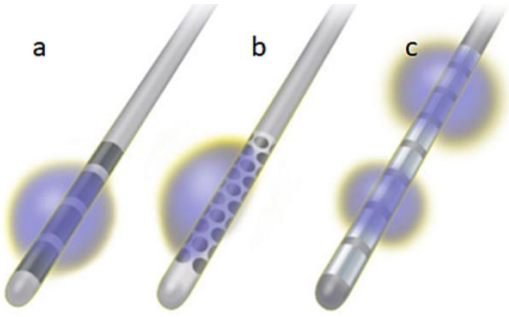

Figure 4: DBS electrode configurations. a) Quadripolar circumferential, b) Multipolar 32 contacts, c) Eight contact electrode with multiple independent current control. [29]

The neurological mechanisms and effects of DBS are still being debated, while it is successfully applied for PD, Essential Tremor, Dystonia, Depression, Tourette syndrome and Epilepsy. Further treatment of headache, addiction, dementia and stroke recovery are being investigated [30]–[33]. DBS increases the output of the stimulated area and activates adjacent fiber pathways. This results in a complex pattern of excitatory and inhibitory modulation of the basal ganglia thalamocortical circuit and regulates neuronal activity by preventing pathologic activity. This in turn alleviates the processing of information and reduces PD symptoms. Section based on [19].

2.2 Neurotransmitter Dopamine and dopaminergic Cell Culture

This chapter introduces the neurotransmitter dopamine, briefly describes the cellular release and the basic requirements and techniques for in-vitro cultivation of dopaminergic cells in culture.

2.2.1 Dopamine and cellular release

Dopamine (3,4-Dihydroxyphenylethylamin) is a compound of a benzene with two hydroxyl side groups and a side-chain amine (Figure 5). It belongs to the group of catecholamines.

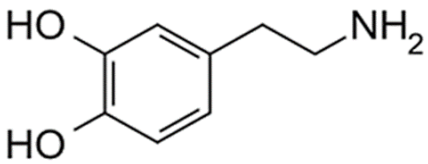

Figure 5: Chemical structure of Dopamine.

Catecholamines are found in the peripheral sympathic nervous system, in the adrenal medulla and various areas of the central nervous system. The precursor to dopamine, 3,4-dihydroxy-phenylalanine (L-Dopa), is physiologically synthesized from the amino acid tyrosine and activated to dopamine via decarboxylation. L-Dopa is also the common drug used for the treatment of motor symptoms in early Parkinson`s disease, since it is incorporated by dopaminergic cells and augments the striatal dopamine by an increased amount of dopamine released [34]. Dopamine is, in turn, the precursor for the neurotransmitters noradrenaline and adrenaline [35]. It is synthesized by neuronal dopaminergic cells and stored in vesicles for release into the synaptic cleft via membrane fusion of vesicle and presynaptic membrane.

This release can be initiated via action potential membrane depolarization and calcium-selective channels as well as via dopamine receptors in the membrane. After release and diffusion to the postsynaptic membrane, dopamine molecules bind to specific dopamine receptors. Depending on the receptor type, binding has an activating or an inhibiting effect. 5 receptor types are known. Receptor type 1 and 5 are proven to have an exciting effect, whereas receptor types 2-4 are inhibiting. Within the basal ganglia, the dopamine receptors are mainly of type 1. Where type 1 and 5 are expressed, extracellular dopamine binding induces a signal cascade, resulting in membrane depolarization and further vesicle release [36]. Once the signal is transmitted, the dopamine molecules are reabsorbed into the presynaptic cell via dopamine transporter channels and stored in vesicles again or catabolized via deamination. Section based [37],[38],[39].

As the hydroxyl groups in the dopamine molecule are released easily, dopamine can be oxidized and reduced in a two-electron transfer. This intrinsic redox nature makes it well suited for electrochemical detection [37]. Electrooxidation of dopamine in physiological pH induces a complicated chemical reaction, that transforms the oxidized dopamine (DA) to dopamine-o-quinone (DAQ). This compound is highly reactive and gets transferred and oxidized further to dopaminechrome (DAC). This product can further undergo polymerization reactions on unprotected electrode surfaces, adhere to those and cause the so called electrode fouling, a loss of sensitivity and electrode activity [40], [41], [42]. The electrode fouling strongly correlates with pH and dopamine concentration in the measurement [41].

2.2.2 Cultivation of dopaminergic cells

For the in-vitro research on dopaminergic cells, the PC12 culture line was isolated from a chemically induced, transplantable pheochromocytoma of a rat in 1976. This cancer is located in the adrenal medulla and secretes catecholamines like dopamine. As in human dopaminergic cells in the substantia nigra, PC12 cells in culture produce dopamine, release it upon depolarization of the cell membrane and incorporate it again. The PC12 cell line is well researched, easy to cultivate and robust. Section based on [43], [44].

Since dopamine is released following the depolarization of the cell membrane, it is possible to stimulate the release with potassium. The addition of positively charged potassium ions decreases the negative charge on the extracellular membrane and depolarize the membrane. As a result, calcium channels open and dopamine release is induced.

The cultivation of any cell line has to be performed under the standard conditions of a cell culture laboratory with environmental settings suited to the specific cell line. Sterility is a prerequisite in cell cultivation. Therefore, ultraviolet germicidal irradiation is a standard process to sterilize materials and surfaces for cell culture. Short wavelength ultraviolet irradiation is based on the destruction of DNA and RNA by UV light, resulting in the inactivation of microorganisms and inhibition of replication. UV irradiation proved to be highly effective against contaminations like viruses, bacteriophages, bacteria, spores and protozoan cysts [45].

As PC12 cells are adhesive, adhesion has to be promoted outside the standard cultivation flask. This is accomplished by the glycoprotein fibronectin, which is promoted by serum-containing media, binds to the surface itself and mediates the mechanical anchoring between the cell membrane and the substrate surface [46]. Additionally, the cell is able to bind to positively charged surfaces, such as plastic, via absorption of bivalent cations onto the surface [47]. This process can be initiated on negatively charged surfaces through attachment factors, such as poly-lysine.

Poly-lysine is a poly-amino acid, promoting the cell attachment to solid surfaces, such as glass. It can be in a poly-l- or poly-d-lysine configuration, depending on the chirality of the central carbon atom. Several lysine molecules collectively form a poly-lysine molecule, which promotes positively charged amino groups at binding sites. Negatively charged oxygen groups of the cell membrane, as well as the glass substrate can be connected via ionic bonds and poly-lysine functions as a mediator between the negatively charged surface and the negatively charged cell membrane [48].

2.3 Electrochemical Measurements

In this chapter the basic electrochemical background, as well as the measurement techniques amperometry, cyclic voltammetry and redox cycling, are reviewed.

2.3.1 Fundamentals in Electrochemistry

Electrochemistry is the science around the transfer of electrons at the electrode-solution interface, combining the electron movement in solid materials with the ion movement in liquids.

Two electrodes surrounded by electrolyte solution is the basic example of an **electrochemical cell** and provides the interfaces necessary for the investigation of the occurring effects. In a

galvanic cell, spontaneous electrode reaction takes place when the electrodes are connected by a conductor, in electrolytic cells an external potential needs to be applied. With two electrodes two independent half-reactions can be observed. The electrode where the reaction of interest takes place is the working electrode (WE), the second is the reference electrode (RE). Several external and electrode variables can influence the rate of an electrode reaction. Figure 6 gives an overview of such contributing variables in an electrochemical cell.

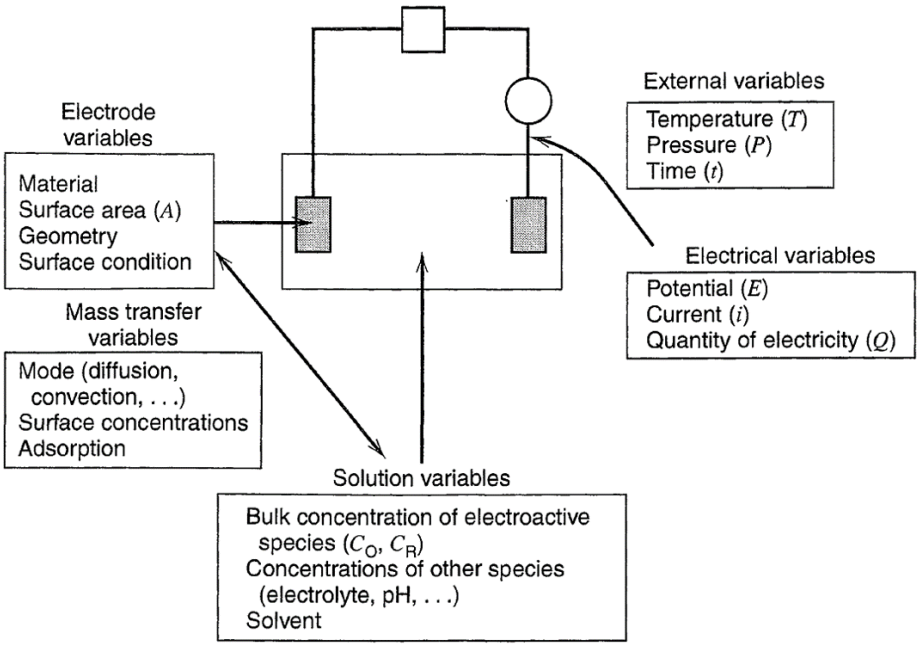

Figure 6: Variables affecting the rate of an electrode reaction. [49]

In a **two-electrode setup**, the current passes through WE and RE and creates a voltage drop equal to the sum of voltage drop at both electrodes and solution resistance *Rs*, following Ohm`s law:

$$V = I * R \tag{1}$$

Therefore, the solution resistance R_s must be small and the voltage drop at the RE must be negligible compared to the resistance of the WE. This is achieved by a much greater surface area of the RE than the WE, resulting in a much smaller current density and voltage drop. Also, the current flow must be kept small in order to reduce the resistance at the RE. Generally, parameters for a two-electrode setup are I < 10 µA and R_s < 100 Ω, so that $I * R_s < (10{-}5A) *$ 100Ω or $I * R_s$ < 1 mV.

For systems where V cannot be kept below 1 mV, a **three-electrode cell** must be used. The third electrode is called counter electrode (CE) and functions as a current sink for the cell. The

majority of the current passes through the CE and WE, thus lowering the potential drop between the RE and WE. This setup allows the RE to be used as a reliable reference for the potential control. Sections based on [49].

Electrochemical electrodes can be classified according to the potential dependency on the electrolyte concentration. Electrodes of the first kind are simple metal electrodes immersed in a solution containing their own ion (e.g., silver immersed in a silver nitrate solution). The equilibrium potential of this electrode is a function of the concentration of the cation of the electrode metal in the solution.

Electrodes of the second kind are a metal electrode assembly with the equilibrium potential being a function of the concentration of an anion in the solution. Typical examples are the silver/silver-chloride electrode and the calomel electrode. The potential of the metal is controlled by the concentration of its cation in the solution, which is, in turn controlled by the anion concentration in the solution through the solubility product of the slightly soluble metal salt:

$$AgCl + e^- \leftrightarrow Ag + Cl^- \tag{2}$$

For a redox reaction

$$O + ne^- \leftrightarrow R \tag{3}$$

where n is the number of electrons exchanged, the relation between concentrations of O and R can be related to the Gibbs free energy change ΔG as follows:

$$\Delta G = \Delta G^0 + RT\ ln\frac{R}{O} \tag{4}$$

where R is the gas constant and T [K] the temperature. Here, the maximum potential between two electrodes or equilibrium potential can be derived

$$\Delta G = -nFE \tag{5}$$

and for unit activity for O and R the standard Gibbs free energy change for the redox reaction can be given as

$$\Delta G^0 = -nFE^0 \tag{6}$$

where E^0 [V] is the standard electrode potential and F the Faraday's constant. With equation (4) and (6) the correlation between potential and concentration for a cell reaction at a redox electrode can be given as the **Nernst equation:**

$$E = E^0 + \frac{RT}{nF} ln \frac{O}{R} \tag{7}$$

The Nernst equation allows the calculation of the electrostatic potential at the electrode for a state of equilibrium without a current flow through the electrode-solution interface. If a reaction needs to be induced, a so called overpotential ŋ, the deviation of the cell potential from its equilibrium value E_{eq}, must be applied:

$$ŋ = E - E_{eq} \tag{8}$$

If a potential is applied to an electrode and results in a current flow, the relation between current and potential can be described by the **Butler-Volmer equation**:

$$I = I_O\left[e^{-\alpha f ŋ} - e^{(1-\alpha) f ŋ}\right] \tag{9}$$

where f is the coefficient $\frac{F}{RT}$, and which employs the exchange current

$$I_0 = FAk^0 C_O^{*(1-\alpha)} C_R^{*\alpha} \tag{10}$$

that is the derived of the current-potential characteristic, A [cm^2] the area of the electrode, k^0 the standard heterogeneous rate constant, C concentration of oxidized or reduced species at the electrode surface and the dimensionless transfer coefficient α.

If a negative potential is applied to the WE, the energy level of the electrons in the electrode material is raised and a phase shift from electrode to electrolyte molecule occurs. The electrons migrate from electrode to electrolyte, **cathodic current** flows and the electrolyte molecules are reduced (**reduction current**). Positive potential applied to the WE lowers the energy level of the electrons in the electrode material. Since the lowest possible potential is desired, electrons migrate from electrolyte into the electrode material, **anodic current** flows and electrolyte molecules are oxidized. Figure 7 shows the contribution of anodic and cathodic current to the overall current I_0.

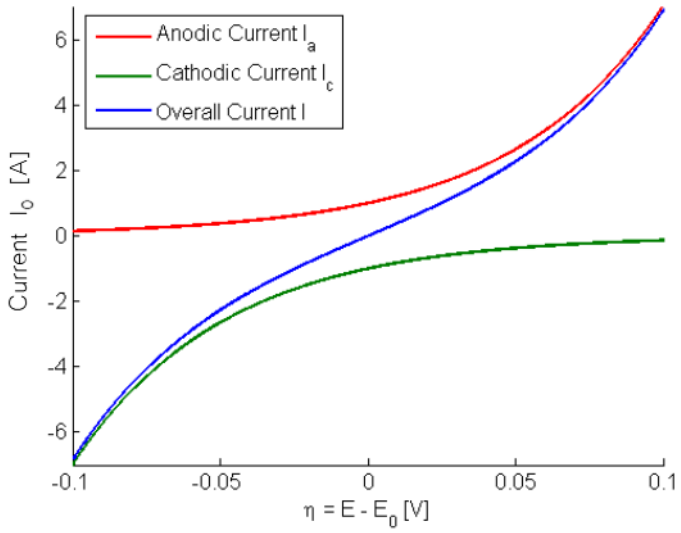

Figure 7: Plot of anodic and cathodic contribution and overall current according to the Butler-Volmer equation (9) at 25 °C. [50] *modified.*

Four major factors affect the **reaction rate** at the electrode-solution interface and the resulting current and are shown in Figure 8 in the pathway of a general electrode reaction:

1. Mass transfer (e.g. of O from bulk to electrode surface)
2. Kinetics of electron transfer
3. Preceding and following chemical reactions
4. Surface reactions (e.g. adsorption, desorption)

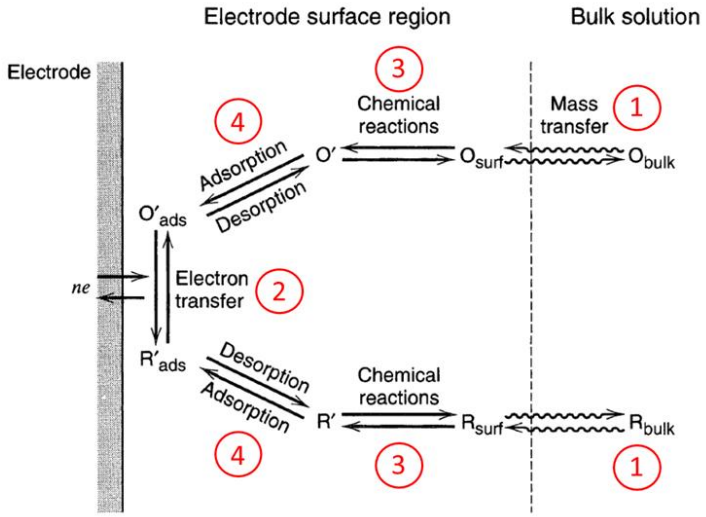

Figure 8: Pathway of a general electrode reaction. [49]

The slowest process will determine the reaction and is called rate-determining step. If all processes are fast, the electron transfer reaction will be the rate-determining step. In order to ensure a diffusion-controlled mass transport for electrochemical experiments, either a large concentration of reactive species in the electrolyte is given to eliminate migration, measurements are completed in under 30 s to avoid convection, or microelectrodes are being used [51].

Two types of charge-related processes occur at electrodes. One kind comprises reactions in which charges are transferred across the electrode-solution interface. Electron transfer causes oxidation or reduction to occur. Since such reactions are governed by Faraday's law (i.e. the amount of chemical reaction caused by the flow of current is proportional to the amount of electricity passed), they are called **faradaic processes**. Processes such as adsorption and desorption can occur, and the structure of the electrode-solution interface can change with changing potential or solution composition. These processes are called **nonfaradaic processes**. Although charge does not cross the interface, external currents can flow when the potential, electrode area, or solution composition changes. The effects of the nonfaradaic processes must be taken into account in using electrochemical data to obtain information about the charge transfer and associated reactions.

In order to understand the reaction kinetics involving an electrochemical process with heterogeneous electron transfer a simplified equivalence circuit model of an electrochemical cell can be used. Figure 9 shows an equivalent circuit:

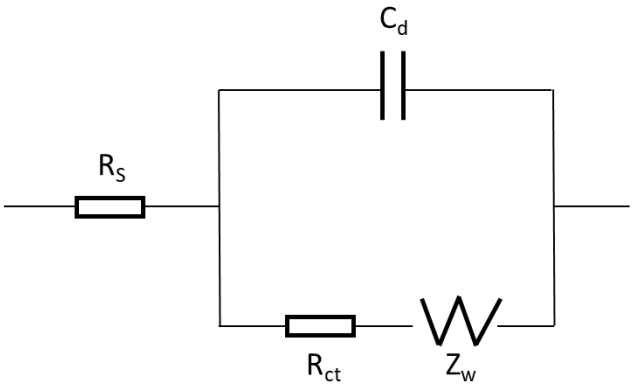

Figure 9: Equivalent circuit model of a simple electrochemical process. [51]

According to Figure 9, electrons can be transferred across the electrode/solution interface via two parallel pathways, the faradaic process, which is represented by the charge transfer resistance R_{ct} and diffusion (Warburg) impedance Z_w connected in series, and the charging/discharging of the electrical double layer C_d. In both cases, the current flows through solution, which is represented by the ohmic resistance R_s. The second pathway is important only if the electrode potential (or surface area) is changed rapidly. In this case, the kinetic parameters can be determined only after separating faradaic current from the double layer charging current. Under steady-state conditions, the charging current is negligibly small and the range of accessible kinetic parameters is determined by the values of R_{ct}, Z_w, and R_s. Clearly, the charge transfer resistance can be measured accurately only if it is much larger than the solution resistance.

The magnitude of solution resistance is less important when relatively slow kinetics are measured. In contrast, fast electrode kinetics can be studied if the ohmic potential drop is either very small (at ultramicroelectrodes under steady-state conditions) or fully compensated. Section based on [51].

The electrode-solution interface can be seen as an **electrical double layer** (Figure 10), with the electrical charge at the electrode surface and charged ions disbursed in the adjacent solution. If a potential is applied to the electrode, the double layer is formed and a charging current flows. Three models of the electrode-electrolyte interface are commonly found, the Helmholtz, the Gouy-Chapman and the Gouy-Chapman-Stern model.

In the **Helmholtz model**, two sub-layers exist in the solution. The first consists of solvent molecules and specifically adsorbed ions. Its boundary is called the **inner Helmholtz plane** (IHP) and marks the location of the electrical centers (χ_1). The second layer consists of solvated ions, which are completely surrounded by solvent molecules and therefore can only approach up to χ_2. Their charges mark the **outer Helmholtz plane** (OHP). Non-specifically adsorbed ions are disbursed in the **diffuse layer**, a three-dimensional region that expands into the bulk of the solution, where the interaction with the electrode only involves long-range electrostatics. This model features solvated ions as circular with a centrically located punctual charge.

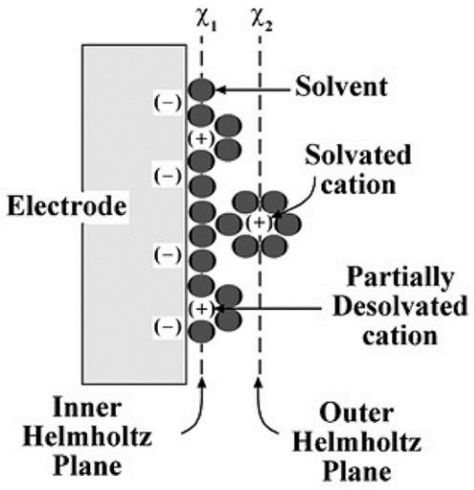

Figure 10: Electric double layer or Helmholtz plane. [51]

The Helmholtz model has been enhanced by Gouy and Chapman to describe the solvated ions to be a point-like canonical ensemble and is named the **Gouy-Chapman model** [52]. It accounts for thermal motion of solvated ions and describes a more extended, diffuse charged layer, but is only accurate for concentrations below 1 mmol/l and small potentials. Otto Stern combined the Helmholtz and Gouy-Chapman theories in a model, which regards a finite ion size and the approach to the interface and is known as the **Gouy-Chapman-Stern model**. Here, a compact Helmholtz plane exists directly on the electrode surface and a diffuse layer distanced further in the bulk solution follows [53].

2.3.2 Classical Electrochemical Measurements

In electroanalytical experiments the potential at the WE is being controlled by a potentiostat. This electronic hardware is a control amplifier that maintains the potential of the working electrode at a constant level with respect to the reference electrode by adjusting the current at the counter electrode.

In electrochemical measurements the response to a change of parameter such as applied voltage or current or a change over time are observed. Depending on the parameter to be measured and the alteration conducted, various standard electrochemical experiments can be distinguished.

C**hronoamperometry** is a technique in which the potential of the working electrode is stepped from an initial potential E_1, where faradaic processes do not occur, to a potential E_2 where oxidation or reduction takes place. The resulting current from faradic processes occurring at

the electrode is monitored as a function of time. For the simple charge transfer reaction (eq. 3 in chapter 2.3.1) the potential E_1 is chosen, so that the concentration of O at the electrode is zero and the current induced by the potential step is only due to diffusion of O towards the electrode and the reduction process initiated. The reduction at the electrode surface induces a very large current, because it occurs instantly and this creates a concentration gradient, which in turn produces a flux of reactant O to the electrode surface proportional to the concentration gradient. A continued flux creates a so called depletion zone where O is absent and the current as well as the concentration profile declines.

Figure 11 shows the waveform for a potential step and the current flow vs. time:

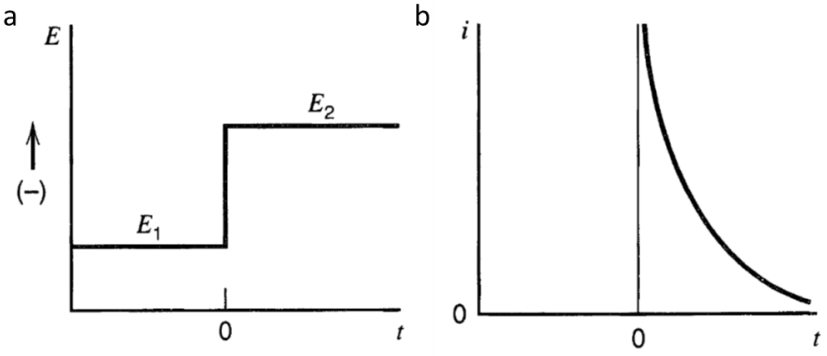

Figure 11: a) Potential step from E_1 to E_2, b) Current flow vs. time. [49]

The current-time response for spherical electrodes is reflected in the Cottrell equation:

$$I(t) \triangleq i = \frac{FAD_O^{1/2}C_O^*}{\pi^{1/2}t^{1/2}} \tag{11}$$

where D_O is the diffusion coefficient of the oxidized species and t the time. The building of a depletion zone due to the reduction process is reflected in the inverse function $t^{1/2}$.

Cyclic Voltammetry (CV) is a potential sweep method, in which the electrode potential is changed linearly over time and the resulting current in relation is recorded. The potential sweep becomes cyclic, when an initial potential E_1 is being increased to a reversal potential E_2 and swept back to E_1 and further to a potential E_3 at the reverse direction. Figure 12 shows the waveform for a linear and cyclic sweep with starting and reversal potential, v is the scan rate.

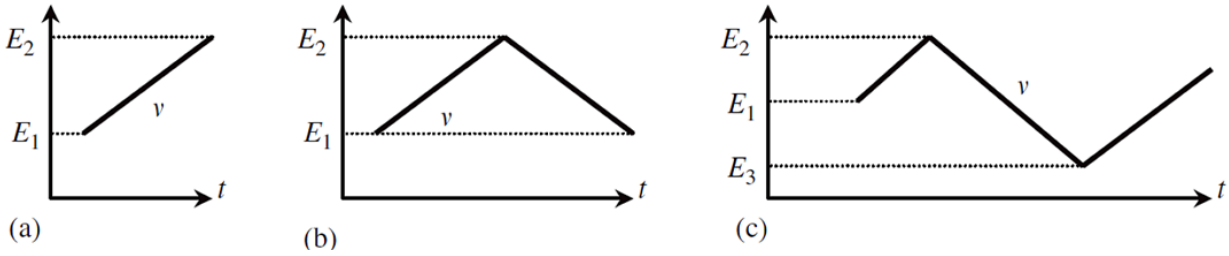

Figure 12: Waveforms used in linear sweep (a) and cyclic voltammetry (b and c). [51]

The choice of potentials is an important step in the experimental design, since they determine the driving force for the electron transfer, the reaction to take place (oxidation or reduction), the species formed and weather the reaction takes place under kinetic or mass transport control. The scan rate determines the reaction time scale and is typically ranged between mV/sec and up to kV/sec with microelectrodes. Section based on [51].

The current-voltage curve or cyclic voltammogram displays the reaction mechanism and the gradient characteristic for the substance under reaction. Figure 13 shows a cyclic voltammogram for a diffusion-controlled electron transfer on a planar electrode:

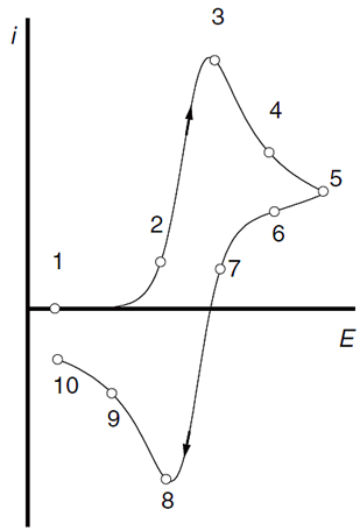

Figure 13. Cyclic voltammogram. [51]

With the changing potential, the concentrations for generated species changes and as such the produced faradaic current in relation to the reaction taking place and concentration at the electrode. For the case of a reduced species initially present, points 1-7 show the oxidation of

the species and the resulting oxidation current, with the peak value I_P at the potential of point 3. After the reversal of the potential at point 5, the reduction of the previously oxidized species takes place between points 8-10 and results in a reduction current.

The peak current I_P can be calculated for a planar electrode and diffusion controlled reaction with the **Randles–Sevčik equation**:

$$I_P = 0{,}4463 \frac{n^{3/2} F^{3/2}}{R^{1/2} T^{1/2}} A D_O^{1/2} C_O^* \nu^{1/2} \tag{12}$$

with n being the number of electrons transferred.

The shape of a voltammogram relates to the rate of electron transfer. If the mass transport is diffusion controlled, the shape is that of Figure 13. If the mass transfer overcomes the electron transfer rate, the voltammogram becomes drawn out (Figure 14), the peaks broaden and the overpotential needed to drive the electron transfer rate increases, which results in a wider peak separation. Section based on [51].

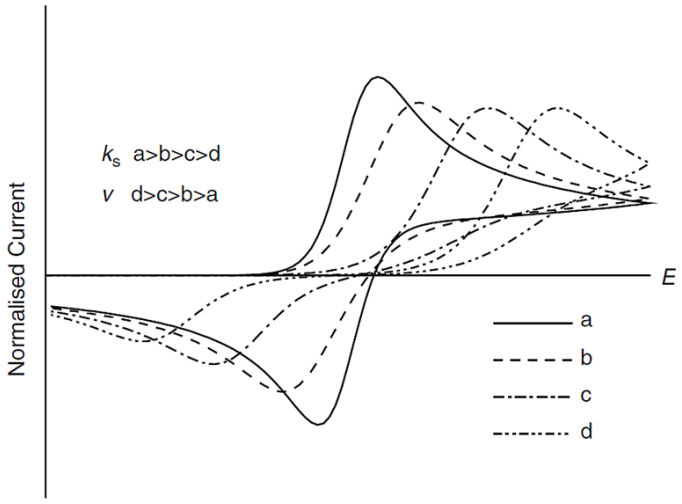

Figure 14: Voltammograms (current scale normalized) under a) electron transfer control, b-d) mass transfer control. k_S: electron transfer rate constant, v: sweep rate. [51]

In the method of fast-scan cyclic voltammetry (FSCV), CV is being done with frequencies in the kHz [54] or even MHz [55] range, which no longer limits the sensitivity to mass transfer processes, when the cycling frequency is faster than the diffusion and repeated cycling of analyte molecules is possible. This technique also has an increased selectivity to analytes, which can undergo repeated redox reactions versus those that only react in one way [56].

Redox cycling is a measurement technique utilizing two working electrodes, each set above a reductive or oxidative potential, thus driving both, a reduction and oxidation process and recording the respective charge transfer. If placed closely enough for molecular diffusion, the analyte species can shuttle between the two working electrodes and undergo a repetitive oxidation-reduction process, thus be cycled between the electrodes (Figure 15). This requires a reversible process and redox-active analyte.

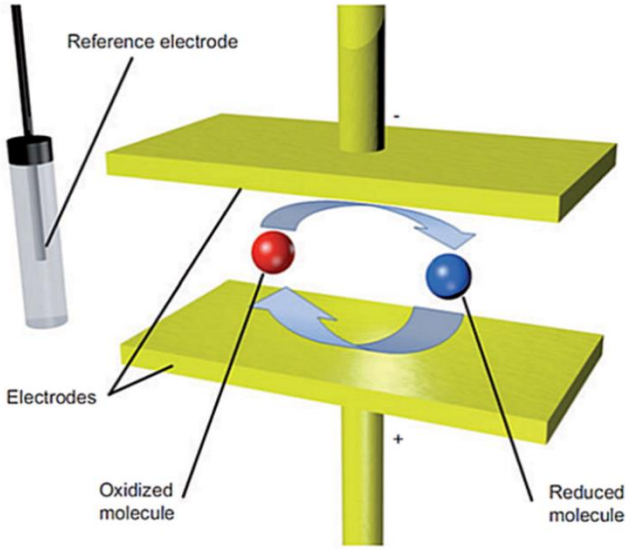

Figure 15: Redox cycling process at two electrodes biased to oxidation/reduction potential. [56]

A redox active substance well suited for experimental measurements is potassium hexacyanoferrate $K_4[Fe(CN)_6]$. This salt of monoclinic crystal structure is non-toxic, since it does not release the cyanide from the complex. In aqueous solutions, the anion hexacyanoferrate(II) oxidizes to hexacyanoferrate(III) in a reversible one-electron-transfer reaction

$$[\,Fe(CN)_6\,]^{4-} \leftrightarrow [\,FE(CN)_6\,]^{3-} + e^- \tag{13}$$

The inter-electrode distance h is an important design consideration, since it influences the shuttling time T_S and the amplification, with the diffusion constant D as analyte specific parameter, for plane-parallel electrode positioning and one-dimensional diffusion as

$$t_S = \frac{h^2}{2D} \tag{14}$$

and even allows the calculation [57] of the average cycling current for a single analyte molecule

$$I_{cyc} = \frac{ne_0}{2T_S} = \frac{ne_0 D}{h^2} \tag{15}$$

with n being the number of electrons transferred and e_0 the elementary charge.

Another important design consideration is the spatial confinement of the analyte molecule, which is dependent on the geometry and needs to consider open access for the electrolyte, as well as diffusion barriers. Generally, the collection efficiency Ɲ is defined as the ratio of the current at the generating and the collecting electrode [58]:

$$Ɲ = \frac{I_{col}}{I_{gen}} \tag{16}$$

Several design choices like interdigitated arrays, pore-based approaches and nanocavity devices have been investigated over the past decade. Section based on [56].

2.4 Multi Electrode Array

This chapter introduces the Multi Electrode Array (MEA), also called Micro Electrode Array, and gives an overview over different designs as well as the flexible version intended for implantation.

2.4.1 MEA Devices

The first multi electrode array was developed in 1972 by C.A. Thomas and intended for use on neuronal cell cultures [59]. Over the years, a broad variety of arrays in different categories were developed, materials tested and measurement setups designed, which cannot be included in this brief introduction. A good overview is given in [60].

Multi electrode arrays are devices, that hold several electrical contacts, plates or shanks, through which electrical signals can be recorded or stimulation can be initiated. These contacts are housed in an insulating layer. The individual electrodes can be arranged randomly, like in sealed metal wires or carbon fibers embedded in glass or epoxy resin. Regularly spaced electrodes in ordered designs include paired electrode designs like a double band assembly and interdigitated arrays (IDA). These planar designs were initially intended for in-vitro experiments with neuronal cell cultures or tissue cultures.

Compared to planar electrode arrays, 3D arrays have either shaped electrodes, that allow penetration of tissue, or individual electrodes located not only next to each other but also atop of each other. Figure 16 shows the variety of electrode arrangements mentioned above.

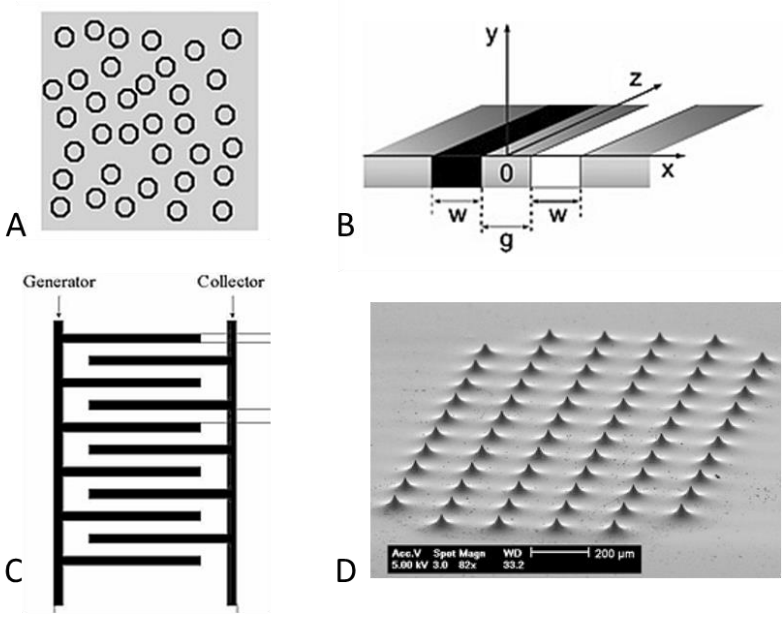

Figure 16: Electrode arrangements: A) Schematic random array [51]*, B) paired electrode, schematic double band assembly* [51]*, C) schematic interdigitated array* [61]*, D) 3-D MEA with tip-shaped glass electrodes* [60]*.*

Using the third dimension in the MEA design allows the construction of a generator-collector array, with individually addressable, plane-parallel electrodes in pairs, located next to each other. In this design, an individual redox cycling (see chapter 2.3.2) electrode pair can be generated next to neighboring electrode pairs.

Depending on the intended use, non-implantable (in vitro) and implantable (in vivo) designs can be distinguished. Non-implantable designs tend to be rigid and planar, with thin MEAs to allow imaging with microscopes. These designs are commercially available and consist of a planar MEA with a fluidic compartment to hold the cell culture or tissue slice in medium. Figure 17 shows a standard model MEA by *Multichannel Systems GmbH*.

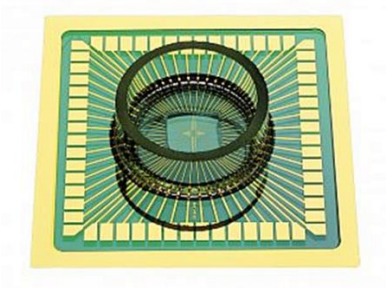

Figure 17: Planar MEA for in vitro use. [62]

2.4.2 Flexible MEAs

The advances in technology and material for MEA production allow the transfer of the initial in-vitro design towards implantable microelectrode arrays for in-vivo measurements. Here, the biocompatibility, biostability and implantability are inevitable demands on the device, next to functionality and durability. In order to minimize mechanical traumatization of the tissue, flexibility is key in any implantable microelectrode device, since close contact to the target tissue, like nerve tissue or sensory cells, is functionally necessary. Therefore, polymers like polydimethylsiloxane (PDMS, silicone), polyparaxylene (PPX, Parylene) and polyimides have successfully been applied for encapsulation and insulation of neuromodulation devices like spinal cord stimulators or sensory implants like the cochlear implants or retina implants [63]. A polyimide-based, flexible version of a multi electrode array is being used in the surface electrocorticograms for cortical stimulation mapping [64]. Figure 18 shows the commercially available device flexMEA36 from *Multichannel Systems GmbH*.

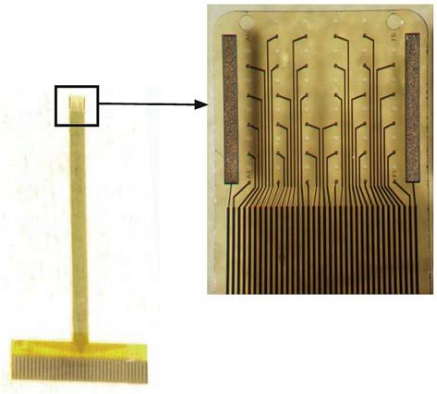

Figure 18: FlexMEA36, 36 TiN electrodes of 30µm diameter in polyimide 2611. [65]

2.5 Micromechanical Bottom-Up Process

This chapter introduces the materials and techniques used in the construction of MEA devices, such as the redox cycling sensor developed in this thesis. The method utilized is called a bottom-up process, since layer after layer of material is constructed on top of the other. The structuring of material is done by lithography, the deposition by vapor deposition techniques and the removal of material via dry and wet chemical etch methods.

Micromechanical manufacturing in a cleanroom environment is the standard for bottom-up processes. The main advantage in a bottom-up process is the construction of small structures in the nanometer range, that can be achieved due to the 3D material deposition. As such, it is much simpler to locate two electrodes nanometers apart when they are insulated by a thin layer in a vertical position, than to create them coplanar horizontally. Further, batch processes can easily be realized by the bottom-up method and therefore have a significant advantage in output number and cost. The choice of material is limited by the processes involved and has to be coordinated with the technologies used and materials to be combined.

2.5.1 Materials

Glass as substrate material in the form of wafers is widely used, when the substrate does not have to have the properties of a semiconductor, in which case silicon substrate with defined crystal orientation is used and electrodes have to be isolated from the substrate. Transparency, good chemical and electrical isolation and low cost are the main advantages of glass substrate. Mostly, borosilicate glass, containing boric oxide, is used. It has a similar thermal expansion coefficient to various metals and silicon [60] and can be cut into shape by a wafer dicing saw with a glass blade.

Titanium is often used as an adhesion layer, as are chromium, molybdenum, tantalum, tungsten or platinum. Adhesion layers are necessary, because the best electrically conductive materials, such as gold, silver or copper, do not stick to SiO_2, and they facilitate the required physical interlocking, chemical bonding or interdiffusion. Titanium forms a titanium-silicon system immediately after deposition and thus a strong bonding. The negative enthalpy of titanium is the source of this reaction and additionally provides a negative heat reaction with SiO_2, which results in the formation of Ti-Si and TiO_2. In the absence of oxygen, like in a vacuum

environment, the transition of titanium to gold is interconnected due to interdiffusion, which creates intermetallic phases such as $TiAu_2$, TiAu or Ti_3Au [66]. Section based on [67]. Since titanium has a high formation of oxidation, the following layer needs to be deposited immediately afterwards.

Gold is chemically inert, an excellent electrical conductor, has a low resistivity and is easily microfabricated, which makes it a commonly used metal for electrode materials [51][60]. In addition, it is biostable and biocompatible [68]. With a Young`s module of 35-44 GPa [69] it is relatively soft. Gold crystalizes in a face-centered cubic crystal structure and grows in the Volmer-Weber island growth mode, which creates single hemispherical islands, that percolate at a film thickness of 8 nm and form a complete film at a thickness of 12 nm [70]–[72]. It has a melting point of 1064,18 °C, but can start spreading of clusters below 727 °C [48][49]. Due to the poor adhesion properties to other materials, adhesion layers have to be created.

Silicon Nitride (Si_3N_4), as well as silicon oxide (SiO_2), are commonly used as insulating materials in microtechnological devices. Si_3N_4 has a dielectric constant of 7 and an electrical resistivity of 10^{14} Ωcm [75], which makes it an excellent insulator. Additionally, it is a very effective diffusion barrier for sodium and water. It is created by chemical vapor deposition (Chapter 2.5.3) as an amorphous material (SiN_x), or in two hexagonal crystalline forms depending on the temperature. It shows a high chemical resistance, resistance to oxidation and high strength. In this thesis, the silicon nitride was deposited at low temperatures with the precursors silane (SiH_4) and ammonia (NH_3) in the general reaction

$$3\ SiH_4 + 4\ NH_3 \rightarrow Si_3N_4 + 12\ H_2 \qquad (17)$$

for the temperature range of deposition from 700 – 1150 °C and a pressure of 1 atm. Section based on [75]. At temperatures below 580 °C, as applied in this thesis, the amorphous SiN_x is created [76].

In the dry etching method of reactive ion etching (Chapter 2.5.4) fluorine gas compounds in an oxygen atmosphere remove the SiN_x with the process gases tetrafluormethane (CF_4) or methyl trifluoride (CHF_3) in the simplified reaction

$$Si_3N_4 + 12\ F \rightarrow 3\ SiF_4 + 2N_2 \quad (18)$$

The use of CF_4 as a fluorine source instead of CHF_3 has shown to create a clean surface, where CHF_3 leaves a coating of fluorocarbon polymer [77].

Chromium is being used as an adhesion layer as well as a sacrificial layer in micromechanical technology. It can be deposited by vapor deposition, removed selectively by wet chemical etching and is a cheap method to create a fully covering protective layer. By use of the composition ceric ammonium nitrate $(NH_4)_2CE(NO_3)_6$: perchloric acid ($HClO_4$) : water (H_2O) in 10.9 % : 4.25 % : 84.85 % (Chrome etch n°1 by Microchemicals GmbH) chromium can be removed selectively towards titanium, gold and silicon nitride and residue-free [78][79].

Polymers such as **Polyimide** have shown to be well suited materials for requirements like compatibility to living tissue, long-term stability, low stiffness and electrical insulation. Polyimide can be used as substrate and insulation layer, thus allowing the construction of flexible MEAs (Chapter 2.4.2, Figure 18). Features like thermoxidative stability, high modulus and mechanical strength, good insulating properties and chemical resistance make polyimide an optimal material [63]. In addition, it can be applied via spin-coating in the form of a liquid precursor. This allows the variation of the material thickness. During a prebake the solvent can partly be driven out to enhance adhesion. The final curing, where the polymerisation occurs, results in a loss of volume of about 50 %. The polyimide in this thesis is a type biphenyldianhydride/1,4 phenylenediamine (BPDA)-(PPD) precursor, which is well suited for microelectric applications [80] and commercially available as PI2610 / PI2611 from *HD MicroSystems GmbH*. Figure 19 shows the structural formula with its specific sequence of imide, ether groups and benzene rings:

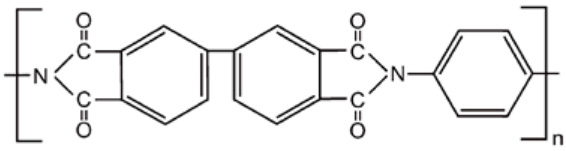

Figure 19: (BPDA)-(PPD) based polyimide. [63]

2.5.2 Patterning by Photolithography

The method of photolithography is a standard in micromechanical manufacturing processes and based on the selective exposure of a reactive material to electromagnetic radiation, which causes a reaction, that in turn allows the selective removal of the material and thus a patterning. The resolution is dependent on the type of radiation and its wavelength, it increases with decreasing wavelength. Most commonly used are the near UV light (350-500 nm) of a Mercury lamp or the deep UV light (150-300 nm) of an excimer laser. Electron-beam, ion-beam or X-ray lithography are particle-based forms of lithographic patterning.

The photolithographic process has three consecutive steps, resist deposition, exposure and development. First, the reactive material, called resist, has to be deposited. This is done via spin-coating. The resist consists of amorphous polymer, which changes structure during radiation and becomes more or less soluble. Positive resist becomes soluble after radiation exposure, as the polymer chains get ruptured by radiation, whereas negative resist is being strengthened by radiation, as it randomly cross-links the polymer. Sensitizer is necessary to control the chemical reactions and casting solvent keeps the resist in a liquid state. [51]

The spin speed (rounds per minute) determines the resist layer thickness. After spin-coating, a pre-bake removes the solvent and leaves the polymer in its reactive state. The second step is the exposure to the radiation. This step includes the transfer of the intended pattern onto the resist by a shadow mask, mostly consisting of a chromium layer in the shape of the pattern on a glass substrate. This lithography mask is placed between the radiation source and resist-covered substrate in a so-called mask aligner unit, either in direct contact (hard contact) or in close proximity (soft contact). The exposure time is an important parameter, since the resist can be overexposed, resulting in larger structures and frayed edges, or underexposed, resulting in a loss of structures due to incomplete reaction of the polymer. After the exposure, the resist consists of soluble and insoluble areas. The development of the resist in the appropriate solvent dissolves the soluble resist, leaving a pattern on the substrate. After metal deposition, the remaining resist is removed by a strong solvent like acetone, which lifts the metal on top as well, resulting in the intended pattern of deposited metal on the substrate. Figure 20 shows an overview of the photolithographic process with gold deposition on glass substrate as a schematic for positive resist.

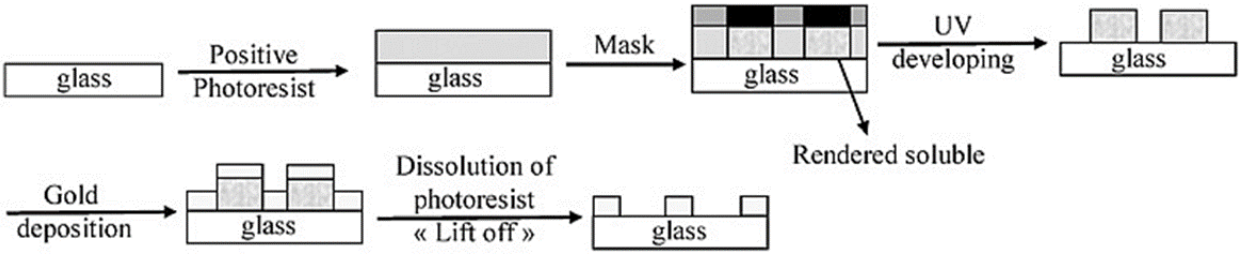

Figure 20: Photolithography process with positive resin to create gold structures. [51]

The optical resolution is dependent on the wavelength (λ) and numerical aperture (NA) of the optical system, according to the Rayleigh diffraction:

$$R = \frac{k_1 \lambda}{NA} \tag{19}$$

with k_1 being an imaging technology constant > 0.7.

Therefore, the construction of smaller structures needs an increased numerical aperture or decreased wavelength. This is achieved by use of particles (electrons, ions) instead of photons or by X-ray lithography. Chapter based on [51].

2.5.3 Vapor Deposition

The vapor deposition method is widely used in micromechanics to deposit materials on structured surfaces. Physical and chemical vapor deposition can be distinguished.

In **Physical Vapor Deposition (PVD)** intense application of energy transforms a target material from the solid state to a gaseous state, which then condenses onto the substrate and creates a thin layer. The evaporation of material can be induced by various technological procedures, like thermal or electron-beam evaporation, sputtering or pulsed laser deposition technique. In **thermal evaporation**, the material contained in a conductive skillet is heated to a gaseous state by either heat or current conduction, induction or a laser beam. In this resistance-heated vaporization only materials with a low evaporation point like alumina, copper, silver or gold can be evaporated. **Electron-beam evaporation** uses a focused electron beam to target the material surface and evaporate material of a higher evaporation temperature.

In the **sputtering** technique, an ion bombardment is used to knock out atoms of the solid target material. Here, an ionized atmosphere or a plasma needs to be created and the ions are directed to the target material in an electric field. High-frequency (HF) sputtering is widely

used, where the electrons following the alternating electrical field collide with the target material, which becomes negatively charged and the ions follow the charge and knock out atoms of the target material to be deposited. In ion-sputtering, mostly noble gases like argon are used to avoid chemical interaction between ions and the target material.

Both techniques require a defined atmosphere, which allows the gaseous particles to travel unhindered towards the substrate surface. This is accomplished by creating a vacuum environment in the evaporation chamber, which reduces collisions of the gaseous particles and thus agglomeration. Section based on [81].

Chemical Vapor Deposition (CVD) uses gaseous chemical compounds, precursor gases, which are thermally, electrically or photonically activated to react and form the desired solid material, which deposits onto a substrate. The reactions take place on the substrate surface, which allows for the process to take place at higher pressures than with PVD. Next to thermal CVD, where the reactions are initiated by high temperature surfaces inside the reaction chamber, **plasma-enhanced CVD (PECVD)** is performed. Here, the gaseous phase in the reaction chamber is ionized by either glow discharge or an alternating electrical field and the ions are directed towards the substrate, where the desired compound is created. This technique has the advantage of a high reactivity of the precursor gases and a resulting high deposition rate in comparatively low temperature ranges. Parameters like chamber pressure, precursor gas and carrier gas concentration, temperature and frequency of alternation of the electrical field can be adjusted to create the desired deposition conditions. Section based on [81].

2.5.4 Dry Etching

In a dry etching process, the material removal reactions occur in the gas phase, not a liquid like in wet chemical etching. Due to the advantages like etch directionality and thus transfer of defined pattern into bulk material, cleanliness and compatibility to vacuum processing technologies, the dry etching is a standard tool in microtechnology. Dry etching can be non-plasma based or plasma based. Plasma-based dry etch utilizing radio-frequency-driven, capacitatively coupled electrodes and suitable gases, which form chemically reactive species, is called **Reactive-Ion-Etch (RIE)**. This process is mostly done in a parallel-plate reactor, where the substrate plate functions as cathode and the chamber wall as anode. Figure 21 shows the schematic of a RIE plasma chamber.

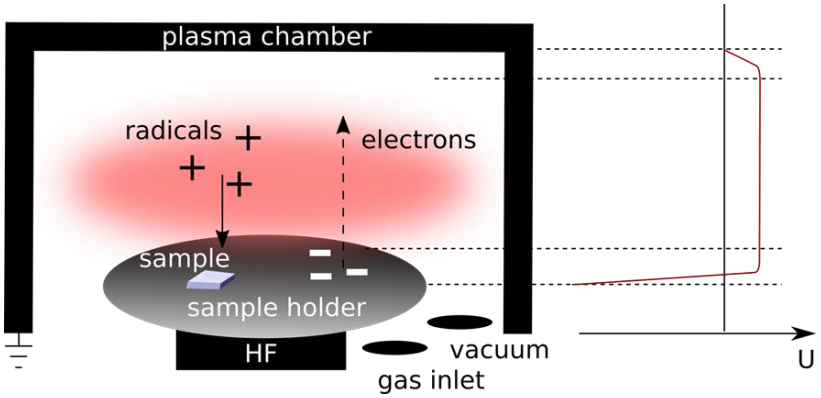

Figure 21: Plasma chamber for RIE, with parallel plate setup. [82] *modified.*

The RIE process is made up of several reactions [83]:

1. Generation of the gas phase with ignition of plasma (glow discharge)
2. DC bias formation with electron transfer to the substrate (cathode)
3. Diffusion / forced convection of reactive ions to the substrate
4. Adsorption of reactive radicals to the substrate surface (ion bombardment)
5. Reaction between radicals and substrate surface material, enhanced by ion bombardment
6. Desorption of the volatile reaction product
7. Exhaust with diffusion of reaction product into the bulk and out of the reaction chamber

Section based on [84].

Poor reaction of radicals with the bulk material, isotropic etching (equally in all directions), or plasma-induced dissociation of product molecules with redeposition on the substrate surface is to be avoided by choosing the optimal parameter setting for pressure, temperature, power and gas flow rate. Physical etching dominates, when the material ablation is induced mostly by ion bombardment. Chemical etching dominates when the reactive radical reaction dominates the material removal. In RIE best results are achieved due to the combination of both processes.

The etching of silicon by RIE creates a special byproduct called black silicon or silicon grass and is an effect of ion bombardment and the creation of so called micromasks. These micromasks arise from re-adsorption of silicon oxide or dust and native oxide already on the substrate.

This creates a sort of mask for the etching process, which results in a number of spikes consisting of silicon and the masking material on the very top. These spikes can be seen in SEM imaging and tend to adsorb light, making the area appear black, hence the name black silicon. The formation of these spikes can be prevented with parameter modification in the RIE process and the addition of CHF_3 gas to the process [85].

In addition to the etching of material, RIE is used for surface activation. Oxygen plasma inherent radicals bind hydrogen or break up native oxygen atoms at negatively charged surfaces, which results in a layer of highly reactive oxygen ions instead of non-polar stable hydrogen or oxygen bound to the substrate surface. This process increases the wettability of the surface [86],[87].

The method of **Ion Beam Etching (IBE)** is utilized when material, which is not easily etched by chemical methods needs to be patterned. In this method, a directed energetic flux of ions is used for material ablation at low pressures (< 1 mTorr). The plasma is created in a remote location, called Kaufman source, by an electron gas and the inert ions are directed from the plasma via electrostatically controlled grids in front of the substrate onto the substrate surface [84]. The main advantage of IBE is the possibility to etch any material like Ti, Au, Pt and even multilayer structures. Since it utilizes the shadow-mask technique to select the exposed areas, where protected areas are covered by a sacrificial layer, and the ablation process is based on the physical bombardment with ions, mask undercut is minimal and small geometries can be etched. IBE has demonstrated the highest etch resolution among comparative technologies for structures < 100 Å [88].

2.6 Nanosphere Lithography

A simple and cost effective approach to small structures is the method of colloidal lithography or nanosphere lithography (NSL). This chapter introduces the basics of the NSL process and the common application techniques with a modified particle distribution method.

Since the first report of an ordered monolayer of colloidal spheres by Fischer and Zingsheim [89] in 1981, there has been great interest in NSL. Compared to high-technology approaches to create miniaturized devices, NSL is inexpensive, compatible with wafer-scale processes and allows the construction of one-, two- and three-dimensional structures.

Spherical particles in the nanometer range are used to create a shadow mask by functioning as a placeholder. The spheres are deposited directly on top of the substrate or metal layers, material is deposited and the particles are removed, leaving a structure to be further treated by wet or dry etching. Figure 22 shows a schematic of the nanosphere lithography process.

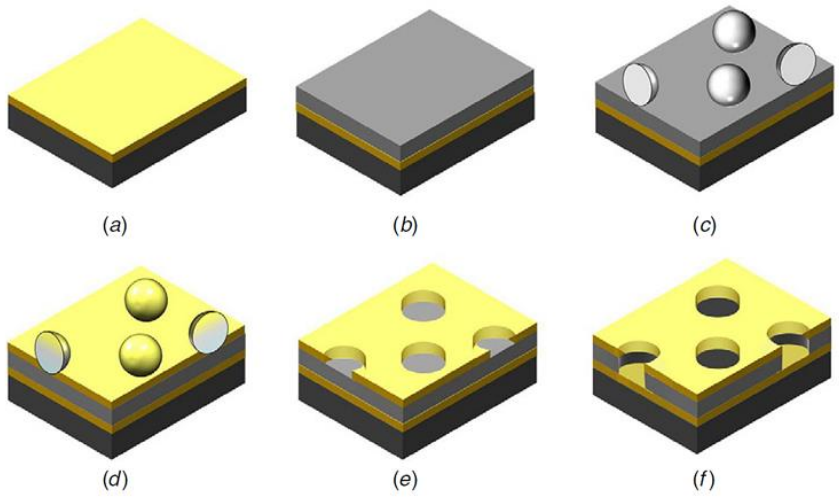

Figure 22: Schematic process of Nanosphere Lithography: a) b) Metal layers on substrate, c) spherical particles deposited, d) Second material deposition, e) Removal of spheres, f) Etching of structure to create pores. [90] *modified.*

The particle deposition is the most critical step, since a 2-dimensional hexagonally close-packed (HCP) monolayer of particles, evenly spaced without defect areas, is pursued. For this, surface modifications like the surface charge of particles and substrate, cleanliness and sufficient control over the deposition method have to be considered. Several deposition methods like spin coating, dip coating, drop coating and self-assembly along an air-liquid interface are common. For all these methods, the particles have to be in solution, which also allows the adjustment of the concentration for best results. The same principle for the particle assembly is behind the afore mentioned deposition methods. At the interface of air and liquid, evaporation takes place which induces a meniscus between the spheres, that creates attractive capillary forces F_c and initiates the assembly. The hydrodynamic force F_d pulls particles together. Both forces are the result of the hydrodynamic flux J_S. Figure 23 shows a schematic of the process.

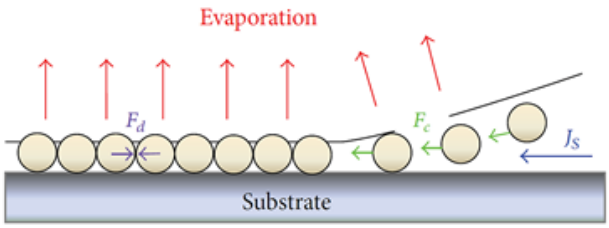

Figure 23:Main forces on particles in solvent-evaporation self-assembly. [91]

Next to temperature and humidity, the attractive capillary force, convective transport of spheres and solvent evaporation rate are the dominating factors for particle self-assembly [92], [93]. With the spin-coating deposition method, particles get dropped onto a substrate, which is immediately rotated at a set speed, thus influencing the spreading of solution and the evaporation rate and therefore the forces induced on the spheres. Similar effects are achieved by drop- and dip-coating, where the spreading of solution and evaporation rate are controlled via inclination of the substrate surface and spreading of solution or the removal of substrate immersed in solution and the active movement of the air-solution interface. Figure 24 shows the principle of these deposition methods. Section based on [91].

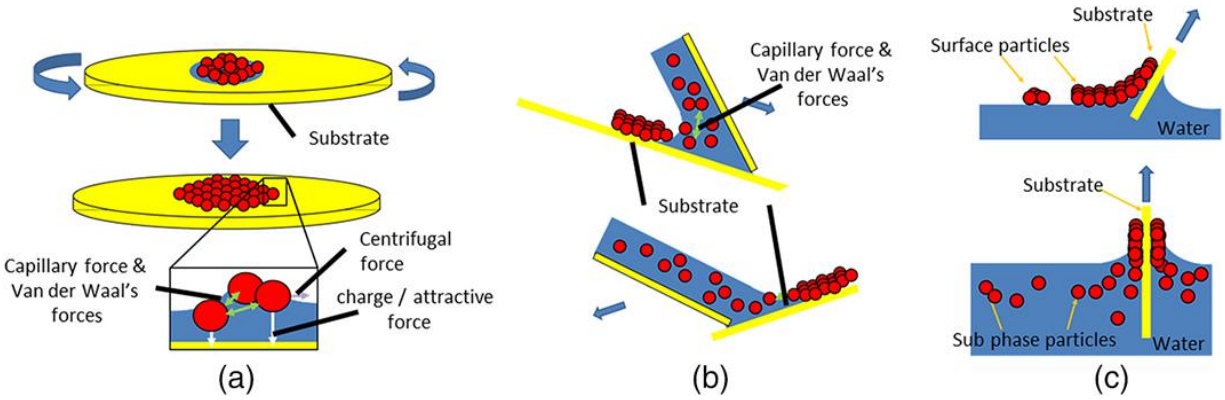

Figure 24: Deposition methods of nanosphere solution and formation of hcp monolayers by a) spin-coating, b) drop coating (convective coating), c) dip-coating. [94]

Another technique of creating two-dimensional, close-packed monolayers of nanospheres was developed by Yu et al. [95] and modified by Geng et al. [96] and involves an air-liquid interface to evenly distribute nanosphere particles. The process takes place in a glass petri dish on a glass slide surrounded by water and is shown and described in Figure 25.

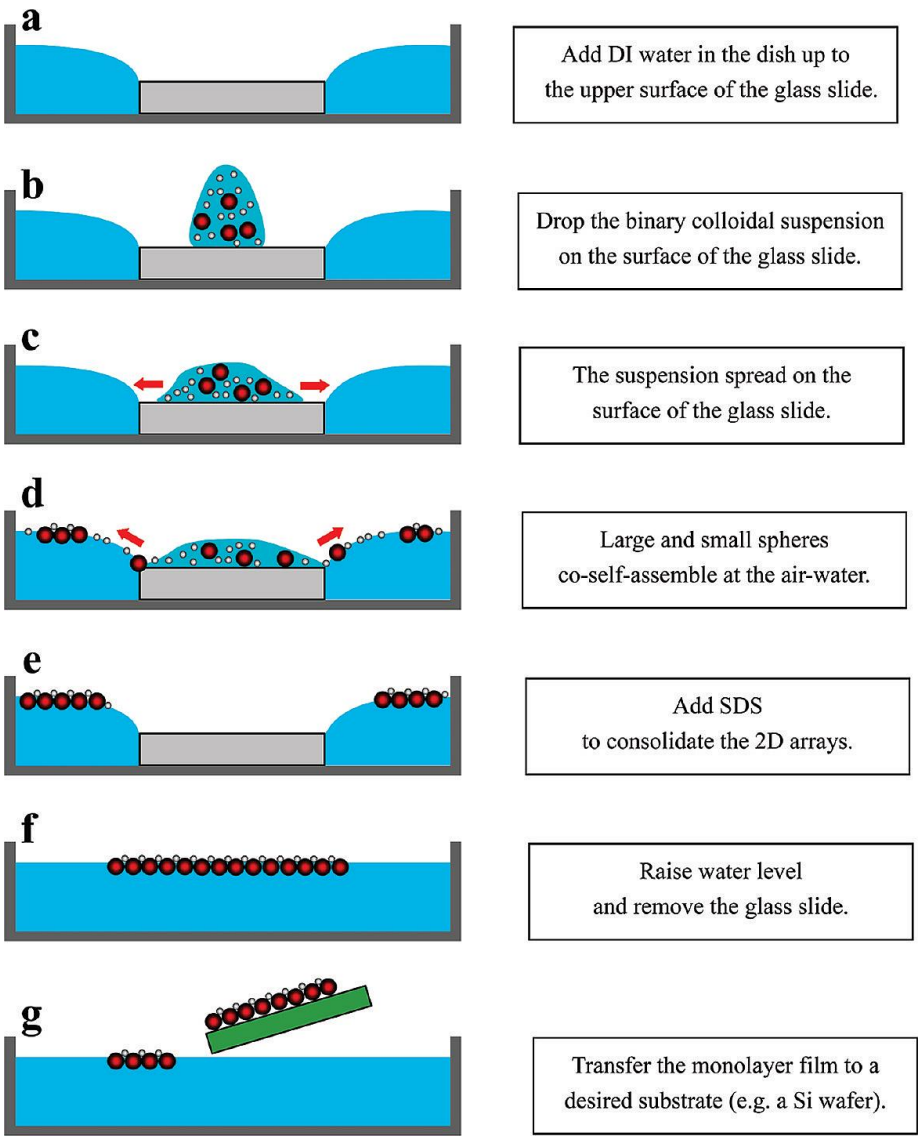

Figure 25: Procedure for the fabrication of 2D colloidal monolayer. [95]

This process has been modified for the creation of HCP monolayers of spherical nanoparticles in this thesis, were steps a – d were performed as described with uniform particle sizes. After the particle distribution on the substrate and surrounding water, the surrounding water was removed slowly and the substrate was dried by nitrogen and removed from the liquid, carrying the evenly dispersed particles on top (see chapter 3.3.1). With this technique, the hydrodynamic flux of particle solution from the substrate to the surrounding water spread the particles over the substrate surface.

3 Materials and Methods

This chapter shows all materials used and methods applied in producing the electrochemical sensor by following the process flows. The sensor evaluation measurements and sensor modification methods conclude this chapter.

3.1 Sensor Production

The sensor arrays were produced in a micromechanical bottom-up process involving optical lithography, vapor deposition and reactive ion etching. The equipment used was available at the Applied Physics Department of the University of Tübingen and the *Center for Light-Matter Interaction, Sensors & Analytics* (LISA$^+$).

3.1.1 Optical Lithography

Optical Lithography was used to create structured shapes of electrodes, feed lines and bond pads on the substrate. As substrate, 4inch borosilicate glass wafers by *Siegert Wafer GmbH* were used. Positive photoresist ma-P 1205 by *micro resist technology* was used in combination with the corresponding developer solution ma-D 331S. Hexamethyldisilazane (HMDS) mixed in propylene glycole methyl ester acetate 1:19 was utilized as an adhesion promoter and obtained from *Carl Roth GmbH*. Chrome-on-glass lithography masks were designed by computer assisted design (CAD) using the software AUTOCAD, version 2016 student, by *AutoDesk Inc.*, manufactured by *Compugraphics Jena* and can be seen in chapter 4.1.

All photolithographic steps were performed in the clean room of the University of Tübingen facility of LISA$^+$. In total 3 lithography steps were performed to create the different layers of the sensor, which only differed in exposure and reaction times. A full process flow can be seen in Table 1. Here, the general procedure is described.

The wafer was rinsed with ultrapure water and blow-dried by nitrogen gas, then placed on a rubber ring on the spinning chuck of the Convac 1001 spin coater combined with parameter control panel Siemens Coros OP15, and its surface covered completely with HMDS. HMDS splits into trimethylsilyl and reacts with the hydroxyl groups naturally present at the silicate surface of the wafer, thus changing the surface charge to hydrophobic and thereby enhancing the adhesion of the photoresist. This process was given a reaction time of 15 seconds, before the wafer was spun dry for 30 s at 3000 rpm. Following immediately, 6 ml of photoresist were

pipetted onto the wafer without creating air bubbles in a way to completely cover the surface and spun dry with the same settings. The wafer was then placed directly onto a 95 °C hot plate for 60 s to perform the soft bake of the resist and evaporate the solvent. After a cool-down period in a glass petri dish for several minutes, the wafer was exposed to UV light (350 nm Hg lamp, 210 W) using the chrome-on-glass shadow masks in the mask aligner MA6/BA6 by *Süss MicroTec AG* for 45 s with hard contact of mask and wafer. Following the exposure, the wafer was placed into a glass dish, dowsed with developer solution and developed for 45 s while swiveling the dish to softly stir the solution. Afterwards, the wafer was rinsed with ultrapure water and blow-dried by nitrogen gun.

The vapor deposition process, which deposits the metals composing the electrode structures, feed lines and bond pads, is described in the following chapter. In order to strip the remaining resist after the deposition, the wafer was placed upside down into a glass dish by use of spacer-pins, designed in-house, to avoid contact of the structured surface and the bottom of the glass dish. The dish was filled with acetone and placed in an ultrasonic bath for several minutes until all excessive resist is removed, taking the excessive metal material with it, only leaving the structured areas on the glass wafer. The wafer was then rinsed with clean acetone and immediately with isopropyl alcohol (IPA) and ultrapure water and blow-dried by nitrogen gun.

3.1.2 Vacuum Deposition

Vapor deposition technique was utilized to deposit metals on the previously structured lithography resist on the wafer substrate. Therefore, the wafer was placed into a 4inch holder and installed upside down on the carousel of the evaporation unit *Pfeiffer PLS 570*, thus facing the target material source on the bottom of the vacuum chamber. Here, electron-beam vaporization and resistance-heated vaporization is possible. Since two materials, titanium as adhesion promotor and gold as actual conducting material, were needed, both vaporizers were used successively. Titanium was provided in a crucible, 999.9 ‰ pure gold was ordered as nuggets at *Agosi AG* and placed in a tungsten evaporation boat obtained from *umicore AG*. The substrate was placed directly above the titanium target for titanium deposition and turned over the gold boat for gold deposition. The vacuum for deposition processes was at least 5 x 10^{-6} mbar, e-beam current for titanium evaporation was 60 mA and current for gold

evaporation was 2.2 AU[1]. 10 nm titanium was deposited, followed by 100 nm gold and again 10 nm titanium. The deposition rate for each material was measured internally by an oscillating crystal with a deposition controller Model 80 by *Telemark*.

A sacrificial chromium layer is needed to perform the final etching of the sensor after all layers have been deposited. This is done similar to the deposition described above. Chromium is deposited by electron-beam vaporization and the material is provided in a crucible and vaporized with an e-beam current of 20 mA. 100 nm of chromium provide a sufficient protection of the underlying layers during RIE.

3.1.3 Plasma-enhanced chemical vapor deposition (PECVD)

The PECVD unit Plasma lab 80 plus by *Oxford Instruments* was used to produce amorphous silicon nitride (SiN_x) passivation layers on top of the electrode structures. This unit has a 13.56 MHz driven parallel plate reactor with a 240 mm substrate electrode and a shower head gas inlet optimized for PECVD. The plasma chamber was pre-heated to 300 °C and conditioned with SiN_x by depositing material into the chamber without the substrate present. Therefore, 0.864 SLPM silane gas (SiH_4) and 14.6 sccm ammonia gas (NH_3) were pumped into the chamber at a process pressure of 1 Torr and a RF power of 20 W. The deposition onto the substrate was done subsequently at the same parameters with a deposition rate of 20 nm/min, producing 300 and 400 nm as inter-electrode passivation, while the bond pads were covered by a square alumina hard mask (Figure 26) to prevent coverage with SiN_x. A 200 to 400 nm final passivation layer was deposited on the top electrode structures. The layer thickness was further verified by use of a *Dektak 3030ST* Auto Surface Texture Profiler.

[1] Arbitrary Unit

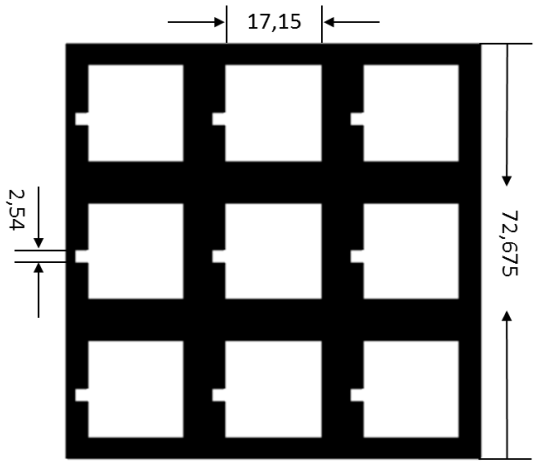

Figure 26: Design of alumina hard mask for bond pad protection, dimensions in [mm].

3.1.4 Reactive Ion Etching

Reactive ion etching was utilized to remove SiN_x from structures like the top electrodes and the inter-electrode passivation in the pores of top- to bottom electrodes, as well as the bond pads of the top structure. This is necessary to open the reactive surface of the top electrode, the pores between top- and bottom electrode and to be able to contact the electrodes via the bond pads and achieved in the RIE unit of the Plasma lab 80 plus by Oxford Instruments. The etch-gases were selected correlating to SiN_x. Therefore, 45 sccm of tetrafluormethane gas (CF_4) and 5 sccm of oxygen (O_2) gas were pumped into the reaction chamber at a process pressure of 0.1 Torr and RF power of 50 W and 20 °C. The substrate was placed in the reaction chamber and etched for 10-12 min. The result was verified under the microscope for free and clean metal surfaces on top electrodes and bond pads as well as in electrochemical measurements.

The RIE was also used for surface activation where adhesion needed to be promoted between two substances. Here, oxygen gas was used to increase the surface energy and hydrophilicity. The substrate was placed in the reaction chamber and O_2 gas was pumped into the chamber at a rate of 50 sccm at a process pressure of 0,1 Torr and RF power of 100 W at 20 °C. A reaction time of 8 seconds was sufficient to activate the surface.

3.1.5 Post production preparation

Since the sensor production took place on a 4inch wafer, the individual arrays needed to be separated before use. This is done utilizing the programmable wafer saw DISCO DAD321, provided by LISA$^+$. The wafer was covered with photolithographic resist as a protection layer

against glass dust as previously described in chapter 3.1.1 without the use of HMDS. It was placed on adhesive wafer-tape and mounted on the dicing chuck. The cutting was done using the glass saw blade P1A851 by *Diamond Blade Japan* at a cutting speed of 1 mm/s to produce 24.225 x 24.225 mm^2 single sensor arrays. After the cutting, the lower right corner of the single array was removed using fine sandpaper to fit the measurement socket. The protective resist was removed by cleaning with acetone, IPA and ultrapure water and the array was blow-dried by nitrogen gun.

After the RIE process, to open the top electrode surface and the pores between top- and bottom electrode, the chromium sacrificial layer was removed by wet chemical etching in TechniEtch Cr01 by *MicroChemicals GmbH*. Therefore, the sensor array was placed in a glass dish containing the etch solution while swiveling the dish to softly stir the solution for several minutes. The array then was rinsed with clean etch solution again and rinsed off with ultrapure water and blow-dried by nitrogen gun.

The following table gives an overview of the process steps that create the complete sensor array. For the flexible polyimide sensor, several aberrations had to be done and the respective process steps can be seen in chapter 3.3.2.

Table 1: Process flow of sensor array production

Process	**Layer created**	**Materials and Parameters**
Lithography I	Resist structure bottom electrode	Resist Ma-P 1205, Developer ma D-331S Bottom Electrode mask, exposure time 45 s, development time 45 s
Vacuum Deposition I	Bottom Electrode	Titanium 10 nm, Gold 100 nm, Titanium 10 nm
Resist Lift-Off I	Structured bottom array	Acetone, IPA, ultrapure water
PECVD	Inter-electrode passivation SiN_x 300 – 400 nm	SiH_4, NH_3, 300 °C, pressure 1 Torr, RF power 20 W
Lithography II	Resist structure top electrode	Resist Ma-P 1205, Developer ma D-331S Top Electrode mask, exposure time 55 s, development time 50 s
Vacuum Deposition II	Top Electrode	Titanium 10 nm, Gold 100 nm,

		Titanium 10 nm
Resist Lift-Off II	Structured top array	Acetone, IPA, ultrapure water
PECVD	Final passivation SiN_x 200, 400 nm	SiH_4, NH_3, 300 °C, pressure 1 Torr, RF power 20 W
Lithography III	Protective layer	Resist Ma-P 1205, Developer ma D-331S Etch mask, exposure time 45 s, development time 45 s
Vacuum Deposition III	Etch structure	Chromium 100 nm
Isolation of arrays	Single sensor array	Sacrificial resist, acetone, IPA, ultrapure water
RIE	Top electrode and pore structure	CF_4, O_2
Chromium Etch		TechniEtch 01, acetone, IPA, ultrapure water

3.2 Sensor Evaluation

The produced sensor array was evaluated electrochemically by use of the redox active substances potassium hexacyanoferrate and dopamine hydrochloride and optically by scanning electron microscopy. The measurements were performed to evaluate the structural design and production as well as the stability of the sensors electrodes.

3.2.1 Measurement Setup

The measurement setup consisted of a computerized eight-channel multi-potentiostat model 1000C by *CH Instruments*, a PC unit running the potentiostat software CHI 1000C Electrochemical Analyzer, an alumina faraday cage and several alligator clip holders. The potentiostat had a minimum current resolution of 0.0015% of the set current range, minimally 0.3 pA. As reference electrode, a silver/silver chloride pellet electrode by *Harvard Apparatus GmbH* in 2.0 mm diameter was used. All 24 electrode connections, reference, counter and working electrode for 8 channels, were fed into the faraday cage and set up as a 2-electrode setup, with all counter and reference electrodes connected over a silver wire and working electrodes clamped on the respective electrode on the sensor array, placed into a connecting socket. The connecting socket was build in-house by the mechanical workshop of the Applied

Physics Department of the University of Tübingen, fitting the used 64-pin-measurement sockets by Yamaichi. These measurement sockets were attached to a printed circuit board, designed and build by the electrical workshop of the Applied Physics Department of the University of Tübingen, to allow easy connection of the alligator clamp electrode connectors of the potentiostat. The setup can be seen in Figure 27 and an electric circuit scheme is shown in Figure 28, where a bottom and top electrode of one electrode pair are connected as 2 separate working electrodes, using the same reference electrode.

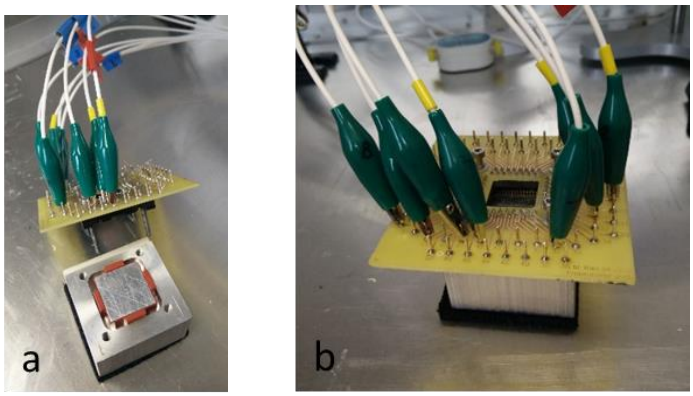

Figure 27: a) Connecting socket and b) printed circuit board with working electrode clamps attached.

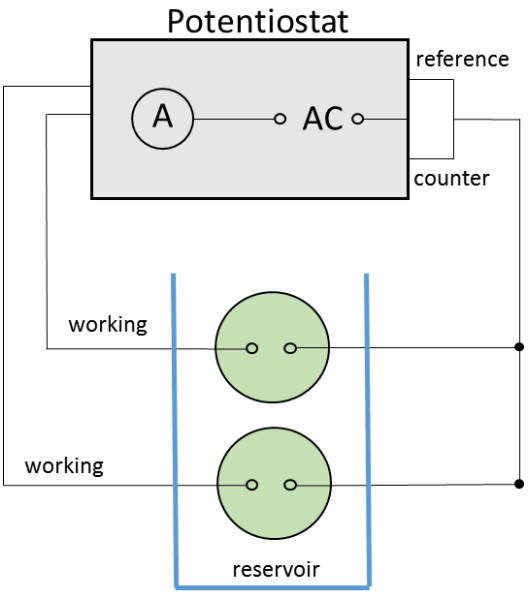

Figure 28: Electric circuit scheme for a 2-electrode setup containing one set of electrodes, bottom and top.

To create a reservoir for the measurement solution, either a ring of modeling clay was formed and pressed onto the fabricated sensor, or, for a more permanent reservoir, a glass ring of 10 mm inner diameter and a height of 8 mm was permanently fixated on the sensor array by PDMS (Figure 29).

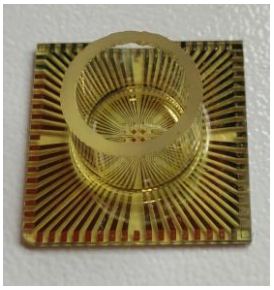

Figure 29: Liquid reservoir on sensor array.

The sensor was placed into the measurement socket with the circuit board screwed on tightly to assure good contact of the connecting pins to the bond pads. The reservoir was filled with measurement solution containing a redox active substance and the pellet reference electrode was lowered into the solution to close the circuit.

In the potentiostat software, the respective measurement technique was chosen. Two kinds of measurements were performed, amperometric I-t curve and cyclic voltammetry.

3.2.2 Measurement Solutions

The basis for all measurement solutions was a 0.01 mol/l phosphate buffered saline solution (PBS), prepared from tablet obtained from *Sigma-Aldrich GmbH*, solved in ultrapure water. As test solution, potassium hexacyanoferrate(II) was prepared in PBS in various concentrations. Dopamine hydrochloride was obtained from *Sigma-Aldrich GmbH* and made fresh for each measurement by dissolving in PBS, sheltered from light and kept in the refrigerator. Substances were weighed on a Kern ALJ250-4AM precision balance by *Kern&Sohn GmbH* with a reading precision of 0.100 mg, linearity of 0.300 mg and reproducibility of 0.400 mg. Dilutions were prepared with standard Schott graduated cylinders and PIPETMAN automated pipettes obtained from *Gilson Inc.*

3.2.3 Fluidic Setup

The fluidic setup was obtained from *Fluigent GmbH* and consisted of a flow control system MFCS-EZ, 2 liquid reservoirs FLUIWELL-1C, a flow rate platform FLOWBOARD, 2 FLOW UNITS model L, and connecting tubes with 1/16inch outer and 500 µm inner diameter. The system was controlled via the MAESFLO software version 3.2. Figure 30 shows the system setup as pictured by the manufacturer.

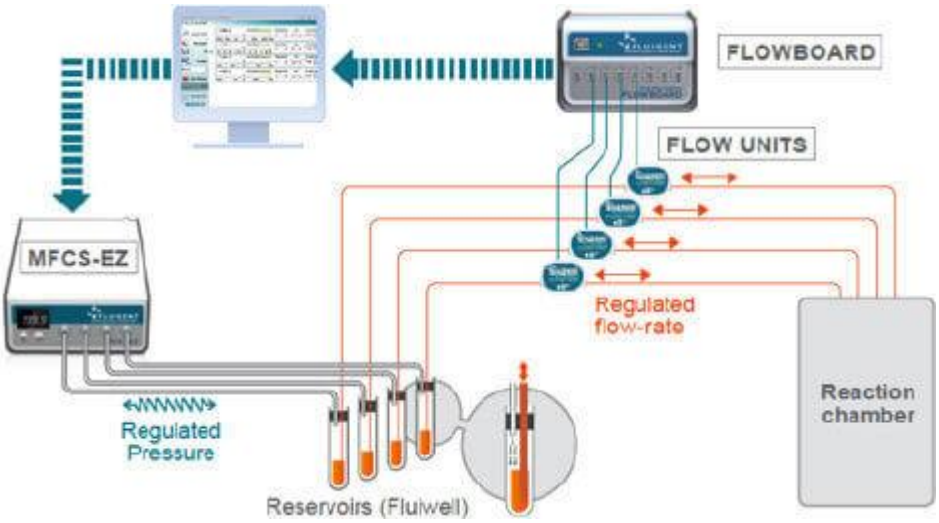

Figure 30: Schematic of fluidic setup by Fluigent GmbH. [97]

The fluidic chamber was designed to fit the requirements of the sensor chip and measurement setup. An alumina casting mold was build in-house by the mechanical workshop of the Applied Physics Department of the University of Tübingen, to produce fluidic chambers made of cured PDMS. Therefore, the mold was wrapped with adhesive tape to create a reservoir and liquid PDMS (Sylgard 527) by *Dow Corning* was poured on the mold without trapping air bubbles and cured at 60 °C in a heating cabinet for several hours. As a reference electrode, a 99.99% pure silver wire by *Advent Ltd*. was chlorinated at one end in Clorox solution, containing 2.8 wt% sodium hypochlorite, and taped to the mold to be situated in the center of the chamber. The resulting chamber had 2 inlets and one outlet to be connected with the tubing of the setup. The chamber diameters were 5.8 x 11 x 2 mm. In order to achieve a tight fitting of the tubing to the chamber, liquid PDMS was poured on the connecting spots and cured. The chamber bottom was then also covered with liquid PDMS and carefully placed on the sensor array and cured.

Figure 31 shows the alumina casting mold, the resulting chamber and a chamber mounted on a sensor array by PDMS with the reference electrode silver wire attached.

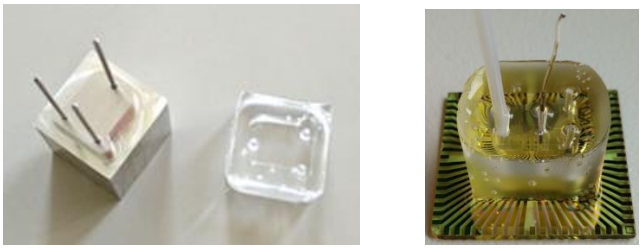

Figure 31: Casting mold, PDMS fluidic chamber and chamber mounted on a sensor array

3.2.4 Cell Culture Preparation

The PC12 cells, kindly provided by the workgroup of Prof. Dr. Offenhäuser at the Forschungszentrum Jülich, were thawed, the stabilizing dimethyl sulfoxide was removed and the cells were cultured under standard conditions in Dulbecco`s Modified Eagle Medium (DMEM) with added 10 % fetal bovine serum and 1 % penicillin-streptomycin obtained from *Sigma-Aldrich GmbH*. Culture conditions were 37 °C, 5 % CO_2 in culture flasks.

Sensor arrays containing a glass ring reservoir were immersed in 70 % ethanol for several hours, rinsed with ultrapure water and dried by nitrogen gun. The sensors were sterilized via UV germicidal irradiation in a *Vilber* UV chamber for 8 minutes with a wavelength of 312 nm. Following the sterilization, the sensors were kept in a sterile glass petri dish and the surface activation was performed utilizing the RIE unit of the Plasma lab 80 plus by Oxford Instruments with O_2 gas set to 50 sccm, RF power to 100 W, pressure to 0.1 Torr and temperature at 20 °C for a duration of 8 seconds. All following procedures were performed in the sterile clean bench environment using the *Safemate* 1.2 Vision clean bench.

Immediately after the surface activation by O_2 plasma, sterile 0.01 % poly-l-lysine solution obtained from *Sigma-Aldrich GmbH* was pipetted into the reservoir of the sensor to cover the entire surface. The sensors were stored in a sealed glass petri dish in the refrigerator overnight. Shortly before the cell application, the sensors were rinsed twice with sterile water and set to dry in the sterile clean bench.

Cultured PC12 cells were rinsed with sterile PBS solution and incubated with 5 ml trypsin to remove the adhesive cells from the incubation flask. 5 ml DMEM was added and the cells were centrifuged for 2-4 min at 600 rpm at room temperature using the *Heraeus* Biofuge Primo R. The medium was removed and cells resuspended in clean DMEM to dilute to preference and pipette into the sensor reservoir. After an attachment period of several hours, the reservoir

was filled up with DMEM and the cells were incubated overnight. To prevent excessive medium evaporation due to the small amount, the sensor was placed onto an elevation within a sterile glass beaker filled with sterile water and loosely covered by a glass dish.

In order to enhance the dopamine excretion of PC12 cells in certain experiments, the culture on the sensor was incubated with 3,4-Dihydroxy-l-phenylalanine (L-DOPA) obtained from *Sigma-Aldrich GmbH* in a final concentration of 100 µmol/l in DMEM for 2 hours prior to the measurement. 30 minutes before a measurement the medium was washed off twice with fresh DMEM.

3.2.5 Measurements

All measurements were performed at room temperature in non-sterile environment.

Since all measurement solutions were based on water, the potential range for measurements was limited by the electrochemical window for water and the potentials were chosen to cover the oxidation and reduction potential of hexacyanoferrate and dopamine, ranging from -0,4 to 0,7 V. The settings of scan rate, sensitivity, sample interval, sampling time, or in cyclic voltammetry number of sweep segments, were chosen to fit the requirements of each measurement. All sensor arrays were tested electrochemically before experimental measurements were performed. Therefore, 0.2 mol/l potassium hexacyanoferrate(II) was used. Both partner electrodes, top and bottom of one set, had to show a reaction to ongoing processes of the other, perform oxidation and reduction reaction alternately and remain electrically passivated to allow a stable measurement over the course of the testing.

Where varying concentrations or solutions were tested, the measurements were performed from lowest to highest concentration to prevent contamination. All sensor reservoirs and the reference pellet electrode were rinsed with ultrapure water and blow-dried by nitrogen gas when different solutions were being used successively. In fluidic measurements the tubing and fluidic chamber was rinsed with PBS in between measurements.

Measurements containing dopamine solution were performed immediately after the preparation of the solution and were limited to a time frame of 10 min, since the process of oxidation of dopamine in solution cannot be prevented.

Measurements on cultivated PC12 cells were performed at room temperature without fumigation with CO_2 and therefore kept as brief as could be managed. Cell stimulation was

induced by addition of varying amounts and concentrations of potassium chloride (KCl) in PBS into the reservoir during measurement. Both, DMEM and 0.01 mol/l PBS solution were used for cell culture measurements and therefore preheated and applied to the culture reservoir of the sensor 10 minutes prior to the experiments to allow buffering of DMEM in the CO_2 incubation chamber. Following the measurement, where possible, the electrode coverage by PC12 cells was verified by optical microscopy, using a *Zeiss* Microscope Axio Scope setup with CCD camera Axiocam.

3.3 Sensor Modifications

Modification of the existing sensor array towards sensitivity enhancement and implantability is described in this chapter. Two attempts have been made. Nanopores were produced to replace the lithographic 5-µm-pores of the top electrode by Nanosphere Lithography and flexibility is pursued by polyimide as a substrate and passivation for the sensor array.

In both attempts the original design was modified for the top electrode, which was reduced in diameter in order to avoid boundary effects, arising from alignment error and intensive RIE. The resist structure and the resulting protective Chromium layer were processed with a lithography mask layout of smaller top electrode diameter. The resulting diameters are 400 nm for the large, 200 nm for the medium and 80 nm for the small electrodes. In order to compare the modified sensors to the original design, original sensors were produced with the top electrodes of smaller diameters as well and are the source for comparative measurements.

3.3.1 Nanopores by Nanosphere Lithography

For the modification of the sensor array towards nanometer sized pores, the sensors were manufactured as described in chapter 3.1 with the difference, that the top electrodes were produced by use of the diameter-reduced electrode lithography mask not containing the pore design. This resulted in electrode structures without pore holes, which then could be created by nanospheres as shadow mask for following etching processes.

Polystyrene (PS) nanospheres (NS) with different surface coatings and diameters were obtained from *Polyscience Inc*. The particles were originally solved in water and had to be transferred in and diluted with 99.9% pure ethanol, obtained from *Ridel de Haën*. The

following particles and diameters were tested for the creation of a hexagonally closed packed (HCP) monolayer production:

Carboxylate-NS	COOH-NS	500 nm
Sulfate-NS	SH_4-NS	500 nm
Amino-NS	NH_3-NS	500 nm
Hydroxylate-NS	OH-NS	100 nm

All stock solutions had a concentration of 2.5 wt% in water. To allow fast evaporation and thereby the even spread of particles on the sensor surface, 1 ml of the stock solution was centrifuged at 4000 rpm for 6 min using the *Rotilabo* microlitre centrifuge *Gusto* and 0.5 ml solution was removed and replaced by ethanol. This was repeated twice and the desired Nanosphere concentration was obtained by adding ethanol accordingly. The concentrations tested were 1.25, 2.5, 5, 10 and 15 wt% spheres in ethanol.

The spheres were deposited in two versions either directly on top of the top electrode structure already etched free from SiN_x passivation, or on top of the SiN_x final passivation layer. The two versions were spin coating of particles and a variation of the Air-Water-Interface-Self-Assembly *AWISA* [95], [96] (see chapter 2.7).

Before the Nanosphere deposition, the sensor surface was activated by oxygen plasma utilizing the RIE unit of the Plasma lab 80 plus by *Oxford Instruments* with an O_2 gas flow of 50 sccm, RF power to 100 W, pressure to 0,1 Torr and temperature at 20 °C for a duration of 10 s. In order to prevent the rebuilding of non-polar hydrogen bonds on the surface, the sensor was kept in ultrapure water and dried by nitrogen gun only shortly before Nanosphere deposition.

For spin coating, a K.L.M spin coater by *Schaefer Technologies GmbH*, was used. The substrate, a sensor array with the dimensions 24,225 x 24,225 mm^2, was placed on the spin coater and 5 µl of particle solution was pipetted on the resting substrate and rotated at varying rotation speeds from 10 to 33 rps for 60 s (Figure 32).

Figure 32: Spin coating procedure. a) sensor chip dried in N_2 steam on the spin coating device; b) pipetting the particle suspension onto the sensor chip; c) sensor chip coated with particle suspension after spin coating.

The Air-Water-Interface-Self-Assembly was performed using a glass petri dish of 90 mm diameter, with the substrate already immersed in ultrapure water. Excess water was removed and the sensor surface blow-dried by nitrogen gun. This left the sensor surface free of water but the surrounding water at level with the substrate surface. 130 µl of the ethanol-particle solution was pipetted onto the sensor surface, spread out and when in contact with the surrounding water, flowed out into the glass petri dish, thus leaving the nanospheres assembled in a two-dimensional monolayer (Figure 33). In order to protect the surface from reflow of surrounding water, immediately after the contact of the two liquids the water was slowly reduced by pipette. The substrate was left to dry completely by evaporation.

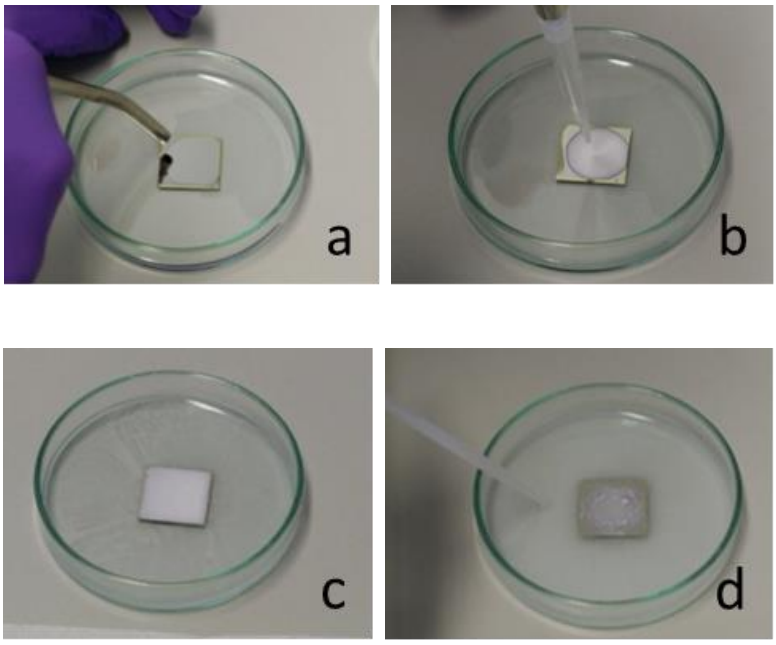

Figure 33: AWISA deposition technique sequence. a) drying sensor chip in water; b) particle suspension pipetted onto sensor surface; c) Nanosphere solution flowing into water; d) drying sensor surface and removel of residual water.

In order to create a wider distance between particles and smaller pore diameter, the particles were reduced in diameter by RIE with oxygen plasma for 90 s to 120 s at the following settings: O_2 gas 50 sccm, RF power 50 W, pressure 0.1 Torr, temperature 20 °C.

To produce an etch mask, 100 nm chromium was sputtered onto the particle-covered surface to protect the underlying structure by use of the *Leibold* Univex 300 sputter coater and a solid chromium target, both provided by LISA$^+$. The nanospheres trapped in the chromium layer were removed by immersion in methyl isobutyl ketone (MIBK) for several hours followed by final ultrasonification for 20 min and cleaning in IPA and ultrapure water.

The etching of the pores needed to be adjusted to the version of nanosphere application. Applied to the final passivation layer, this layer needed to be etched down to the top electrode by RIE, followed by an ion-beam etching (IBE) process to pass through the titanium-gold-titanium layer of the top electrode and then followed by another RIE process to pass through the inter-electrode passivation. In case of the particle deposition directly on the top electrode, the final passivation was already removed from the electrode surface and the first etching was the ion-beam etch of the top electrode. The IBE was done using argon ions and the UniLab ion-beam device by *Roth & Rau AG* for 50 min at the following settings: Rotation speed 0.715 Hz, process pressure $1.2\mathrm{e}^{-3}\ \mathrm{mbar}$, mass flow 3.5 / 1.7 sccm, ion beam current 23 mA, ion beam voltage 302 V, acceleration current and voltage 1-8 mA and 700 V, for the cathode 17.2 mA and 11.4 V and for the discharge 1.65 mA and 33 V. The RIE was done as described in chapter 3.1.4. with an etch rate of approximately 40 nm/min. After the completed etching, the chromium protective layer was removed by wet-chemical etching as described in chapter 3.1.5.

Just as for the initially designed sensor, the evaluation of the pore production was done by electrochemical measurements as described in chapter 3.2.5. Additionally, optical and scanning-electron-microscopy (SEM) as well as focused-ion-beam (FIB) were utilized to verify particle distribution, etch success and pore production. Therefore, the sensor array was attached to a specimen pin stub by conductive silver varnish by *Acheson*, both obtained from *Plano GmbH*, and its surface was covered by a thin gold conductive layer, produced by a sputter coater *Cressington* 108. The SEM used was a *Jeol* JSM-6500F, the FIB was a Strata DB235 by *Fei*, both provided by LISA$^+$.

3.3.2 Flexible Polyimide Substrate

For the flexible version of the sensor array the same production steps as for the standard array described in chapter 3.1 were adapted for polyimide. SiN_x was replaced by polyimide as passivation layer. Additional process steps were necessary to ensure a working sensor production, such as an etching process after the creation of the inter-electrode passivation to open up the bond pads of the bottom electrode. Also, a sacrificial titanium layer on the glass substrate was necessary to be able to detach the produced flexible layer array from the glass wafer. The sequence of process steps, the layers created and the materials and parameters used can be seen in Table 2.

Two kinds of polyimides were used, PI 2610 and PI 2611 by *HD Microsystems GmbH*, with PI 2610 being lower on solid units, resulting in a lower viscosity and possibly thinner layer. PI application was done following the manufacturer`s recommendations by pouring the viscose liquid slowly, without trapping air, onto the substrate at room temperature and letting it rest for 20 seconds to relax the polyimide. An even layer was created by use of the spin coater Convac 1001. Various rotation speeds for the 2 polyimide products were tested in a 2 step process to create layers of different thicknesses. Settings for step 1 were 500 rpm for 10 s at a ramping of 10 AU, followed by step 2 ranging from 3000 to 9999 rpm for 90 s at a ramping of 10 AU. For low rotation speeds only, a soft-bake on a hotplate at 90 °C for 90 s, followed by 150 °C for 90 seconds was performed before the curing. The curing was done following the manufacturer`s recommendations, with the tempering in a programmable oven by *Heraeus*. The temperature was ramped up to 300 °C at 4 °C/min, held for 30 minutes and reversed, using a curing recipe created for our workgroup by Markus Westerhausen. Since polyimide has a poor adhesion to metal and vice versa, a surface activation using oxygen plasma was performed immediately before each new layer of material was produced, using the RIE unit of the Plasma lab 80 plus by *Oxford Instruments* with the same settings as described in chapter 3.2.4.

As the tempering oven would only fit substrates up to 50 mm in diameter, the glass wafer substrates had to be cut in 35x35 mm squares using the programmable wafer saw DISCO DAD321, provided by LISA$^+$, as described in chapter 3.1.5. and all process steps had to be performed for single array substrates.

Table 2: Process flow of flexible substrate production

Process	**Layer created**	**Materials and Parameters**
Vacuum Deposition Ti	50 nm titanium sacrificial layer	Titanium 50 nm
Wafer cut	Single substrate, 35x35 mm	Sacrificial resist, acetone, IPA, ultrapure water Disco DAD 321, saw blade P1A851 by Diamond Blade
Polyimide I	Bottom substrate layer	PI 2611, Spin coater Convac 1001 Hotplate, tempering oven
Lithography I	Resist structure bottom electrodes	Resist Ma-P 1205, Developer ma D-331S Bottom Electrode mask, exposure time 40 s, development time 35 s
Vacuum Deposition I	Bottom Electrode	Titanium 10 nm, Gold 100 nm, Titanium 10 nm
Resist Lift-Off I	Structured bottom array	Acetone, IPA, ultrapure water
Polyimide II	Inter-electrode passivation layer	PI 2610, 9999 rpm, 90 s, Spin coater Convac 1001, tempering oven
Lithography Bond Etch	Resist structure to etch bond pads	Resist Ma-P 1205, Developer ma D-331S Bond Etch mask, exposure time 40s, development time 35 s
Vacuum Deposition Cr	Protective layer	Chromium 50 nm
Resist Lift-Off Bond Etch	Structured Chromium with Bond pads free	Acetone, IPA, ultrapure water
RIE	Open Bond pads	50 sccm O_2, RF power 100 W, 0,1 Torr, 20°C
Chromium Etch	Removal of Chromium	TechniEtch 01, acetone, IPA, ultrapure water
Lithography II	Resist structure top electrode	Resist Ma-P 1205, Developer ma D-331S

		Top Electrode mask, exposure time 45 s, development time 40 s
Vacuum Deposition II	Top Electrode	Titanium 10 nm, Gold 100 nm, Titanium 10 nm
Resist Lift-Off II	Structured top array	Acetone, IPA, ultrapure water
Polyimide III	Final passivation layer	PI 2610, 9999 rpm, 90 s, Spin coater Convac 1001, tempering oven
Lithography III	Resist structure *etch layer* Electrodes and Bond pads free	Resist Ma-P 1205, Developer ma D-331S Etch mask, exposure time 40 s, development time 35 s
Vacuum Deposition Cr	Protective layer	Chromium 50 nm
Resist Lift-Off Cr	Structured chromium layer	Acetone, IPA, ultrapure water
RIE	Open electrodes, pores and bond pads	50 sccm O_2, RF power 100 W, 0,1 Torr, 20°C
Chromium Etch	Removal of Chromium	TechniEtch 01, acetone, IPA, ultrapure water
Detachment from wafer	Flexible array	Adhesive tape
Resizing to 24,225x24,225 mm^2		Scissors

With the final passivation attached and the electrode structure and bond pads etched open, the sensor was tested in electrochemical measurements similar to the standard sensor array described in section 3.2.1, with the flexible array still attached to the glass wafer fragment. Due to the larger size of the substrate, the connecting socket and printed circuit board could not be used. Instead, the sensor was placed on a measurement stage and connected via probe positioner needles on the respective bond pads. A ring of modeling clay was formed and pressed onto the fabricated sensor to create a preliminary reservoir to hold the measurement solution and reference electrode pellet (Figure 34).

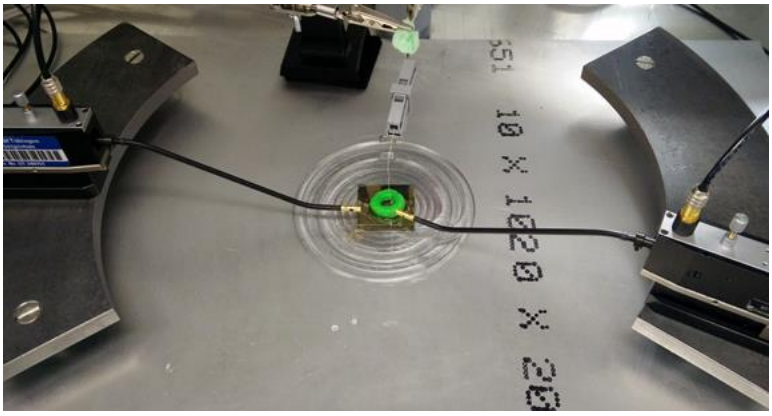

Figure 34: Flexible sensor array measurement setup. 2 probe positioners connect the working electrodes via bond pads, a preliminary reservoir holds measurement solution and the reference electrode pellet.

After the measurement, the sensor was detached from the wafer fragment by use of adhesive tape and the performance was measured again.

4 Results and Discussion

This chapter introduces the produced Redox-cycling sensor array and contains the evaluation of the sensor in voltammetric and amperometric measurements with stationary and fluidic solutions of potassium hexacyanoferrate and dopamine. Sensitivity, cycling efficiency and the general characteristics are key parameters to determine the sensors performance. Cell culture experiments furthermore show the measurements of cellular release of dopamine, simulating the physiological dopamine detection. The chapter is concluded with the modification by Nanosphere Lithography and the transfer to a flexible sensor array.

4.1 Sensor Design

The sensor design was based on a Multi Electrode Array. This structure consists of a planar arrangement of contacting areas (bond pads), connecting structures (feedlines) and the circular electrode structure. The circular structure was chosen to decrease possible fringe effects created at corners. A central positioning of the electrodes with wide distance to the bond pads was chosen to allow the positioning of a liquid containing reservoir and a fluidic chamber. Having the electrodes located closely together also enables the measurement of concentration variations and spatial-temporal resolution in fluidic measurements. As a redundancy, each electrode is connectable via two bond pads and feedlines. In total, 16 electrodes in 3 sizes are present, 4 with 500 µm, 8 with 250 µm and 4 with 100 µm in diameter. The sensor array is 24.2 x 24.2 mm in size. Figure 35 shows the layout and an enlargement of the electrode area with electrodes numbered for easier referencing.

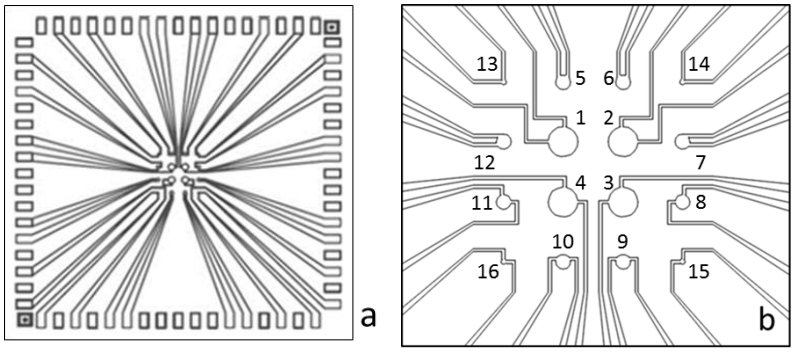

Figure 35: a) Sensor array layout with bond pads, feedlines and electrodes; b) 16 electrodes in 3 sizes, numbers for reference.

A 3-dimensional plane-parallel electrode positioning was chosen for this array. Since the materials were deposited in a bottom-up process, the spacing of top to bottom electrode can

easily be varied and be much smaller than in a coplanar, interdigitated structural array. The top electrode design mirrors the bottom electrode structure turned 180° horizontally. Thus, the feedlines do not overlap, the bond pads are not occupied twice and the design is kept simple. In order to increase the reactive surface and provide a confinement for the reactant, the top electrode was designed containing circular pore structures of 5 µm in diameter. Figure 36a shows the mask layout for the top electrode structure, Figure 36b shows an enlargement of the electrode surface and the pore structure, as well as the group logo.

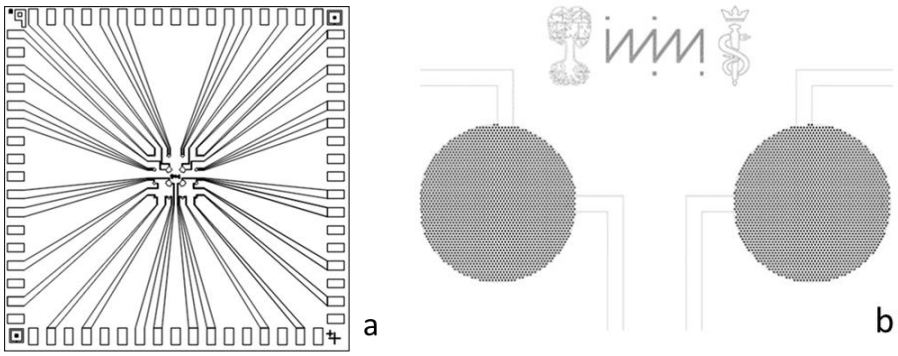

Figure 36: a) Sensor array layout of top electrode structure; b) Top electrode surface with pore structure and group logo.

Since optical lithography was used to create the structures, the 5 µm diameter of the pores was chosen in order to avoid problems of resolution, which would occur in smaller diameters, with the resolution of the UV-lithography process at 1 – 2 µm. The distance between pores was also designed to be 5 µm. This resulted in 2278 pores for the large electrodes, 569 pores for the medium and 90 pores for the small electrodes.

In order to maximize the output of each process batch, a 3 x 3 array of sensors was chosen for the chrome-on-glass lithography shadow masks. This correlates with a use of 4inch wafers, which is the maximum size usable in the mask aligner available. Figure 37 shows the mask layout for the bottom electrode, top electrode and the layout for the etch structure.

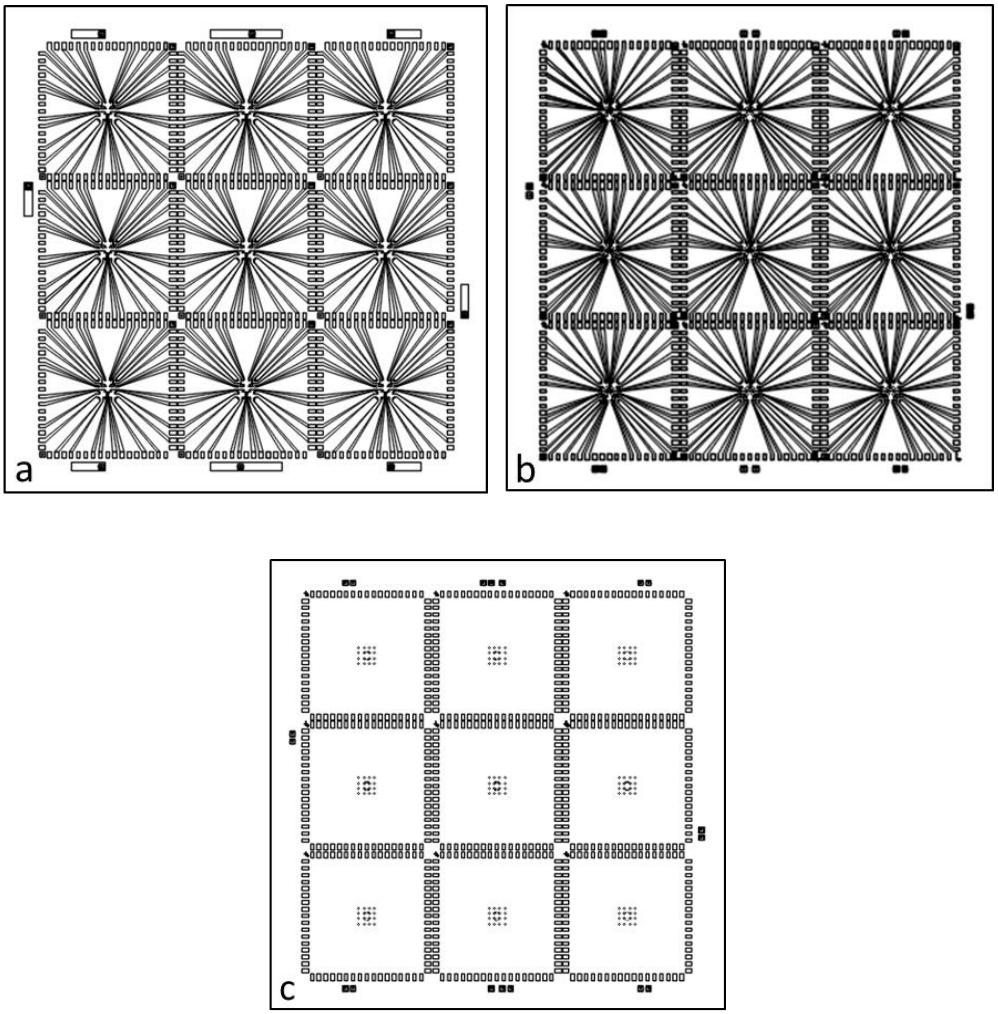

Figure 37: Lithography mask layout in 3x3 array of a) bottom electrode, b) top electrode, c) etch structures.

This design results in a 3-dimensional electrode structure containing pores, in which the reactant is spatially confined and can shuttle between electrodes, which are only several hundred nanometers apart.

Figure 38 shows a model drawing of the electrode structure and the pore, with a dopamine molecule being oxidized to Dopaquinone (DAQ) at the bottom electrode and reduced back to dopamine at the top electrode.

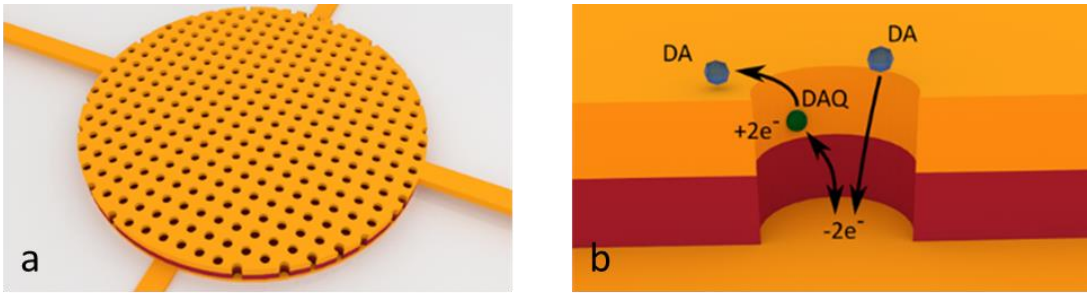

Figure 38: a) Model drawing of an electrode structure containing pores; b) Pore of top and bottom electrode (yellow) and the inter-electrode SiN_x passivation layer (red). DA enters the pore, gets oxidized at the bottom electrode and transferred to Dopaquinone and reduced back to dopamine. Graphics by Markus Westerhausen.

4.2 Sensor Production

The various successive production steps were chosen in correlation to the materials used, as to not interfere with previously produced layers in chemical exposure and temperature.

The adhesion promotor HDMS proved to be indispensable for the creation of stable and reproducible photoresist structures, that would withstand the development and lift-off procedure and allow the construction of uniform metal structures. This became obvious when resist structures would not remain on the glass wafer substrate without HDMS. Here, especially the production of the resist pillars, which allow the construction of pore holes within the top electrode, proved to be a challenge due to their small diameter.

The use of titanium as adhesion layer between gold and the amorphous SiN_x (see chapter 2.5.1) proved to be successful, since the layer structures were stable in ultrasonification and the cleaning, necessary for use and re-use of the complete sensors during measurements.

The passivation layer, consisting of amorphous SiN_x, was produced by use of low temperature SiN_x deposition, thus keeping the metal structure, consisting of titanium and gold, intact. PECVD processes with high temperatures to deposit SiN_x are known to produce a higher quality layer, with the pinhole density increasing and possible oxygen impurities at temperatures below 300 °C [76]. Due to a high surface-to-volume ratio of the 100 nm gold-layer structure and the possible melting of small gold clusters at a temperature below 600 °C [98] this process would not have been suitable, since creep of the gold structures would have been possible. Also, SiN_x layers deposited at temperatures of 300 °C or below show an increased etch rate in RIE [76] , which is preferable for the structuring of the passivation.

The inter-electrode passivation layer was kept as thin as possible to perform electrical passivation and to keep the electrodes as close to each other as possible. This resulted in a working structure with inter-electrode passivation of at least 300 nm to 400 nm thickness. Dimensions below 300 nm did not produce a sufficient passivation. Due to the volume resistivity of PECVD SiN_x of 10^{12} Ωcm, the passivation of 400 nm results in a theoretical resistivity of 40 MΩ, the passivation of 300 nm in 30 MΩ. These values are a magnitude of 10^4 larger than the largest resistivity necessary, which would be 1.1 kΩ for 0.2 mol/l potassium hexacyanoferrate(II) at 0.6 V and a produced current of 0.5 mA. Therefore, the necessary inter-electrode passivation thickness is not defined by the electric passivation properties of SiN_x, but rather the construction processes described in the following.

The final passivation of 400 nm proved to be sufficient. The low temperature PECVD process produced uniform and clean layers at the settings described in section 3.1.3, which were stable and successful in passivating the conductive structures.

The RIE process by use of CF_4 and O_2 showed good results in the removal of SiN_x and relatively clean etch areas. The presence of silicon grass was negligible and could be further reduced by prolonged RIE, leaving the metal surfaces free of residue.

Figure 39a shows a single square sensor array of 24.2 mm edge length, containing the bottom electrode structure and the inter-electrode passivation layer, Figure 39b shows, in addition, the top electrode structure and final passivation.

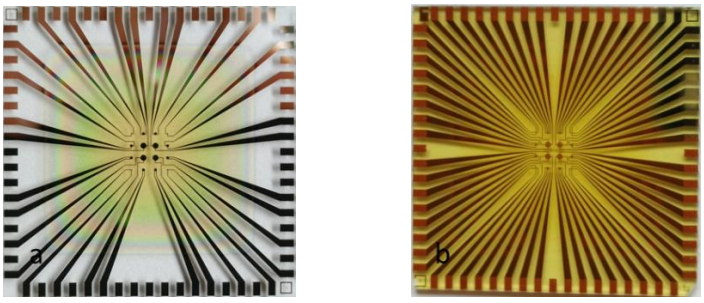

Figure 39: a) Bottom electrode and passivation; b) Top electrode and final passivation.

Due to the photolithographic structuring process, a perfect alignment of top to bottom electrode was unattainable. For a 4inch mask and wafer, the range of movement of the microscope eyepiece lens of the mask aligner was too small to examine the complete area. This resulted in more or less precise positioning of the top electrode onto the bottom

electrode. Therefore, the number of pores on each electrode, as well as the coverage of the bottom electrode surface by the top electrode, vary. This results in a varying ratio of reactive surface from bottom and top electrode. In best possible positioning, the percentage of possible pores on the large electrode was 99,3%, in the medium electrode 98,4% and the small electrode 90%. A good approximation for the reactive surfaces is given in Table 3 for each electrode size. For the top electrode, the total surface area consists of the electrode surface itself and the curved surface areas of the pores. For all electrode sizes, the top electrode surface area is significantly larger than that of the bottom electrode, where only the bottom plane of all pores counts as reactive surface. On average, the reactive surface of the top electrode is 3.5 times the bottom area for the large and medium electrodes, and 4 times that of the bottom area at the small electrodes.

Table 3: Surface Area of Bottom and Top Electrodes

Electrode Diameter [µm]	Surface Area Bottom [μm^2]	Surface Area Top [μm^2]
500	44 423	156 204
250	10 993	39 153
100	1 590	6 417

In the production of working sensor arrays, next to the structural mask alignment, the uniform illumination of the wafer area proofed to be a critical step as well. Non-uniform illumination created about 65% discharge in the number of successfully produced arrays, with underdeveloped structures on the one side next to properly developed areas.

The complete opening of the pores proofed to be critical as well. Due to the small diameter of the pores, combined with the low Young`s module and the tensile strength of PVD gold (see chapter 2.5.1), many of the pores within the gold layer of the top electrode would not open in the wet-chemical lift-off process described it chapter 3.1.1. This created top electrode structures with several clogged pores (Figure 41, Figure 42), which decreased access to the bottom electrode and reduced the output of working sensors, since the capped pores often created a short-circuit between top- and bottom electrodes. The same problem occurred at narrow structures along the feedlines, where the stripping process described in section 3.1.1 was not completely successful and a hammock-like gold layer remained between structures.

Also, the removal of excessive gold at the bottom structures left frayed edges, at which the ragged gold arched upward and could be the reason for defects in the inter-electrode passivation. An increase in exposure time under UV light during the lithography as well as an optimized positioning in the mask aligner, to reduce effected areas of non-uniform illumination, allowed the production of complete top electrodes in approximately 30% of produced arrays. Figure 40 shows a large top electrode with fully opened pores and only a small alignment error. Figure 41 and Figure 42 show an enlargement of clogged pores next to open pores still containing the inter-electrode passivation SiN_x.

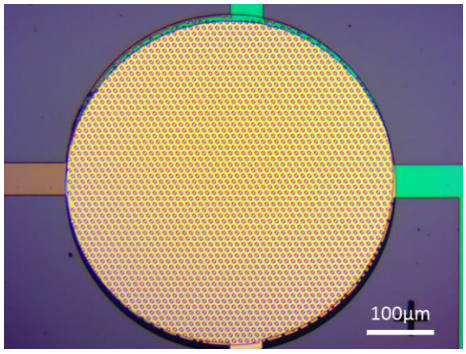

Figure 40: Electrode structure with top electrode (yellow) containing a complete pore structure and slight alignment error, top electrode and feedlines show in green due to SiN_x passivation.

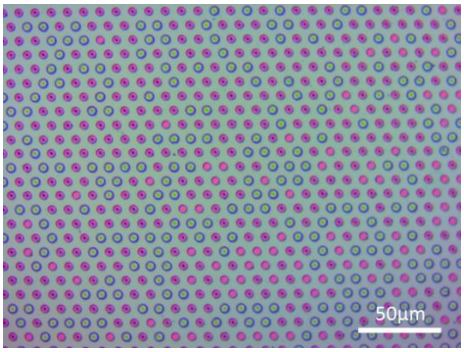

Figure 41: Enlargement of top electrode pores. Clogged pores (blue), open pores containing SiN_x (pink).

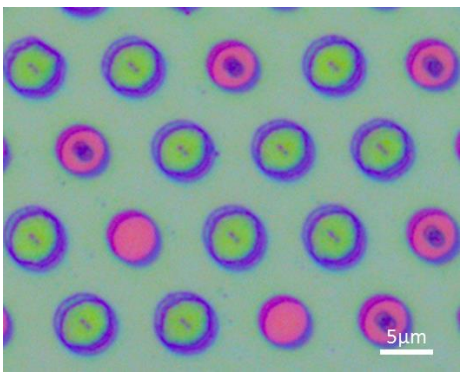

Figure 42: Pores in top electrode, open (green), clogged (pink), with depositions at the center.

As can be seen in Figure 42, the pore holes show a deposition at the center. This is most likely caused by the so called tea-leaf paradox [99] as described by A. Einstein in 1926. Here, the circular movement of the substrate during development (see section 3.1.1) causes the centripetal force and friction along the rim and bottom to create the boundary layers, where fluid rotation is slowed by friction and viscous effects. The centripetal force due to pressure gradient is dominant over the inertial forces from rotation and creates an inward secondary flow within the boundary layer. The flow converges at the bottom, where it traps the solved particles, and flows upwards to the surface. Higher up, the liquid flow meets the surface and flows outwards. The particles are too heavy to lift upwards and remain in the middle. This effect could not be eliminated, since the development of the structured resist could not be performed upside down like the stripping described at the end of chapter 3.1.1. Nevertheless, during a successful and complete stripping process with ultrasonification, the depositions could be removed also, leaving clean pores.

4.3 Sensor Evaluation

The successful sensor production was verified by electrochemical measurements. The RIE success in opening the electrode structure, the functionality of each single electrode, the passivation properties and the stability of the layer construction were tested by the application of an electric potential difference between bottom and top electrode, while both are connected through the measurement solution containing potassium hexacyanoferrate(II). The redox reaction and resulting current was recorded. In order to investigate the surface conditions and structural properties, SEM and HIM pictures were taken additionally.

4.3.1 Functionality

A properly functioning electrode array shows the independent half reactions of oxidation and reduction at the respective electrode as action-related dependence-current (see chapter 2.3.1 and 2, Redox Cycling). The substance generated at one electrode is transported by potential-induced diffusion to the partnering electrode and transformed again. This results in a mirroring current, displayed in the cyclic voltammogram. The functionality of the produced electrode array was tested by cycling either bottom or top electrode over the potential range from -0.4 to 0.7 V, while the respective partnering electrode is set to the fixed oxidation or

reduction potential of -0.4 V or 0.7 V against the reference electrode. The cycle starts at 0 V, turns to the negative with reversal at -0.4 V and reverses again at 0.7 V to stop at -0.4 V.

The following graphs display the voltammetric current flow for the reduced form of hexacyanoferrate(II), for the resulting 4 electrode-setting combinations and the 3 electrode sizes, large (black), medium (red) and small (blue). The concentration of reactive molecules is 0.2 mol/l in PBS, the scan rate is 0.2 V/s. All measurements were performed on sensor arrays with 400 nm inter-electrode passivation (see chapter 3.1.3). The current at the bottom electrode is displayed in solid lines, the current at the top electrode in dashed lines.

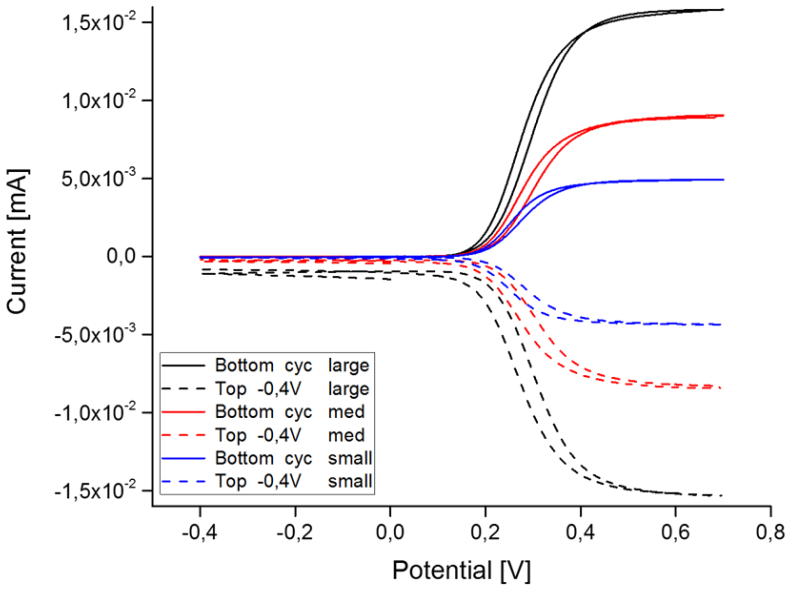

Figure 43: Redox current in 0.2 mol/l hexacyanoferrate(II): Bottom electrode cycling, oxidation current (solid lines), top electrode at fixed reduction potential -0.4 V (dashed lines), scan rate 0.2 V/s.

The bottom electrode, cycling over the potential range from -0.4 to 0.7 V, induces the oxidation of the reduced form of hexacyanoferrate(II) between 0.2 and 0.7 V with the main inclination between 0.2 and 0.4 V. A relatively steady current is produced between 0.4 and 0.7 V and a much smaller current is induced in the potential range from 0.2 to -0.4 V, where few oxidized molecules are present to be reduced. The partnering top electrode, set at the reduction potential of -0.4 V, immediately transforms the oxidized species hexacyanoferrate(III) back to the original hexacyanoferrate(II), as given in equation 13, chapter 2.3.2. Depending on the electrode surface area, the overall current produced is largest

for the large electrodes of 500 µm and gradually smaller for medium (250 µm) and small electrode (100 µm). As the sigmoidal curve indicates, the electrode functions as a micro-electrode at this setting, showing the effect of a convergent diffusion instead of a planar diffusion pictured in Figure 13. Here, the rate of mass transport in relation to electrode surface is increased, as is the current density. Since the large surface area of the top electrode is set to the reduction potential with only reduced molecules in solution and the smaller surface area of the bottom electrode is set to the generating potential, the effect of a macro-electrode does not occur. The potential shift in the range of 0.5 to 0.1 V to a more positive potential for the oxidation and a more negative potential for the reduction process shows the increase in overpotential needed, to drive the electron transfer for the second passing of the potential rage from 0.4 to 0.2 V and can be explained by the established depletion zone near the electrode surface, induced by the first reaction at the respective electrode potential.

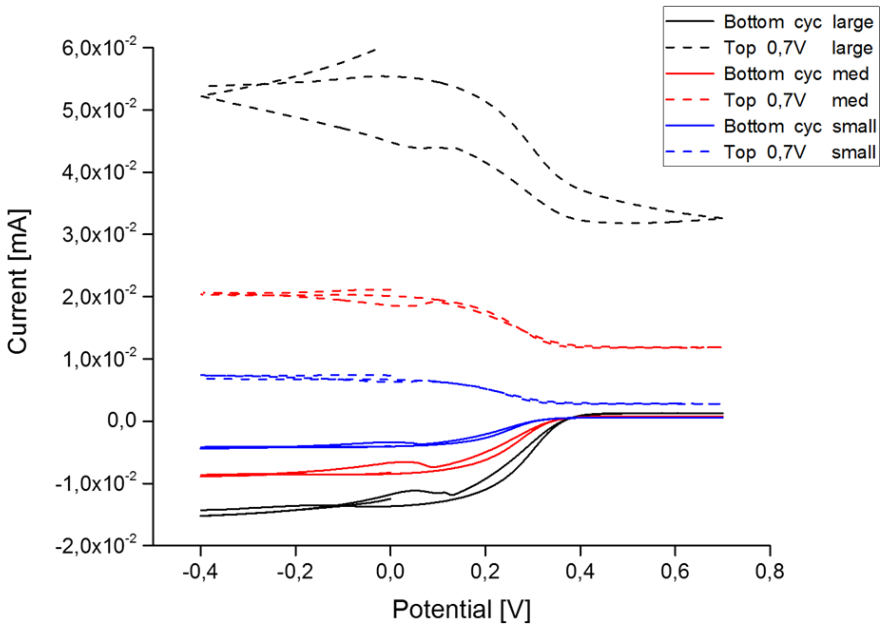

Figure 44: Redox current in 0.2 mol/l hexacyanoferrate(II): Bottom electrode cycling, oxidation current (solid lines), top electrode at fixed oxidation potential 0.7 V (dashed lines), scan rate 0.2 V/s.

With the bottom electrode cycling and the top electrode set to the oxidation potential of 0.7 V, the reduced form of hexacyanoferrate(II) is instantly and permanently oxidized at the top electrode, resulting in a constant positive current. The bottom electrode reduces the

generated oxidized molecules in the cycling range between -0.4 and 0.4 V, which in turn increases the amount of reactive molecules for the top electrode to oxidize and results in a reflected current increase. In the potential range between 0.4 and 0.7 V, the top electrode shows the constant oxidation, resulting in a size-dependent current for each electrode size. Very little oxidation takes place at the bottom electrode in that range, resulting in a current drop towards 0 mA. This is due to the constant oxidation of molecules at the top electrode and a resulting depletion of reactive molecules in the vicinity of the bottom electrode. Since a permanent oxidation takes place at the top electrode, oxidized molecules can easily diffuse into the bulk solution and are lost for the redox cycling. This is reflected in the difference in the induced current of bottom to top electrode, which is much higher at the top electrode than the bottom electrode. The large electrode shows a diffusion-controlled current gradient at this electrode setting, typical for a macro-electrode, as well as a large current-divergence between first and second cycle of the potential range from 0.4 to -0.4 V.

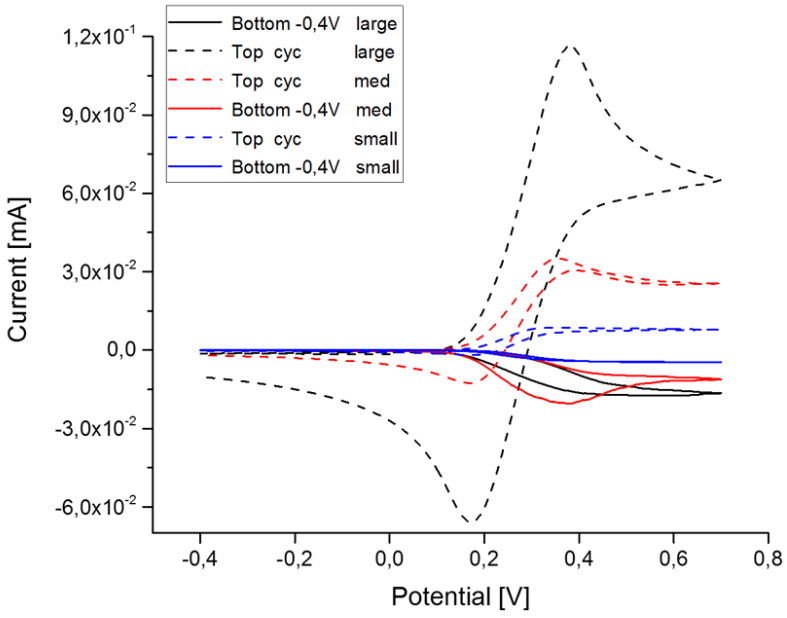

Figure 45: Redox current in 0.2 mol/l hexacyanoferrate(II): Top electrode cycling, oxidation current (dashed lines), bottom electrode at fixed reduction potential -0.4 V (solid lines), scan rate 0.2 V/s.

When the top electrode is cycling the potential range from -0.4 to 0.7 V and the bottom electrode is set to the fixed reduction potential, the top electrode shows the current-voltage

curve described in Figure 13 for a macro-electrode. This is due to the unlimited supply of reactive molecules for the top electrode, resulting in a diffusion controlled electron transfer reaction. In the potential range from 0.2 to 0.7 V, the produced oxidized molecules from the top electrode are reduced at the bottom electrode only in part, resulting in a much lower current for the reduction compared to the oxidation. This is due to the spatial orientation, where the oxidized molecules can easily diffuse form the top electrode into the bulk and only partly diffuse through the pore-channel to the bottom electrode. In the potential range from 0.2 to -0.4 V, only previously oxidized molecules of hexacyanoferrate(III) can be reduced at the top electrode during the cycling, which results in the reduction current, visible for the large and medium size top electrode in this graph. At this electrode setting, the current gradient develops from a macro-electrode process at the large and medium-sized electrodes towards a micro-electrode process for the small electrode, resulting in an increasingly sigmoidal gradient for a decreasing electrode size. This is also reflected in the potential, at which the oxidative peak-current is reached, which shifts slightly from approximately 0.4 V towards 0.3 V for the top-electrode sizes and is a result of the increasingly convergent diffusion and higher current density, that allows the peak current to be reached at a lower potential value.

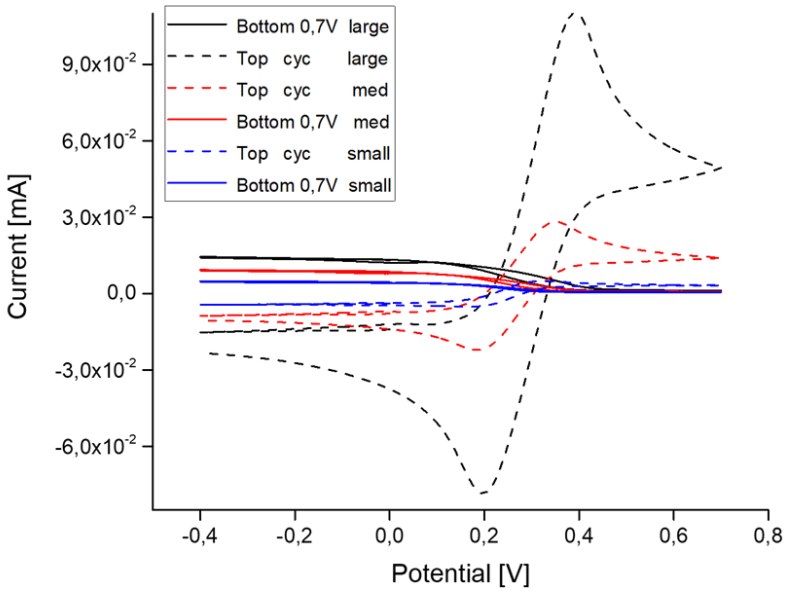

Figure 46: Redox current in 0.2 mol/l hexacyanoferrate(II): Top electrode cycling, oxidation current (dashed lines), bottom electrode at fixed oxidation potential 0.7 V (solid lines), scan rate 0.2 V/s.

With the top electrode cycling and the bottom electrode set to the oxidation potential of 0.7 V, the reduced form of hexacyanoferrate(II) is permanently oxidized at the bottom electrode, resulting in a constant positive current. This current decreases towards 0 mA when the top electrode cycles in the oxidative potential range and thus is in dominant competition for the reduced molecules. The top electrode again shows the diffusion controlled current-voltage curve as described for Figure 45 above. The loss of redox active molecules to the bulk is the same as described above, and results in the loss of oxidized and reduced molecules form the top electrode, which in turn might diminish the current at the bottom electrode for the reduced species lost to the bulk. The increasingly sigmoidal current gradient for decreasing top-electrode sizes, as well as the shift in potential for the oxidation peak-current is reflected again as described for Figure 45.

The voltammetric measurements of redox cycling in hexacyanoferrate(II) show the functioning of the individual electrodes and the coupled reaction to oxidative and reductive potentials. The effect of pore geometry and size of reactive area can be shown. The setting of the generating potential at the bottom electrode and the collecting potential at the top electrode shows a reflected current at each electrode with almost no loss of reactive species.

In the following amperometric measurement, the current over time is displayed for the 3 electrode sizes. The bottom electrode is set at the oxidative potential 0.6 V and the top electrode at the reductive potential of -0.1 V, the concentration is 0.2 mol/l potassium hexacyanoferrate(II).

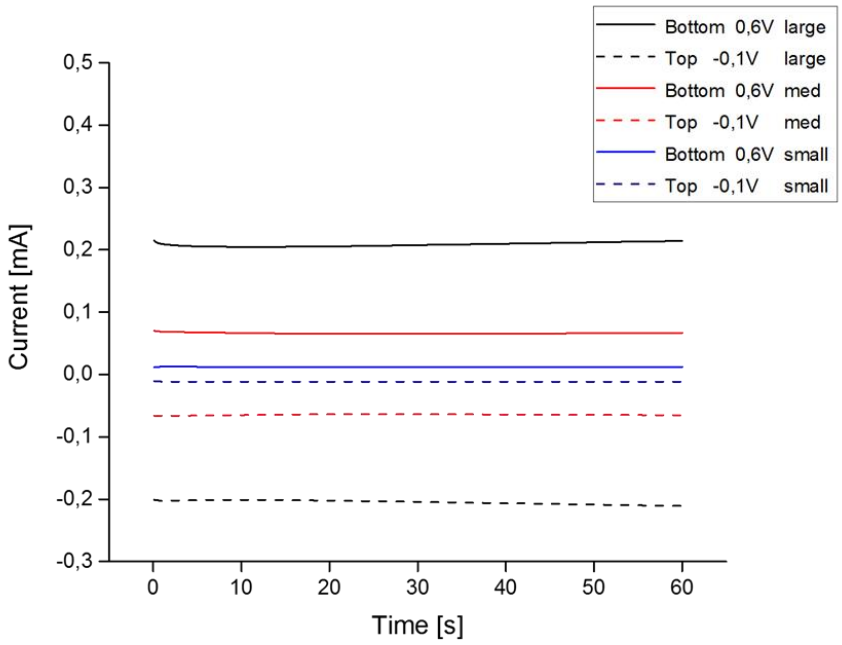

Figure 47: Amperometric measurement in 0.2 mol/l hexacyanoferrate(II): Bottom electrode set to oxidative potential 0.6 V (solid lines), top electrode set to reductive potential -0.4 V (dashed lines).

The size-dependency of the current becomes clear, when the 3 electrodes are compared. For the large electrode the current values after 30 seconds are 0.2076 mA for the generator electrode and -0.2041 mA for the collector electrode. The values for the medium electrode are I_{gen} = 0.0654 mA and I_{col} = -0.0638 mA and for the small electrode I_{gen} = 0.0122 mA and I_{col} = -0.0114 mA. The values of generator and collector current, meaning oxidation and reduction reactions, show minor divergence on all 3 electrodes, which is reflected in the cycling efficiency and closely investigated in chapter 4.3.3.

4.3.2 Sensitivity

The sensitivity of the sensor was tested by redox-cycling in measurement solutions of potassium hexacyanoferrate(II) in various concentrations, ranging from 0.001 to 0.2 M. Either the bottom or top electrode were cycled over the potential range from -0.1 to 0.6 V at 0.2 V/s, with the respective partnering electrode set to the reduction potential of -0.1 V. Since the reduced form is present in the solution, oxidation at the cycling electrode creates the reactive molecules hexacyanoferrate(III) to be reduced again at the partnering electrode and allows the comparison of the current-concentration relation.

The following graphs show the voltammetric current flow, exemplary on a large electrode, for the 2 settings with the bottom electrode cycling and the top electrode on reduction potential and vice versa (Figure 50, Figure 51). All measurements were performed on a sensor arrays with 400 nm inter-electrode passivation (see chapter 3.1.3). The same electrode was used to compare the concentration-dependent current. The current at the bottom electrode is displayed in solid lines, the current at the top electrode in dashed lines.

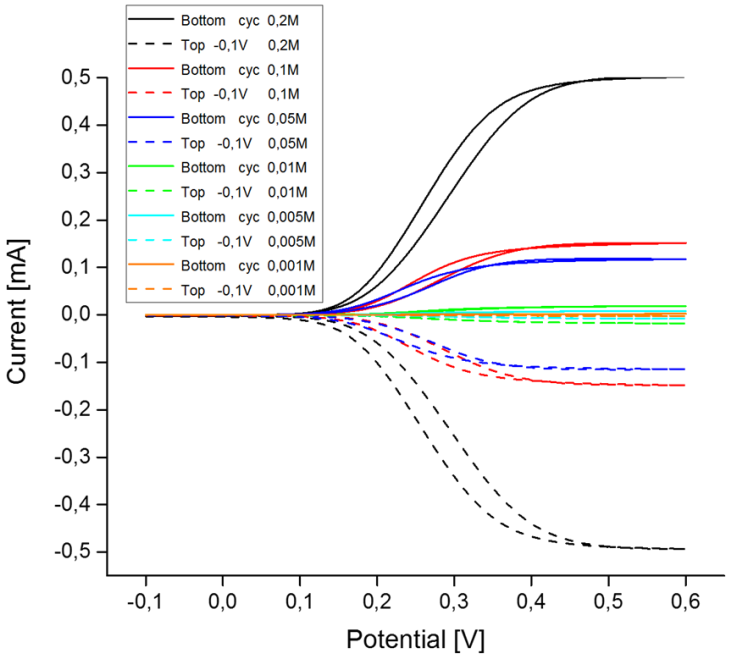

Figure 48: Concentration-dependent redox current in hexacyanoferrate(II): Bottom electrode cycling, oxidation current (solid lines), top electrode at fixed reduction potential -0.1 V (dashed lines), scan rate 0.2 V/s.

With the bottom electrode cycling and the top electrode set at the reduction potential, the cyclic voltammogram shows the same run of the curves as discussed in Figure 43 for all concentrations of hexacyanoferrate(II). The symmetry of the amount of oxidation and reduction current is given again. The evident current-concentration relation is shown, with the lowest current produced for the lowest concentration of reactive molecules. Figure 49 shows an enlargement of the current flow for small concentrations.

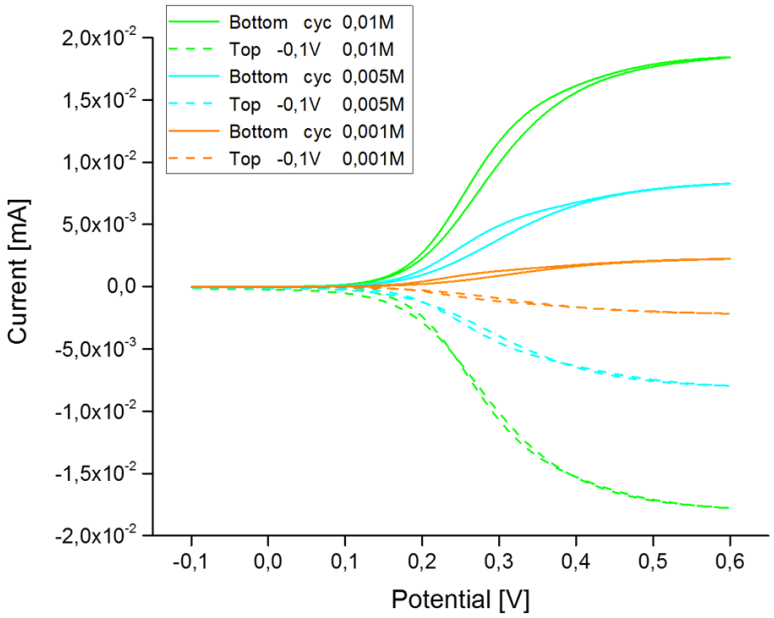

Figure 49: Concentration-dependent redox current in hexacyanoferrate(II) for 0.01 to 0.001 mol/l: Bottom electrode cycling (solid lines), top electrode at fixed reduction potential -0.1 V (dashed lines), scan rate 0.2 V/s.

Concentrations as low as 1 mmol/l hexacyanoferrate(II) could be detected by the redox cycling for the one-electron transfer.

The cyclic voltammogram of Figure 50 shows the concentration dependency as well as the redox symmetry with the top electrode cycling and the bottom electrode set to the reduction potential of -0.1 V. Figure 51 displays the enlargement for the small concentrations.

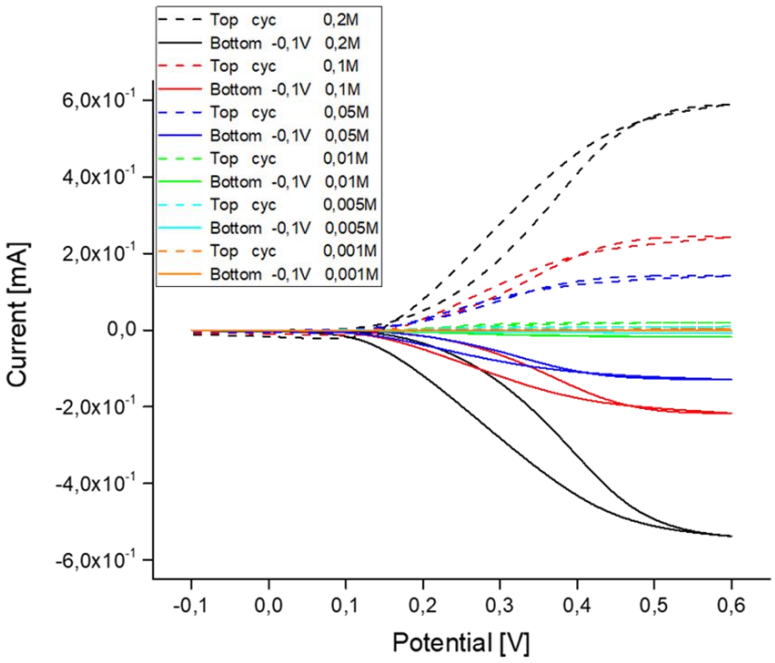

Figure 50: Concentration-dependent redox current in hexacyanoferrate(II): Top electrode cycling, oxidation current (dashed lines), bottom electrode at fixed reduction potential -0.1 V (solid lines), scan rate 0.2 V/s.

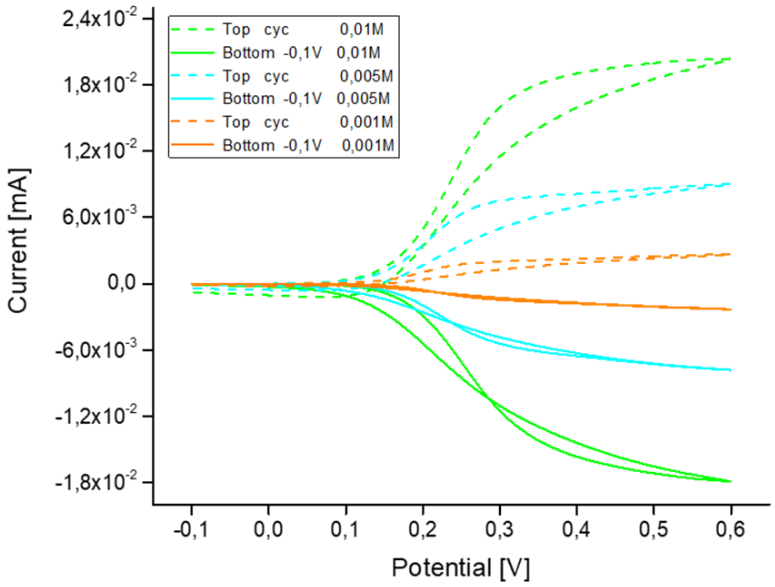

Figure 51: Concentration-dependent redox current in hexacyanoferrate(II) for 0.01 to 0.001 mol/l: Top electrode cycling, oxidation current (dashed lines), bottom electrode at fixed reduction potential -0.1 V (solid lines), scan rate 0.2 V/s.

There does not necessarily need to be a significant loss of reactive molecules to the bulk with the top electrode as the generating electrode, which is the case for the large electrode in this measurement.

The current-concentration relation for the 3 electrode sizes is given in Table 4. Figure 52 and Figure 53 as enlargement display the values. The oxidation current displayed is at the cycling potential of 0.6 V with the bottom electrode cycling and top electrode set to -0.1 V.

Table 4: I-c values for various concentrations at the generator potential 0.6 V for 3 electrode sizes

	I [mA]	0.001 [mol/l]	0.005 [mol/l]	0.01 [mol/l]	0.05 [mol/l]	0.1 [mol/l]	0.2 [mol/l]
Large	Ox	0.00226	0.00830	0.01844	0.11740	0.15170	0.50250
	Red	0.00216	0.00796	0.01777	0.11450	0.14860	0.49350
Medium	Ox	5.527E-4	0.00174	0.00385	0.02567	0.02592	0.08197
	Red	4.916E-4	0.00157	0.00352	0.02430	0.02195	0.07733
Small	Ox	6.744E-5	1.936E-4	4.259E-4	0.00257	0.00349	0.01107
	Red	5.938E-5	1.691E-4	3.819E-4	0.00239	0.00300	0.01041

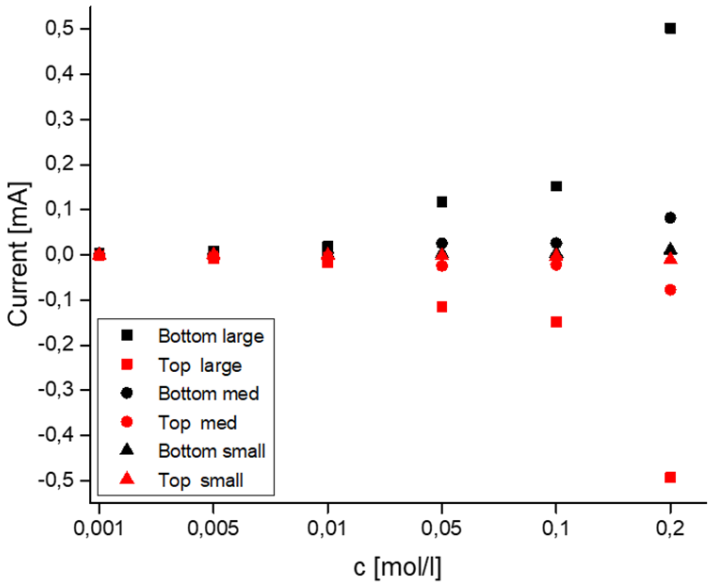

Figure 52: I-c relation for the 3 electrode sizes.

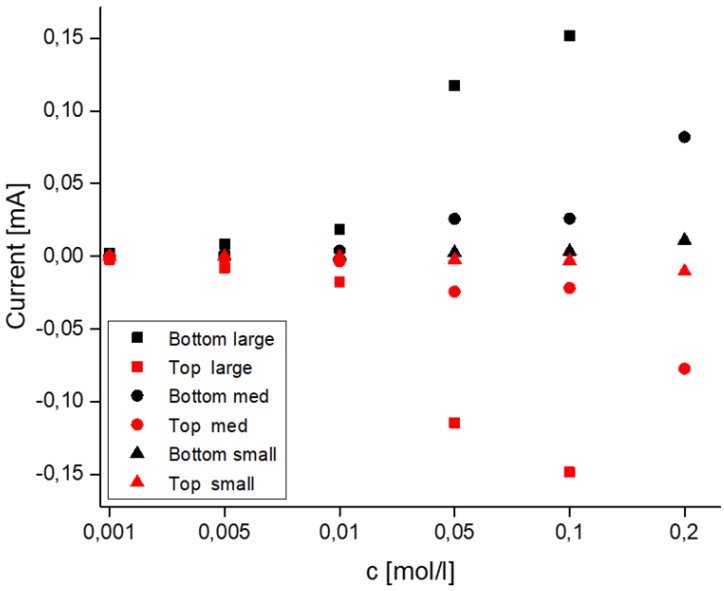

Figure 53: Enlargement of Figure 52, I-c relation.

The current-concentration relation is clearly visible for all 3 electrode sizes. The increase in current with concentrations larger than 0.05 mol/l becomes more prominent and the current values reflect the electrode size. This is due to the increase in pores and thus the increase in reactive surface area for the generating bottom electrode, as given in Table 3.

The sensor clearly reflects the concentration of the redox-active substance in the induced current for all of the 3 electrode sizes. The sensitivity is established up to a concentration of 1 mmol/l for a one-electron transfer redox cycling.

With the Cottrell equation (11) (chapter 2.3.2), the current-time response for spherical microelectrodes can be calculated for a diffusion-driven reaction in sufficiently short times, without time-dependence [51] as

$$I = \frac{nFADc}{r_S} \tag{20}$$

With the diffusion coefficient for ferricyanide $[Fe(CN)_6]^{3-}$, D_{FeIII} $7,17 \cdot 10^{-6}$ cm²/s [100], and dopamine in water, D_{DA} $6 \cdot 10^{-6}$ cm²/s [101], and the surface area of bottom and top electrode in Table 3, the simple time-independent current can be calculated for the various concentrations. Equation 20 is regarding planar spherical electrodes and the radius of a

structured electrode area would be a systematic error, relevant only for comparison to the currents obtained by measurements. Since the alignment error mentioned in chapter 4.2 and the resulting variation in reactive surface of bottom and top electrode is by far the largest divergence, this comparison was forgone here.

4.3.3 Cycling Efficiency

The sensor efficiency, as described in chapter 2.3.2 and equation 16, is a means of evaluating the sensor design by regarding the relation of the oxidation and reduction current, where a perfect cycling efficiency would be Ŋ = 1, with every generated or oxidized molecule collected and reduced again. This is done in this chapter for the 2 electrode settings regarding oxidation and reduction on bottom and top electrode, including the comparison of each electrode size to electrodes of the same size and the varying concentration of reactive molecules. Further, the inter-electrode passivation height of 400 nm is compared to a passivation of 300 nm SiN_x.

The following graphs display the efficiency for all 3 electrode sizes and a 400 nm inter-electrode passivation, with the bottom electrode set to cycling the potential range from -0.1 to 0.6 V and the top electrode collecting and reducing at -0.1 V. All measurements were performed for the same electrode with varying concentrations of potassium hexacyanoferrate(II).

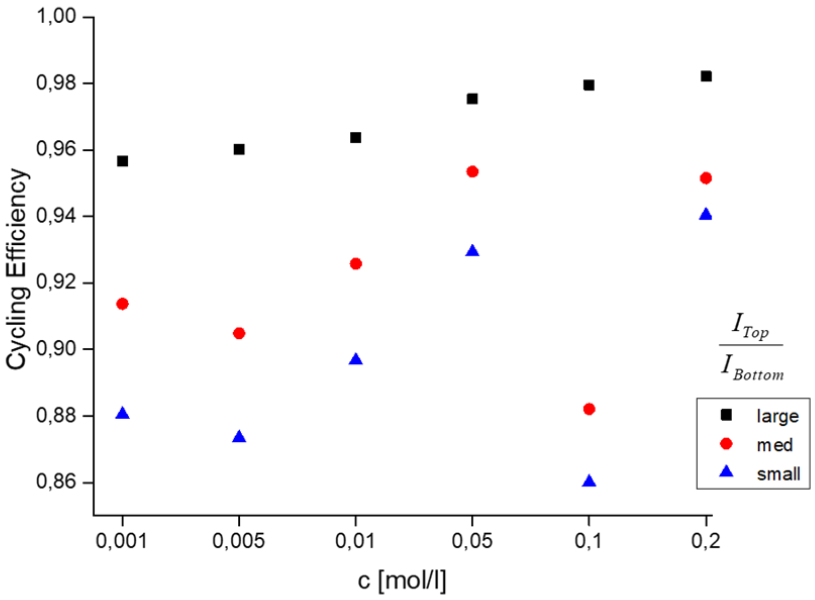

Figure 54: Cycling efficiency of 3 electrode sizes and 400 nm SiN_x passivation

The range of cycling efficiency for all 3 electrode sizes is from 0.86 to 0.98, with the small electrodes showing the lowest efficiency and the large electrode an efficiency very close to 100 %. A slight variation in efficiency for varying concentrations is visible, with steadily increasing efficiency for concentrations larger than 0.05 mol/l, with the exception for 0.1 mol/l on small and medium sized electrodes, which seems to be an inconsistency.

An overall exceedingly good cycling efficiency can be confirmed. The difference in cycling efficiency for the electrode sizes is most likely due to the manufacturing process mentioned in chapter 4.2, where the alignment error and reactive surface area plays an important role for the efficiency and generally large electrodes could be more perfectly aligned than the small electrodes. With an increase in concentration, the probability of reaction at the bottom electrode increases and thus the amount of oxidized molecules to reach the top electrode and take part in the reduction process. This is reflected in the increasing efficiency for increasing concentrations at all 3 electrode sizes.

In the following graphs, the range of efficiency is displayed for each electrode size by comparing the redox cycling efficiency of 3 to 6 electrodes of the same size at varying concentrations of potassium hexacyanoferrate(II). Since different electrodes are compared to each other, the alignment error and resulting reactive surface area have a major effect on the electrode performance, which has to be kept in mind in comparative evaluation. Not all concentration measurements could be obtained for all electrodes compared. The bottom electrodes were set to cycling the potential range from -0.1 to 0.6 V and the top electrode set to the reduction potential of -0.1 V.

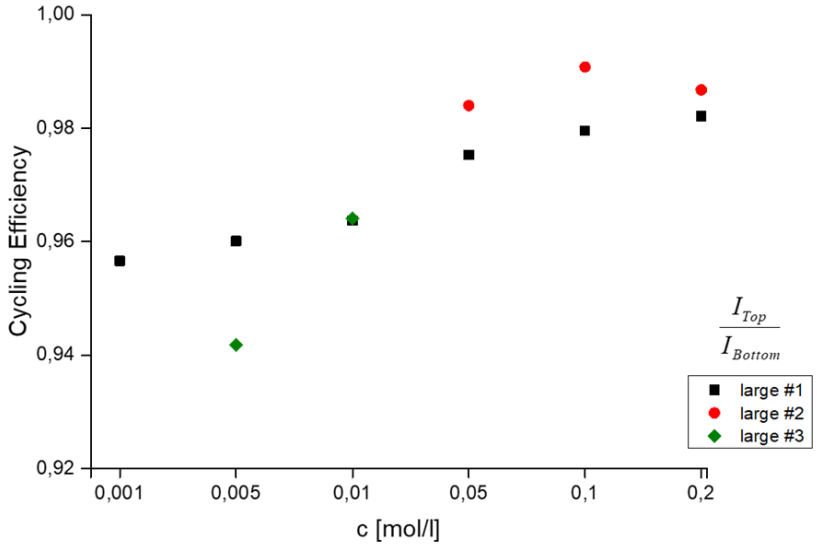

Figure 55: Variance in cycling efficiency on 3 large electrodes.

The 3 large electrodes compared in Figure 55 range from 0.94 to a very good efficiency of 0.99 for concentrations above 0.05 mol/l. Due to the fact that large electrodes were most prone to defects, not all concentration measurements could be obtained for all 3 electrodes compared here.

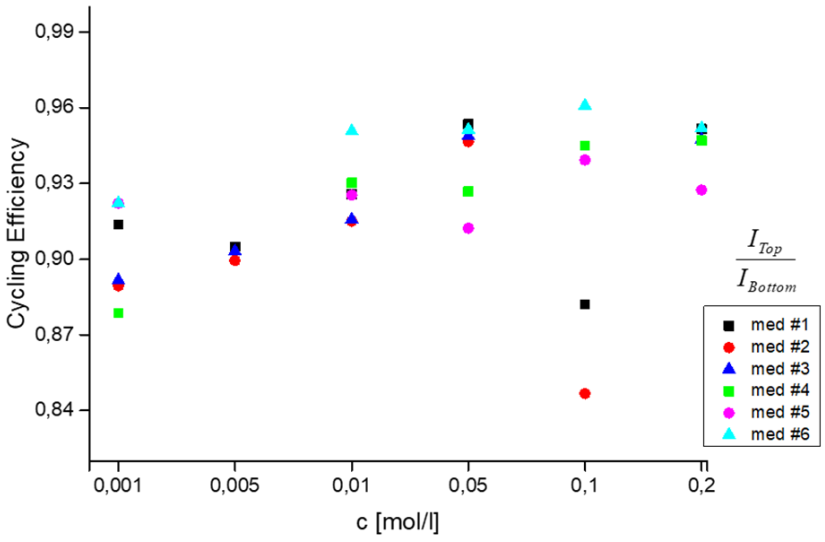

Figure 56: Range in cycling efficiency on 6 medium-sized electrodes.

Figure 56 shows the efficiency range from 0.84 to 0.96 for the 6 medium-sized electrodes compared here. An inconsistency at 0.1 mol/l for the electrodes #1 and #2 is present.

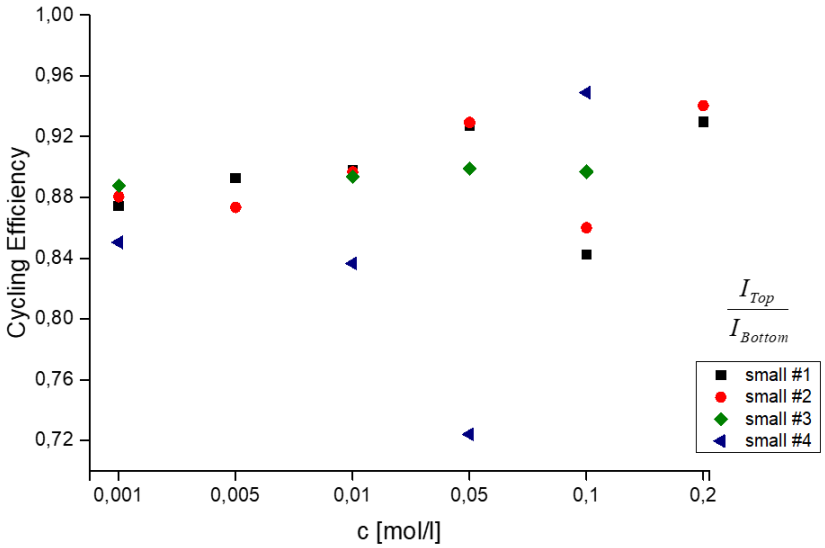

Figure 57: Range in cycling efficiency on 4 small electrodes.

The small electrodes compared in Figure 57 show the widest range of efficiency from 0.72 to 0.95 for the 4 electrodes compared here. This is due to the electrode #4 and a reoccurring inconsistency at 0.1 mol/l for electrode #1 and #2 and would be a range of efficiency from 0.85 to 0.95 for ideal electrodes.

Figure 58 to Figure 60 compare the efficiency for the 3 electrode sizes with regard to the electrode settings, where the generator-collector setting of the bottom and top electrode is switched. In one setting, the reactive molecule is generated at the bottom electrode, in the other at the top electrode. The comparative measurements were performed at the identical electrode.

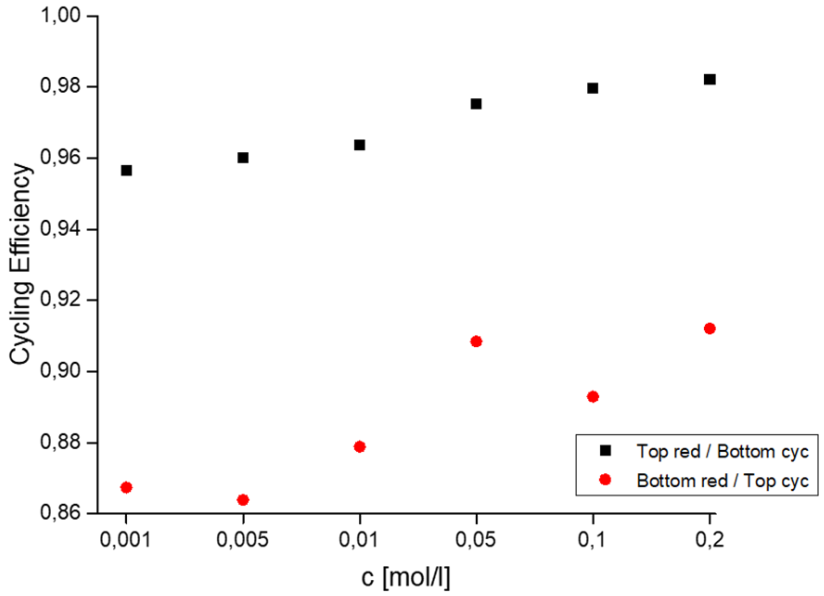

Figure 58: Cycling efficiency of large electrodes for 2 electrode settings. Black: Bottom electrode set to cycling, top electrode set to reduction potential; Red: Top electrode set to cycling, bottom electrode set to reduction potential.

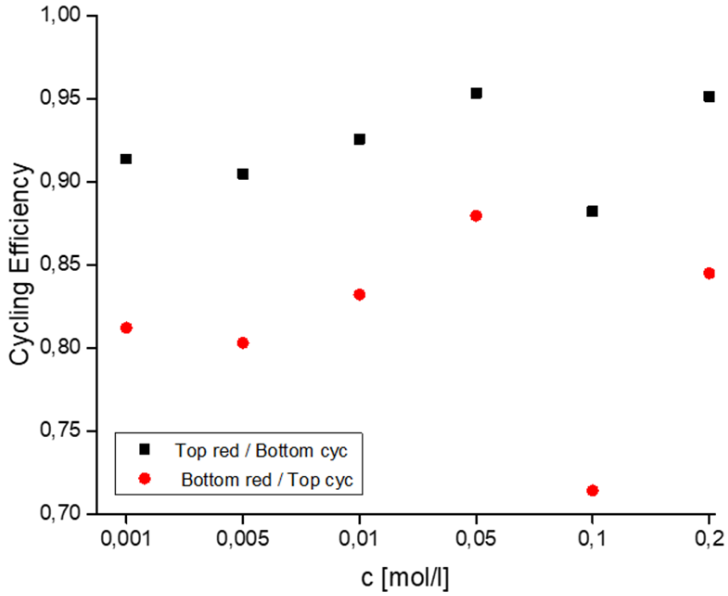

Figure 59: Cycling efficiency of medium-sized electrodes for 2 electrode settings. Black: Bottom electrode set to cycling, top electrode set to reduction potential; Red: Top electrode set to cycling, bottom electrode set to reduction potential.

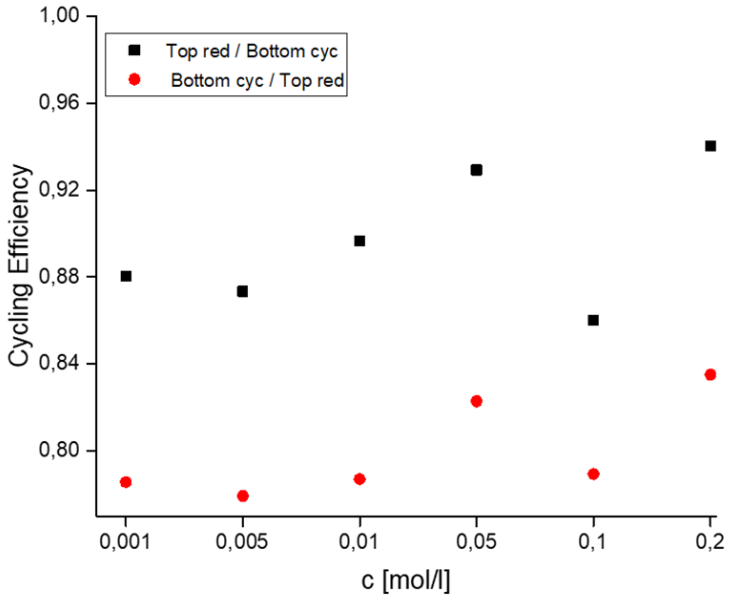

Figure 60: Cycling efficiency of small electrodes for 2 electrode settings. Black: Bottom electrode set to cycling, top electrode set to reduction potential; Red: Top electrode set to cycling, bottom electrode set to reduction potential.

For all 3 electrode sizes, the cycling efficiency is visibly higher when the generating electrode is the bottom electrode. In this setting the generation of the reactive molecule occurs at the bottom electrode, thus confining the oxidized molecule in the pore and increasing the probability of a reaction at the top electrode. This setting guaranties a minimal loss of reactive molecules for the redox reactions whereas the setting of the top electrode as generator and the bottom electrode as collector shows a significant loss of reactants to the bulk solution. An unexplained inconsistency is present in all settings for the cycling efficiency at the concentration of 0.1 mol/l.

As described in chapter 2.3.2, the vertical inter-electrode distance *h* is an important design parameter, since it influences the shuttling time t_S (eq. 14) and thus directly the cycling current I_{cyc} (eq. 15). For the two inter-electrode passivation heights, using equation 14 and

$D_{FeIII} = 7.17 \cdot 10^{-6}$ cm²/s [100], the shuttling times are calculated as

$$t_{S\,300nm} = 6.272 \cdot 10^{-5}\ \text{s} \qquad t_{S\,400nm} = 1.116 \cdot 10^{-4}\ \text{s}$$

and the cycling current for a single ferricyanide molecule with n = 1 and $e_0 = 1.602 \cdot 10^{-19}$ C as

$$I_{cyc\,300nm} = 1.276 \cdot 10^{-15}\ \text{A} \qquad I_{cyc\,400nm} = 7.179 \cdot 10^{-16}\ \text{A}$$

The inter-electrode distance of 300 nm was compared to the 400 nm SiN_x passivation via the cycling efficiency of successfully produced redox-cycling sensors.

Figure 61 to Figure 63 show the cycling efficiency for the various concentrations of hexacyanoferrate(II) for the 3 electrode sizes in measurements, where the bottom electrode was set to cycling the potential range from -0.1 to 0.6 V and the top electrode set to the reduction potential of -0.1 V. Sensor array electrodes with 400 nm inter-electrode distance are displayed in black, 300 nm distance in red.

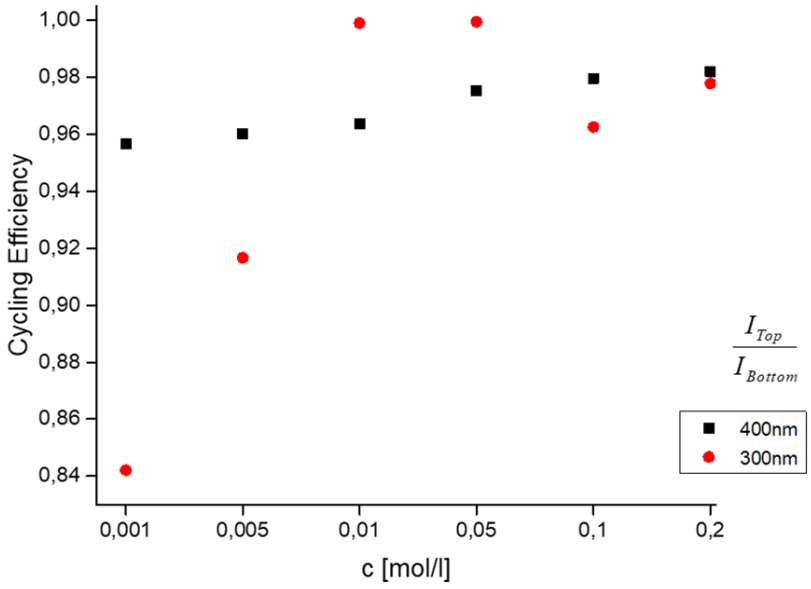

Figure 61: Cycling efficiency of 300 nm vs. 400 nm passivation for large electrodes.

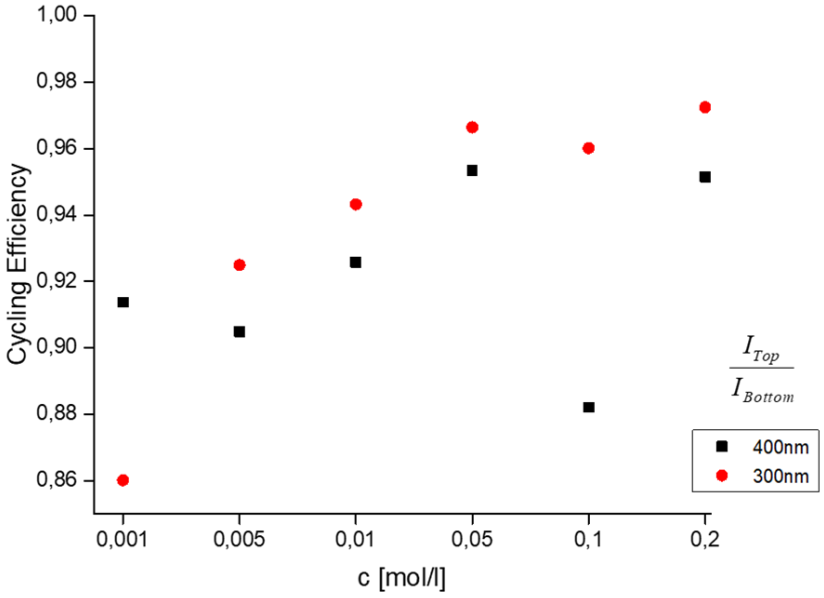

Figure 62: Cycling efficiency of 300 nm vs. 400 nm passivation for medium-sized electrodes.

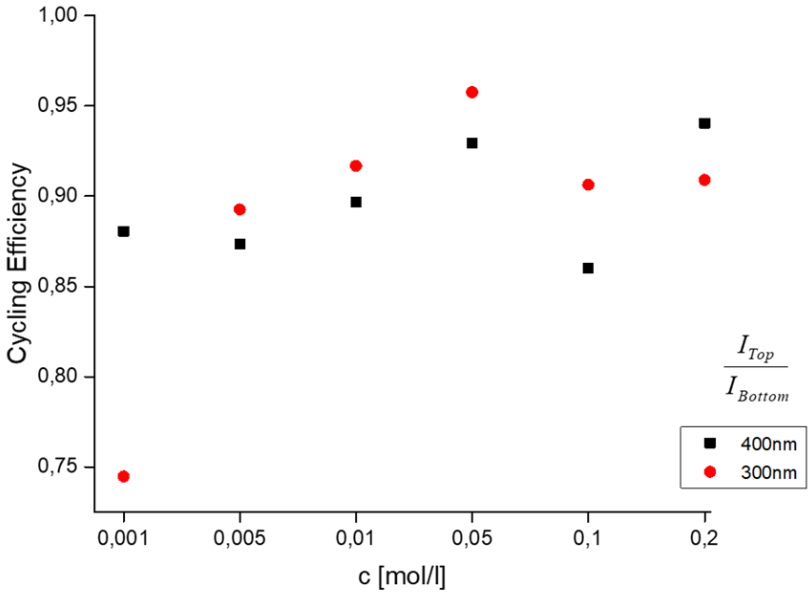

Figure 63: Cycling efficiency of 300 nm vs. 400 nm passivation for small electrodes.

Since different electrodes are compared to each other, the alignment error and resulting reactive surface area have a major effect on the electrode performance, which has to be kept

in mind in comparative evaluation. For the large electrodes in Figure 61, the 300 nm passivation actually reaches the cycling efficiency of 100 % for the concentration of 0.01 and 0.05 mol/l. An unexplained inconsistency is again present for the cycling efficiency at the concentration of 0.1 mol/l. Generally, the highest efficiency in all 3 electrode sizes is reached by the electrodes with 300 nm passivation, although the distribution of the efficiencies at various concentrations does only show a conclusive, overall improvement for the medium-sized electrodes in Figure 62 by a decreased inter-electrode distance. The range of efficiency for both distances is very good and influenced not only by variations in the surface area but also the concentration of reactive molecules and therefore the probability of diffusive transport to the partnering collector electrode.

4.3.4 Fluidic Performance

The fluidic system was chosen to evaluate the sensor regarding the reaction to a change in concentrations and to perform measurements with solutions containing dopamine. Amperometric measurements were performed with the bottom electrode set to the oxidation potential of 0.6 V and the top electrode to the reduction potential of -0.4 V. 0.1 mmol/l dopamine solved in PBS was inserted via inlet No. 1 and 0.01 mol/l PBS via inlet No. 2 (Figure 64). The pressure on channel No. 2 was regulated manually via the MAESFLO control software. Figure 65 shows the current at the bottom electrode displayed in solid lines, the current at the top electrode in dashed lines. The arrows indicate the change of pressure.

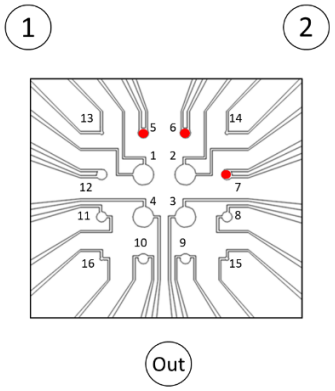

Figure 64: Electrode position relative to fluidic inlets.

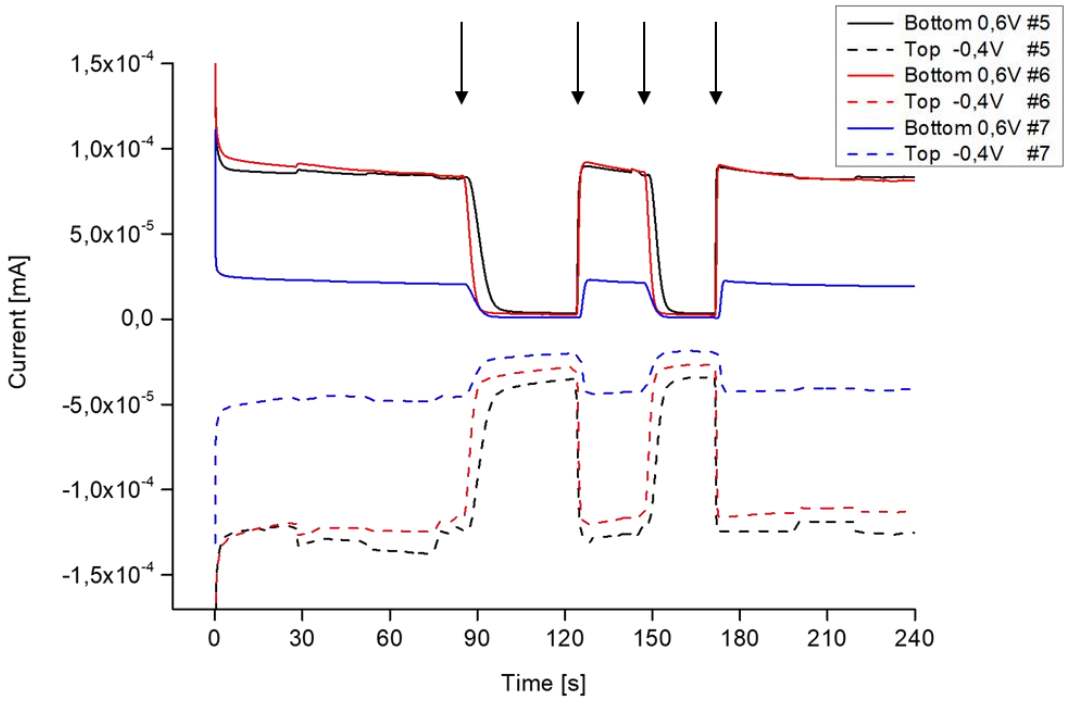

Figure 65: Amperometric measurement of redox currents by 0.1 mmol/l dopamine in PBS with fluid gradient movement via pressure change.

With the initial pressure dominant in channel No. 1, dopamine reaches the electrodes #5 and #6 (Figure 64), where a oxidation and reduction current of similar height is measured. Electrode #7 shows a current of less magnitude, which might be due to the position closest to channel No. 2 or due to the specific characteristics of this electrode.

When the pressure in channel No. 2 is increased, the PBS flow is dominant and pushes the dopamine solution to the side of the array, resulting in an immediate decrease of redox current with only PBS solution present at the electrodes. If reversed, the dopamine solution extends over the electrodes, inducing an immediate redox reaction. The abrupt sloping of the curve in redox current indicates the immediate reaction to a change in concentration for the top as well as the bottom electrode. This means, that the solution flow immediately reaches the bottom electrode in the pore and the oxidized molecules can diffuse to the top electrode to be reduced. A dopamine concentration of 0.1 mmol/l can easily be detected and results in an oxidation current of about $8.5 \cdot 10^{-5}$ mA and a reduction current of $1.3 \cdot 10^{-5}$ mA after 60 seconds for the medium-sized electrodes #5 and #6.

With the flow rate platform FLOWBOARD by *Fluigent GmbH*, the pressure for each channel can be set manually to a fixed value. The following graphs show the amperometric measurement of various dopamine concentrations in PBS (No. 1) vs. pure PBS (No. 2) for each electrode size. The gradient shift across the sensor array is induced by a change in pressure in both of the liquid channels No. 1 and No. 2 at a time interval of 50 s, resulting in 6 consecutive concentration phases, displayed in mbar for No.1 vs No.2 in the graphs. Figure 66 gives the electrode position relative to the liquid inlets, which is to the left side in this measurement and thus more accessible for the solution in channel No. 1. The background current of only PBS solution and pure water is given as well. The bottom electrode is set to the oxidation potential of 0.6 V and displayed in solid lines, the top electrode to the reduction potential of -0.4 V and displayed in dashed lines.

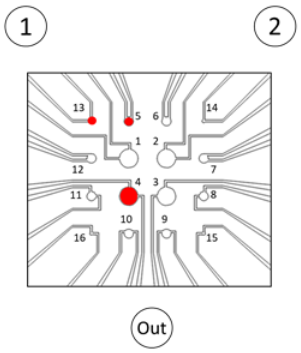

Figure 66: Electrode position relative to fluidic inlets.

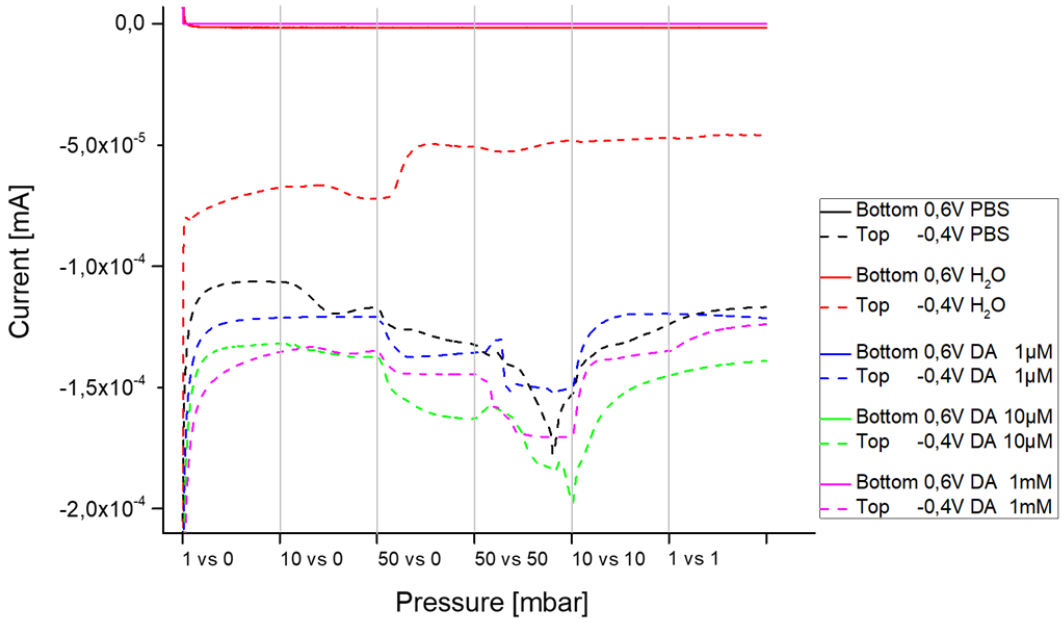

Figure 67: Amperometric measurement of redox currents on a large electrode with various concentrations of dopamine in PBS and background PBS as well as water. Fluid gradient movement via pressure change in channel 1 vs channel 2 in mbar, time interval 50 s.

The bottom electrode in this measurement for the large electrode was defect, showing no current for all concentrations and solutions. On the top electrode a reduction current in response to the dopamine concentration can be measured, with the highest overall value for the highest concentration of 1 mmol/l. Without the bottom electrode, this current is purely amperometric without any cycling effect. In the initial phase, the current is stable with the flow of solution in channel No.1 and increases with increasing pressure for the dopamine solution from 1 to 10 to 50 mbar and reaches the highest value for 50 mbar pressure on channel No.1 and No. 2. The flow of only PBS (black) and pure Water (red) induce a reduction current as well, in the case of PBS even in the range of the current measured by dopamine solution.

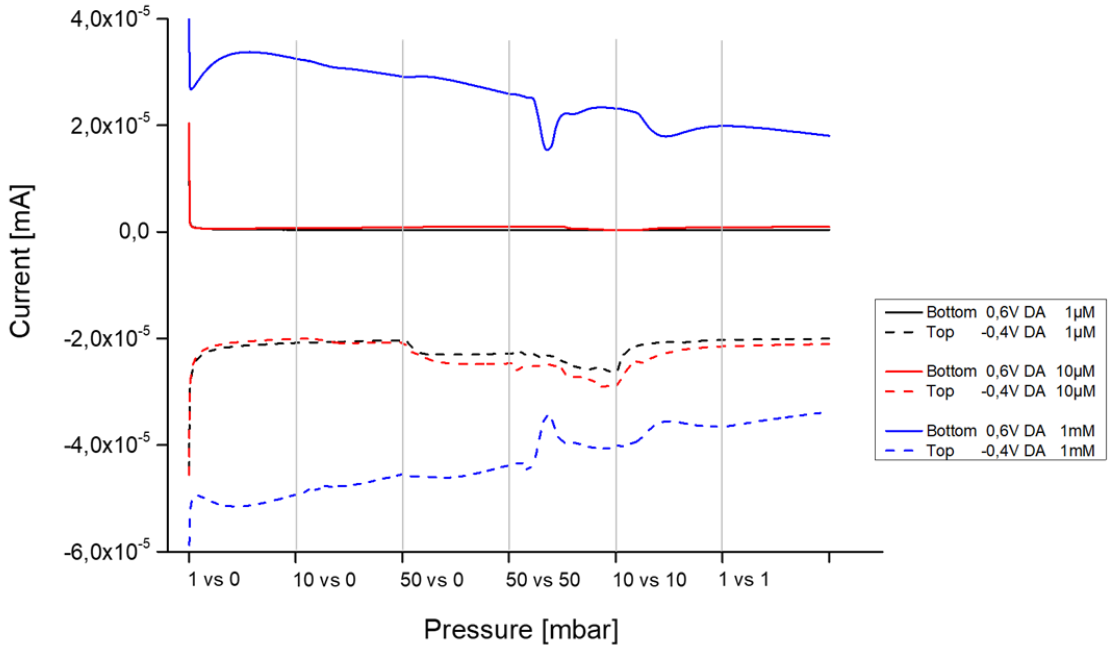

Figure 68: Amperometric measurement of redox currents on a medium-sized electrode with various concentrations of dopamine in PBS and background PBS as well as water. Fluid gradient movement via pressure change in channel 1 vs channel 2 in mbar, time interval 50 s.

In this measurement at a medium-sized electrode, the bottom electrode shows very little oxidation current for concentrations < 1 mmol/l, but a reduction current at the top electrode in relation to the pressure on the channel containing dopamine solution. For 1 mmol/l, the top as well as the bottom electrode show the respective currents of a redox-cycling effect. Increased flow of dopamine solution does not increase the current after an initial peak during the 1st phase at about 25 seconds. A significant decrease in current is induced when the PBS channel No. 2 is switched on in the 4th phase at 160 seconds with a delay of 10 seconds. For this concentration, a general decline in current over time can be observed.

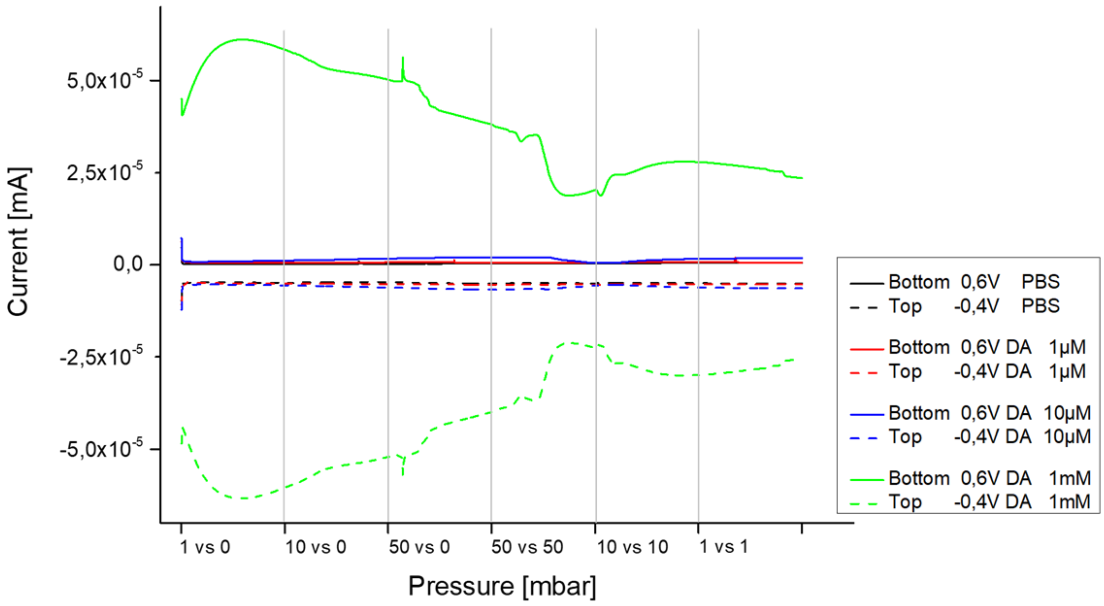

Figure 69: Amperometric measurement of redox currents on a small electrode with various concentrations of dopamine in PBS and background PBS as well as water. Fluid gradient movement via pressure change in channel 1 vs channel 2 in mbar, time interval 50 s.

For the small bottom and top electrode very little redox currents for concentrations < 1 mmol/l are measured. At dopamine concentrations of 1 mmol/l a definite dependence-current can be measured for oxidation at the bottom and reduction at the top electrode (green). After the initial increase with starting flow of dopamine solution, again a steady decline in current is measured over time, with no change due to increased flow and a significant decrease in current by dilution with PBS in the 4th phase, with about 20 seconds delay. Spikes visible are artefacts induced by the change of pressure to the system.

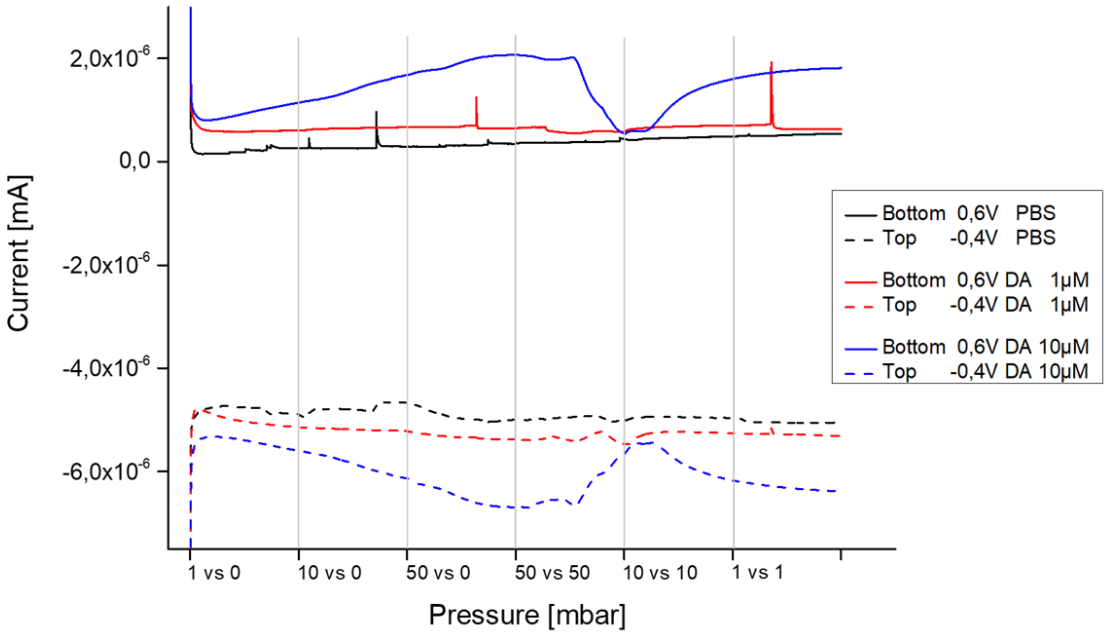

Figure 70: Enlargement of Figure 69, Amperometric measurement of redox currents on a small electrode with various concentrations of dopamine in PBS and background PBS as well as water. Fluid gradient movement via pressure change in channel 1 vs channel 2 in mbar, time interval 50 s.

The enlargement of the redox currents for 1 and 10 µmol/l with the comparison to pure PBS shows an increase in oxidation and reduction current with increased flow for the dopamine concentration of 10 µmol/l. The dopamine-induced redox current is distinctly higher than the background current of PBS. For the concentration of 1 µmol/l, the current shows no response to changes in flow rate and is similar in height to that of PBS. Spikes visible are artefacts, most likely induced by the change of pressure to the system.

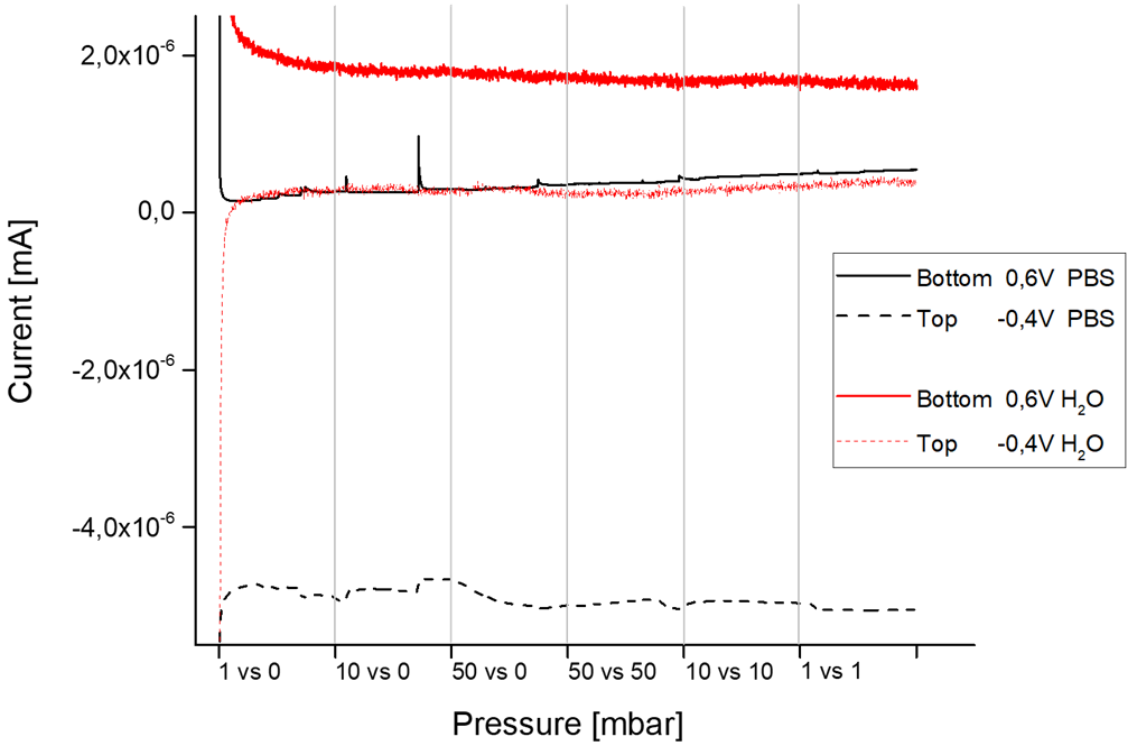

Figure 71: Amperometric measurement of redox currents on a small electrode with background PBS and water. Fluid gradient movement via pressure change in channel 1 vs channel 2 in mbar, time interval 50 s.

Pure PBS and water do not show a redox current at this small electrode, but reflect the potential set to the electrode. The current values are in the range of 10^{-9} A. The negative potential of -0.4 V induces a reaction to changes in the flow rate of the solution in PBS. Spikes visible are artefacts induced by the change of pressure to the system and the background noise is visible at this resolution.

Without both half-reaction currents at the respective electrodes, only the measurements on the medium-sized and the small electrodes for the concentrations of 10 µmol/l and 1 mmol can be interpreted as redox induced dependence-current (Figure 68 to Figure 70). These measurements reflect the dependence on dopamine concentration and deliverance of reactive molecules by hydrodynamic flux.

The establishing of a stable gradient of solutions from the two inlets could not be verified by measurements utilizing dyed solutions. In general, the PDMS fluidic chamber induced eddies and wall effects and a laminar flow cannot be presumed. Changes in pressure on one channel disrupt the liquid flow in the chamber in diverse ways. Additionally, the utilized hardware by *Fluigent GmbH* provides an open-loop system. Initially set pressure does not prevent backflow in the channel of lower pressure, resulting in the contamination of solution and a diverted flow in the chamber. Therefore, parameters had to be watched closely and any backflow had to be prevented by synchronizing the pressures to a working value.

Since the top electrode naturally is more exposed to the liquid flow than the bottom electrode in the pore, the measurement of redox induced dependence-current on both electrodes with the oxidized molecules from the bottom electrode reacting at the top electrode is all the more impressive. The pore design also proves to be successful with regard to the access of analyte molecule to the bottom electrode, as well as diffusion in the pore and flushing out.

4.4 In-vitro measurements

In order to simulate the physiological dopamine detection, PC12 cells were cultured on the developed sensor array, to be the source of dopamine for amperometric detection. Potassium chloride as well as dopamine in solution was used to initiate cellular dopamine release. The results shown in this chapter were obtained in part by Louisa Bühler during the direct supervision of her Bachelor thesis [102].

4.4.1 Cell culture on sensor array

The cultivation of the PC12 cells on the sensor proofed to be simple and successful with the protocol described in chapter 3.2.4 and 3.2.5. The amount of cells applied to the sensor surface was checked by microscopic imaging, since no cell count was established and dilution by volume was used to dilute the cell solution. The correct amount of cells ensured a proper attachment for several days, without cluster formation or desorption due to cell-cell attachments. Figure 72 shows optical images of a cell layer of PC12 cells on various electrodes after a measurement was undergone.

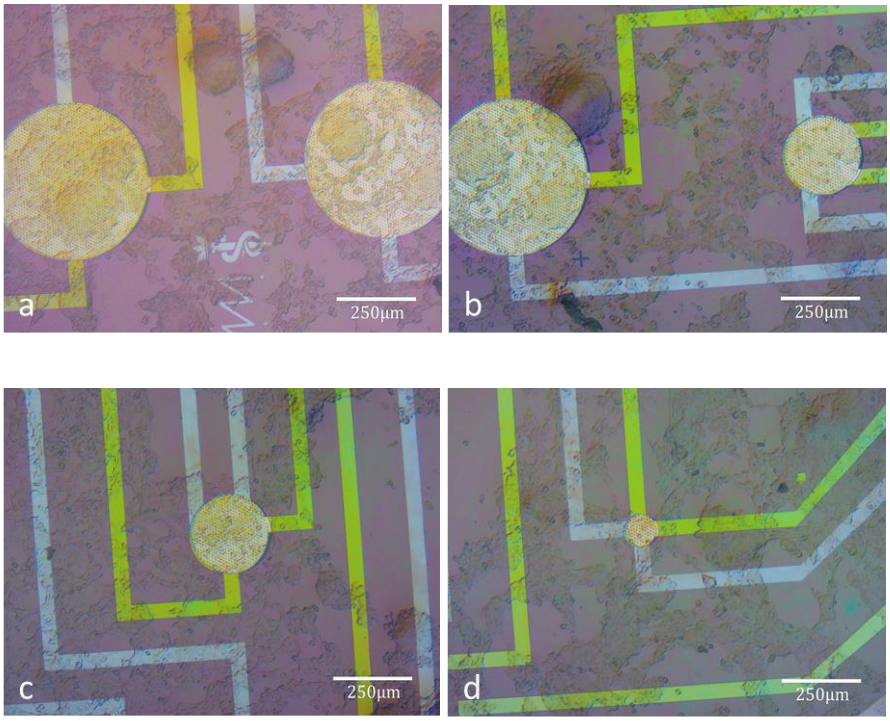

Figure 72: Optical images of a PC12 cell layer on top electrodes of various sizes, a) and b) large electrodes, c) medium-sized electrode, d) small electrode. Images by Louisa Bühler.

A confluent cell layer was mostly not established over the full sensor array, since the PC12 cells tended to attach easily to each other after proliferation. Measurements were undergone only on electrodes initially covered with cells, as shown in Figure 72. Generally, cells cultivated on the sensor arrays could be used for days, when flushing and the change of medium was done carefully. The measurements induced some stress on the cells, mainly due to the change in temperature and pH of medium, which resulted in cell rounding or detachment.

4.4.2 Background Measurements

In order to investigate the effect of solution and stimulation substance, preliminary measurements with DMEM and PBS were done to exclude a potential influence on the redox current. KCl and dopamine in solution were also tested on the sensor. The following graphs display amperometric measurements in cultivation medium (black) and PBS (red), with the bottom electrode set to the reduction potential of - 0.4 V (solid lines) and the top electrode to the oxidation potential of 0.7 V (dashed lines). This setting was chosen for the measurements on cell culture with regard to the electrode position, so that the maximum dopamine oxidation could be measured at the more exposed top electrode.

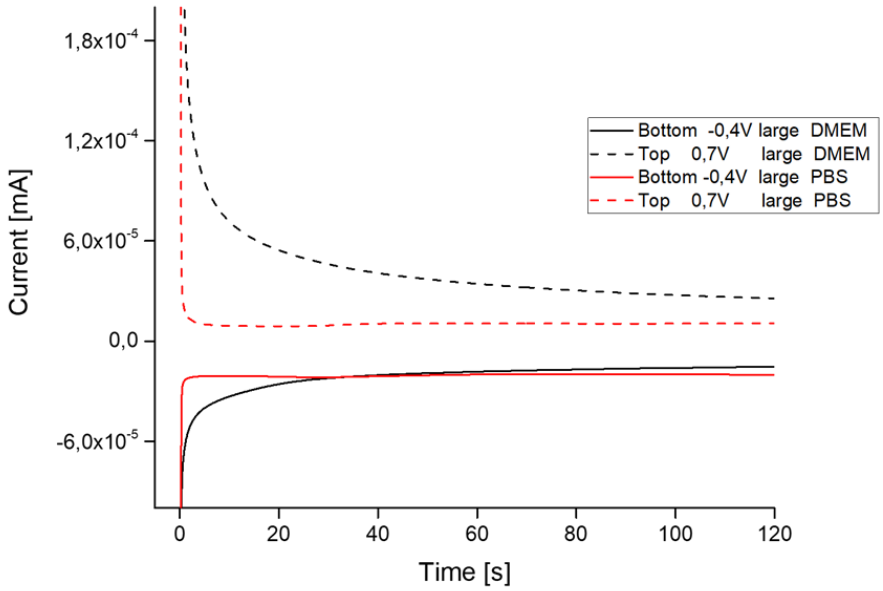

Figure 73: Amperometric measurement in DMEM and 0.01mol/l PBS solution on a large electrode: Bottom electrode set to reduction potential -0.4 V (solid lines), top electrode set to oxidation potential 0.7 V (dashed lines).

Figure 73 shows the current induced on a large electrode by DMEM and pure PBS without redox active substances present. The current in PBS solution is smaller than in DMEM due to the increased amount of solvated ions contained in the medium. For both potentials the current ranges within +/- 0.06 µA. The current gradient shows the initial establishment of an electrical double-layer and its extension into the bulk, resulting in a depletion of charged ions in the vicinity of the electrodes and thus in a steady decline of the current. This is less pronounced for the PBS due to the smaller amount of ions.

The effect of potassium chloride was investigated by applying 50 µl of 1 mol/l KCl to 450 µl DMEM after 60 seconds, resulting in a final concentration of 100 mmol/l KCl, and is displayed in Figure 74 for a medium-sized (black) and a small electrode (red).

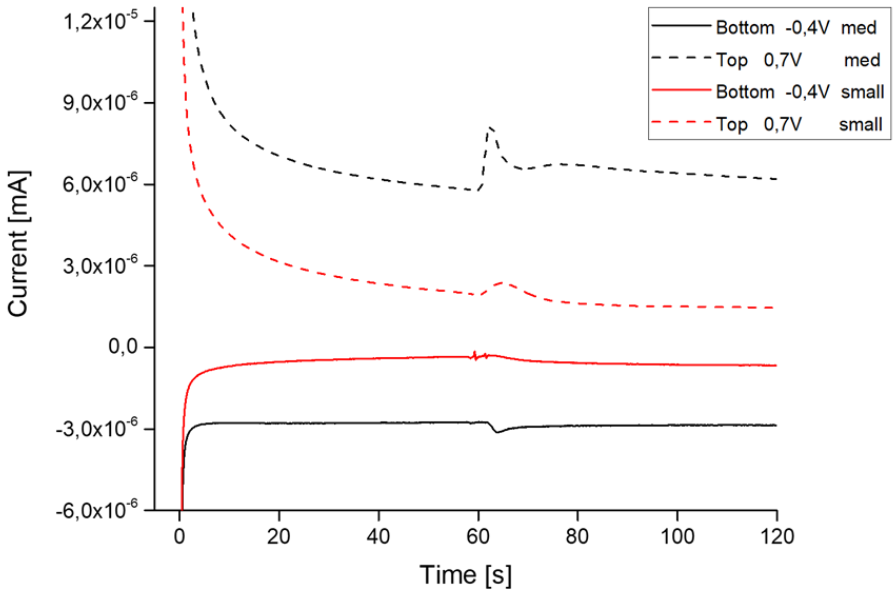

Figure 74: Amperometric measurement of 100 mmol/l KCl in DMEM on a medium-sized and a small electrode: Bottom electrode set to reduction potential -0.4 V (solid lines), top electrode set to oxidation potential 0.7 V (dashed lines).

Since KCl dissociates to positively charged potassium and negatively charged chloride ions, the visible increase of current is expected to be instant and temporary, since there are no redox-active substances present. The top electrode is more exposed to ions pipetted into the liquid on the sensor array than the bottom electrode and has a larger surface area (see Table 3 chapter 4.2) , which results in a more prominent effect on the top electrodes for both sizes.

The effect of dopamine added to the measurement solution was investigated similar to the KCl effect, by pipetting 5 µl of 1 mmol/l dopamine in PBS to 450 µl of DMEM after 60 seconds, resulting in a final dopamine concentration of 100 µmol/l. Figure 75 shows the effect on a medium-sized, Figure 76 on a small electrode.

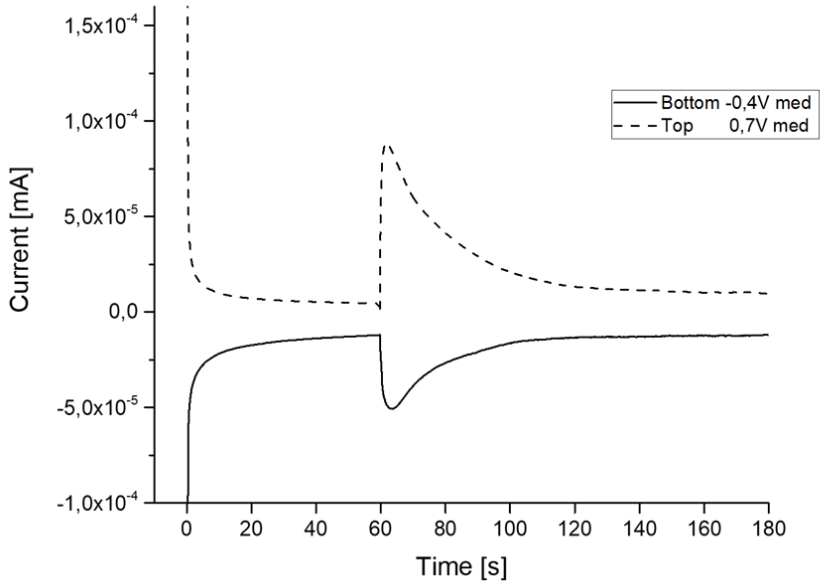

Figure 75: Amperometric measurement of 100 µmol/l dopamine in DMEM on a medium-sized electrode: Bottom electrode set to reduction potential -0.4 V (solid lines), top electrode set to oxidation potential 0.7 V (dashed lines).

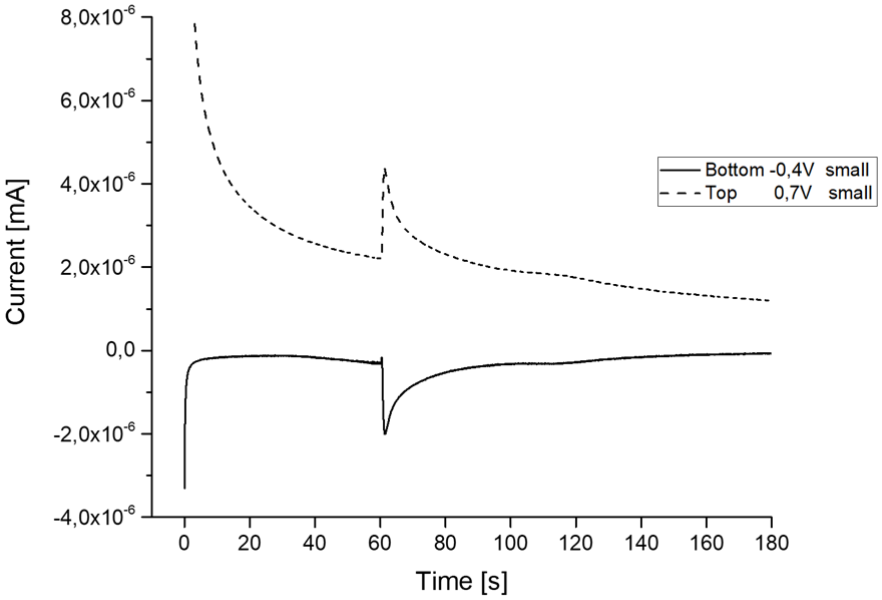

Figure 76: Amperometric measurement of 100 µmol/l dopamine in DMEM on a small electrode: Bottom electrode set to reduction potential -0.4 V (solid lines), top electrode set to oxidation potential 0.7 V (dashed lines).

Both electrodes show clearly the effect of injection of a redox-active component, in case of the medium-sized electrode, with an area-dependent unequal amount of current. The oxidation current at the top electrode is larger than the reductive current at the bottom electrode due to the exposed position and larger surface area. When the difference in electrode size is not as distinct, the currents show an equal amount, as for the small electrode in Figure 76. The injection of dopamine generally induces a sharp spike, followed by a fast decline in current, which continues the initial declining slope. Since the dopamine is injected into the culture well on the sensor array with a forceful flash by a pipette, it is likely that a variation in concentration is generated on the electrode array with a loss of redox-active molecules due to the kinetic energy of the flush. Dopamine to be oxidized at the top electrode would thus not be present for long and hence not be reduced at the bottom electrode, which would result in the temporary increase of current, similar to that of KCl in Figure 74.

4.4.3 Stimulation-induced Dopamine Release

Successfully cultured PC12 cells on the sensor array were induced to release dopamine by injection of KCl. The optimal concentration of KCl for the stimulation of PC12 cells was described to be between 75 and 120 mmol/l ([44], [103], [104]). Therefore, 60 seconds after the start of the measurement, 72 µl of 1 mol/l KCl was pipetted to the culture containing well, holding 528 µl of buffered DMEM, resulting in a final concentration of 120 mmol/l KCl. The resulting dopamine release can be seen in Figure 77 for a medium-sized (black) and a small electrode (red), were the bottom electrode is set to -0.4 V (solid lines) and the top electrode to 0.7 V (dashed lines).

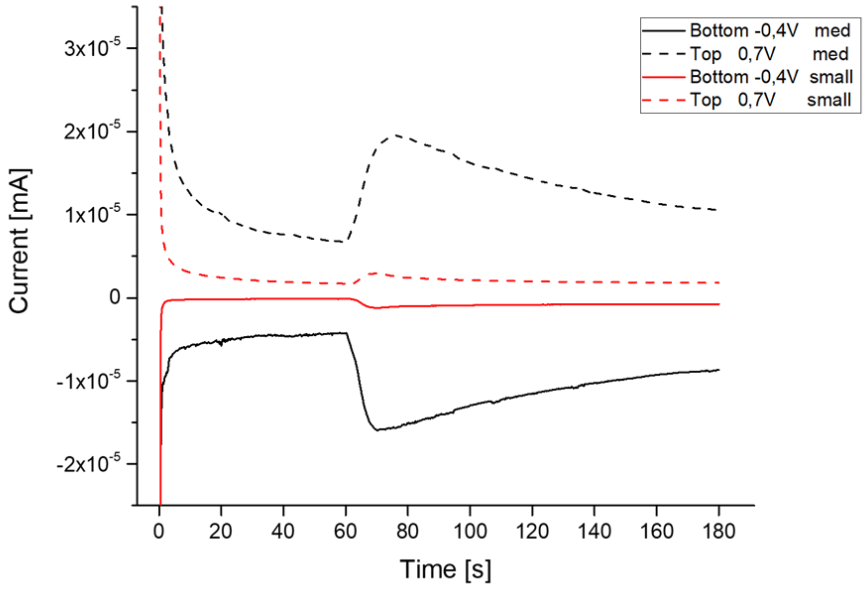

Figure 77: Amperometric measurement of KCl induced dopamine release of PC12 cells on medium-sized electrode (black) and small electrode (red). Bottom electrodes set to reduction potential -0.4 V, top electrode set to oxidation potential 0.7 V.

In the first 60 seconds prior to the stimulation, the current steadily declines due to the development of a depletion zone of ions. After the stimulation with KCl at 60 seconds, an equivalent increase in current at both, bottom and top electrode, is measured, which clearly indicates a redox current. Compared to the background measurement of only KCl in Figure 74 and the background measurement of dopamine in DMEM in Figure 75 and Figure 76, the current increase is not as instantaneous, the peak is reached after 10 seconds instead of immediately and the peak itself is not as sharp. The following gentle decline in current is not regaining the initial value within 120 seconds. This indicates a dopamine release by the PC12 cells and an equal number of oxidation and reduction reactions. The surface-area dependency of the current for the different sizes of electrode surfaces is clearly visible and in this kind of measurement additionally influenced by the amount of cells located at or near an electrode and the local concentration and flux of KCl and thus released dopamine. Although physiological dopamine release can be extremely fast, in culture conditions the effects of the diffusion of molecules and the flux of solution must be considered. Since the surface area of the sensor was treated by PLL, a capacitive layer between top electrode metal and adhered cells can be assumed, which could act as a barrier for the diffusion of molecules, that would

delay the redox reactions but also prevent the loss of redox active molecules to the bulk and result in a prolonged cycling.

Since there was no redox active substance present before the stimulation and after stimulation a redox current is measured, the successful dopamine release and detection by the sensor array can be verified in this measurement and multiple stimulation was tested additionally. Therefore, immediately before the measurement the DMEM was removed and exchanged for preheated PBS solution in order to reduce the background current. The stimulation was initiated by injecting 50 µl of 1 mol/l KCl to 450 µl PBS on PC12 cells, resulting in a final concentration of 100 mmol/l KCl.

The following graphs show a repeated stimulation by KCl without intermittent removal of the medium and with removal. Figure 78 displays an amperometric measurement with PC12 cells and KCl induced dopamine release after 60 seconds and again after 300 seconds for a medium-sized electrode were the bottom electrode is set to -0.4 V (solid lines) and the top electrode to 0.7 V (dashed lines).

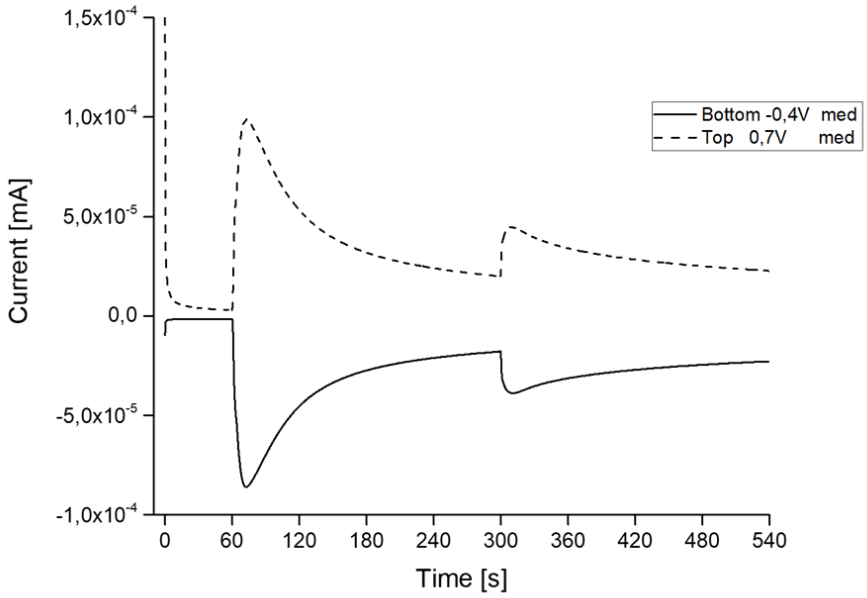

Figure 78: Amperometric measurement of repeated KCl induced dopamine release of PC12 cells on medium-sized electrode. Bottom electrodes set to reduction potential -0.4 V, top electrode set to oxidation potential 0.7 V.

The first stimulation after 60 seconds results in a massive increase of current on both, bottom and top electrode equally, and the gentle decline in current described above for Figure 77. 4 minutes after the first stimulation, the second stimulation with KCl again induces an increase in current for both electrodes, indicating a second dopamine release from the PC12 cells and a resulting redox reaction. The second release induces a smaller redox current, indicating a smaller amount of released dopamine, which is likely founded in the prior release and depleted dopamine reserve within the cells.

Figure 79 and Figure 80 show the same measurement with removal of the dopamine containing PBS solution after the first stimulation and the second stimulation in fresh solution for a large and a small electrode. Preheated, fresh PBS was applied as gently and quickly as possible, with the second measurement starting immediately afterwards. For the second stimulation, the time scale is not significant.

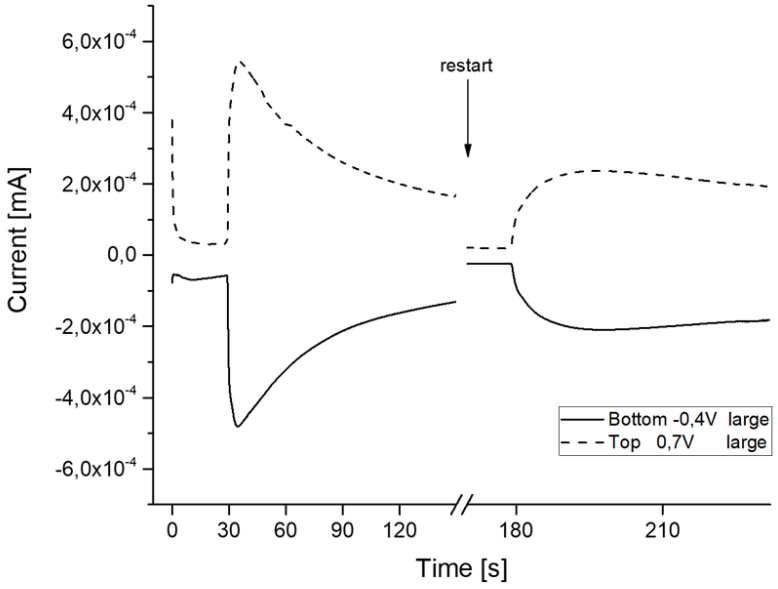

Figure 79: Amperometric measurement of repeated KCl induced dopamine release of PC12 cells on a large electrode with exchange of solution. Bottom electrodes set to reduction potential -0.4 V, top electrode set to oxidation potential 0.7 V.

For the large electrode in Figure 79, the first stimulation is equal to the measurement described for Figure 78. The initial value of steady-state current is regained after exchanging the PBS solution and a second stimulation induces another dopamine release and resulting

redox currents. The shape of the current profile suggests an instant yet slowly increasing dopamine concentration at the electrodes, reflected in the slope of the peak, which reaches its maximum 20 seconds after the stimulation and might be the physiological response to a repeated intense stimulation. The current value is only half of that of the first stimulation, suggesting the depletion of dopamine reserves in the cells.

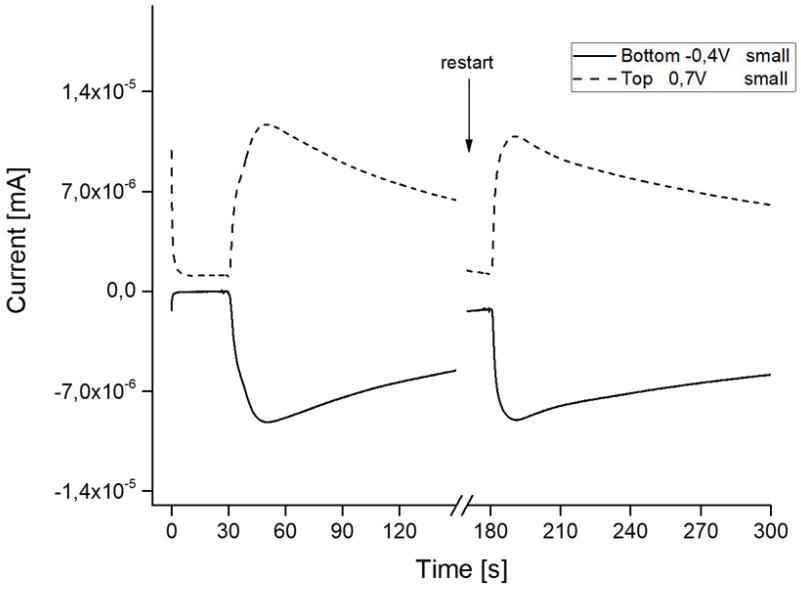

Figure 80: Amperometric measurement of repeated KCl induced dopamine release of PC12 cells on a small electrode with exchange of solution. Bottom electrodes set to reduction potential -0.4 V, top electrode set to oxidation potential 0.7 V.

For the small electrode in Figure 80 both stimulations are similar in shape, reaction time and current value, with the steady-state current prior to the second stimulation slightly higher than the initial. Here, an identical current value and thus amount of dopamine reacting at the electrode within the same timespan can be induced by the second stimulation. Since this measurement shows the effect for a small electrode, a detection limit could be given due to limited size and a large amount of cells on the electrode area. If the electrode is covered completely with cells, the released dopamine relative to the surface area could result in the second, equally large current measurement.

Since dopaminergic cells are capable of reuptake of dopamine, the time interval of 4 minutes between stimulation for the measurement without the change of solution (Figure 78) should be sufficient to reincorporate dopamine and release it again at a second stimulation. The measurements with a change of solution and removal of initially released dopamine suggest that the amount of KCl used to induce dopamine release via membrane polarization does not deplete the cells of dopamine and allows a second release after stimulation.

Even with the most careful removal of culture solution many cells detach from the surface and are lost for a second measurement. Together with a reduced amount of dopamine readily available for the cell, this can result in a decreased dopamine release during the second stimulation. As mentioned before, the amount of cells located at or near an electrode and the local concentration and flux of KCl have a major impact in these measurements and can allow an identical repetition of performance like displayed in Figure 80, with no loss of adhered cells and not fully depleted cells after the first dopamine release.

4.4.4 L-Dopa augmented release by KCl and Dopamine stimulation

In order to show the uptake effect of dopaminergic cells treated with L-Dopa, amperometric measurements were done on PC12 cells incubated with L-Dopa, as described in chapter 3.2.4. For the stimulation after 60 seconds, 50 µl of 1 mol/l KCl was pipetted to 450 µl DMEM, resulting in a final concentration of 100 mmol/l KCl. Augmented and physiological release measurements were not recorded on the identical electrode in the same culture.

Figure 81 and Figure 82 show the stimulation result of loaded PC12 cells (red) in comparison to a regular release (black) for a medium-sized and a small electrode. The bottom electrode was set to the reduction potential of -0.4 V (solid lines) and the top electrode to the oxidation potential of 0.7 V (dashed lines).

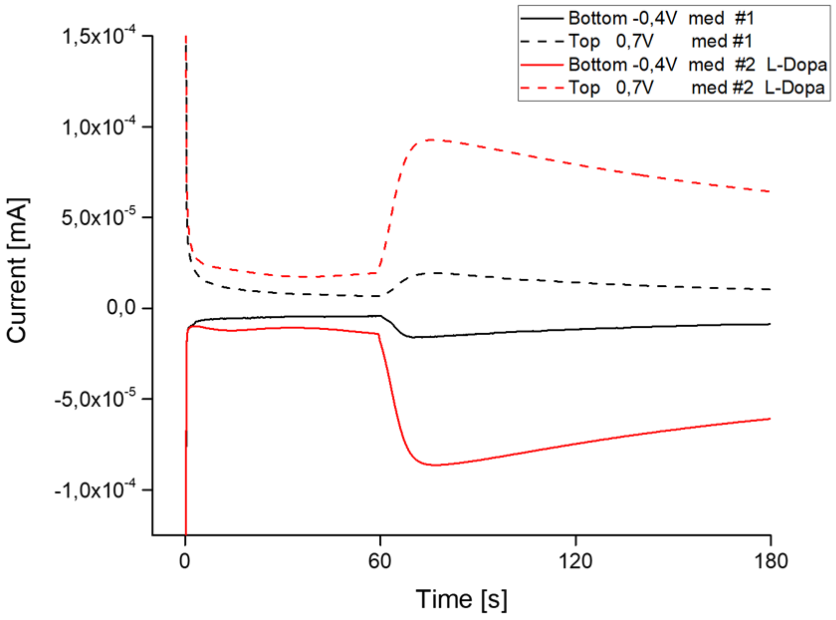

Figure 81: Amperometric measurement of L-Dopa treated (red) vs. physiological PC12 cells (black), stimulated by KCl on a medium-sized electrode. Bottom electrodes set to reduction potential -0.4 V, top electrode set to oxidation potential 0.7 V.

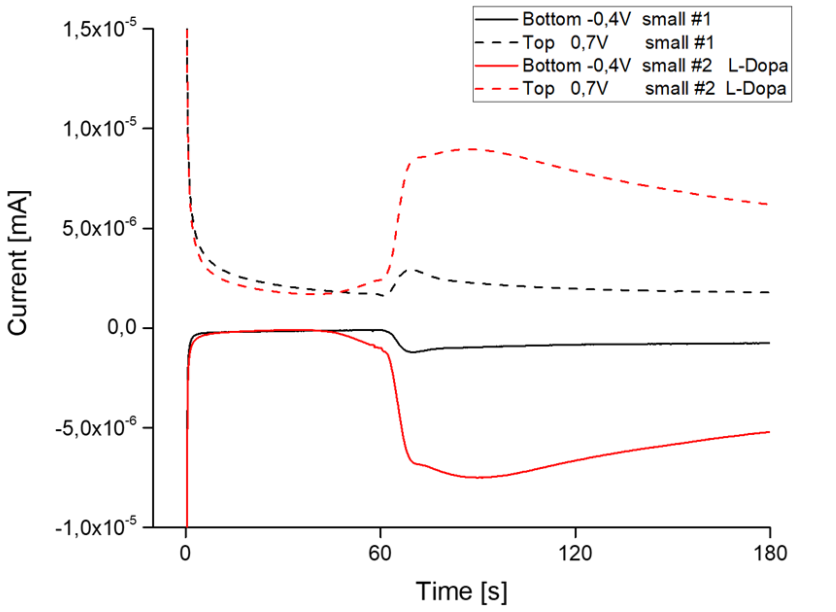

Figure 82: Amperometric measurement of L-Dopa treated (red) vs. physiological PC12 cells (black), stimulated by KCl on a small electrode. Bottom electrodes set to reduction potential -0.4 V, top electrode set to oxidation potential 0.7 V.

For both electrode sizes a significant increase of current can be detected after stimulation with KCl for the culture with L-Dopa treatment. Clearly more dopamine is released, resulting in a much higher redox current than a regular release provides. Even though a quantitative comparison between regular and augmented dopamine release is not possible due to variations in electrode performance, culture density and stimulation effects, an incubation with 100 µmol/l L-Dopa for 2 hours shows the uptake of the precursor and release in the resulting concentration of redox active dopamine at the sensor electrodes.

Since extracellular dopamine induces a dopamine release on dopaminergic cells, a stimulation of L-Dopa treated PC12 cells by dopamine itself was tested, in order to compare the dopamine effect from extracellular presence and cellular release at the sensor array.

Figure 83 and Figure 84 show the amperometric measurements with stimulation by 100 µmol/l dopamine in PBS with (red) and without (black) PC12 cells cultivated on the sensor array for a medium-sized and a small electrode. Both measurements were done at the identical electrodes. After 60 seconds, 50 µl of 1 mmol/l dopamine in PBS was pipetted to 450 µl of DMEM. The bottom electrode was set to the reduction potential of -0.4 V (solid lines) and the top electrode to the oxidation potential of 0.7 V (dashed lines).

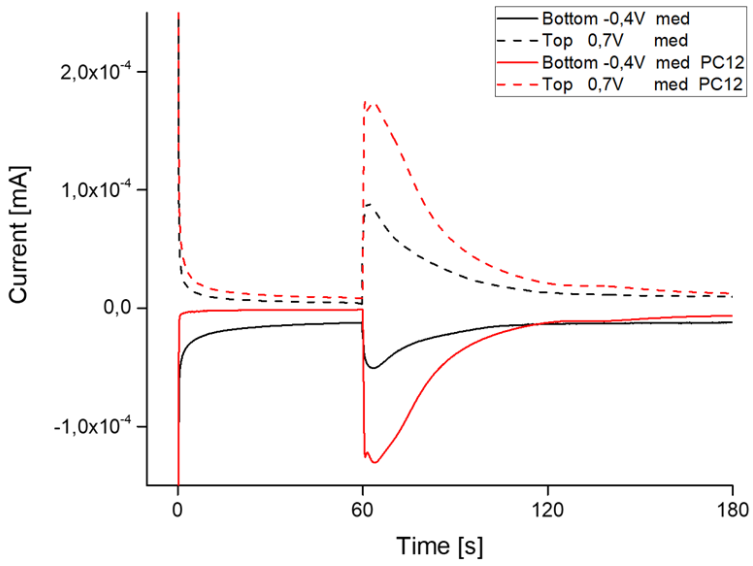

Figure 83: Amperometric measurement of dopamine-induced dopamine release on L-Dopa treated PC12 cells (red) vs. dopamine background (black) on a medium-sized electrode. Bottom electrodes set to reduction potential -0.4 V, top electrode set to oxidation potential 0.7 V.

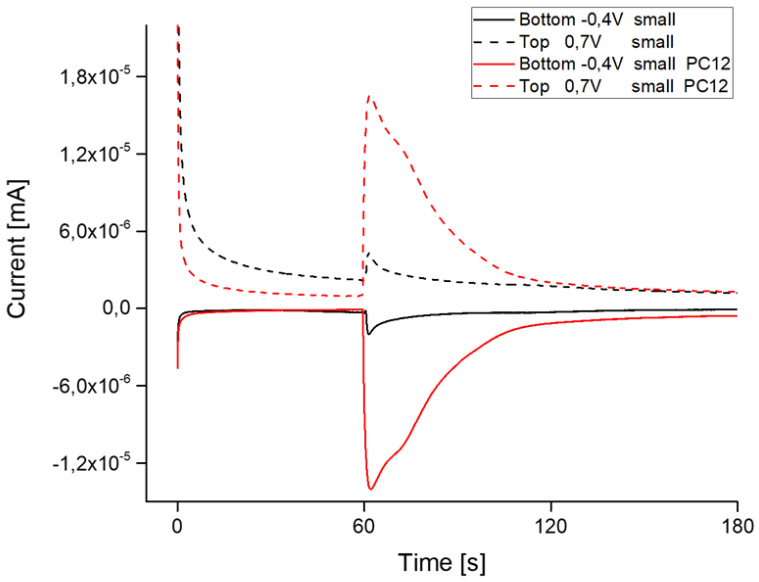

Figure 84: Amperometric measurement of dopamine-induced dopamine release on L-Dopa treated PC12 cells (red) vs. dopamine background (black) on a medium-sized electrode. Bottom electrodes set to reduction potential -0.4 V, top electrode set to oxidation potential 0.7 V.

The massive increase of current immediately after injection of dopamine to L-Dopa augmented PC12 cells, compared to the current of the 100 µmol/l dopamine in PBS, clearly indicates the release of additional dopamine provided by the PC12 cells. For the medium-sized electrode in Figure 83, the peak current is twice as high, for the small electrode in Figure 84 almost 6 times as high.

The stimulation of PC12 cells with dopamine results in a very different current profile than that with KCl, shown in Figure 81 and Figure 82, where a gentle decline of redox current follows the current peak. With dopamine, the current decreases fast and almost reaches the steady-state value from before the stimulation within 60 seconds. Both kinds of stimulation were measured in DMEM, where the buffering effect is the same, which excludes the buffering of oxidized or reduced dopamine molecules in the medium. Since KCl-induced stimulation triggers a membrane depolarization, whereas extracellular dopamine induces further dopamine release via receptor binding, the release-time and reuptake process might be influenced differently in both cases for PC12 cells. The developed sensor array allows the successful detection of this distinction.

4.5 Sensor Modifications

The developed sensor array was modified in an attempt to increase the sensitivity and to take a first step towards flexibility for future developments of an implantable sensor system. This was done in two separate process developments by nanosphere lithography and with a flexible polymer substrate, with the results described in this chapter. The NSL was used to produce pores of reduced diameters in the nanometer range, to increase the sensitivity of the sensor by increasing the redox-reaction probability and creating an even smaller confinement for the reactant in the nanometer range. The results shown in this chapter were obtained in part by Melina Becker during the direct supervision of her Bachelor thesis [105]. The flexibility was pursued to transfer the sensor array from a rigid glass substrate to a polymer-based, insulating substrate, with principal implantability requirements in mind.

4.5.1 Sensitivity improvement by NSL

Initially, the spheres were deposited either directly on top of the top electrode already etched free of SiN_x or on top of the final passivation layer. The latter did not produce a single working sensor, which might be founded in the process steps of etching the final passivation first and thereby damaging the passivation of the top electrode towards the bottom electrode in the following etch processes of RIE and IBE. Distribution of particles however did not show any significant deviation.

For the creation of hexagonally close-packed (HCP) monolayers of particles on the sensor surface, the PS-NS were distributed in various wt% concentrations by the techniques of spin coating and a modified version of AWISA (chapter 2.6 and 3.3.1). For spin coating, parameters like rotation speed in rounds-per-second (rps) were modified to find the most suitable combination.

At low concentrations and deposition by spin coating, all particle types showed a quite homogenous distribution. With increased concentration and rotation speed, a specific distribution pattern as well as surface-binding behavior could be observed and was expected. Carboxylate-coated PS-NS deposited in a net-like structure, left large areas uncovered but created locally satisfactory HCP monolayers at 33 rps and 10 wt% concentration (Figure 85a). Sulfate-coated NS in ethanol showed a high affinity to each other and assembled in clusters in every concentration and rotation speed and were excluded. Amino-coated NS formed large areas of HCP monolayers at 17 rps and 5 wt% concentration (Figure 85b) and generally showed

the best results in regard to reproducibility and stability of particle distribution as well as a continuous surface coverage with few multilayered areas. Hydroxylate PS-NS performed best at 17 rps and 5 wt% concentration, but still created clusters and multilayers and at the same time uncovered areas at sufficiently high concentrations and where thus excluded also.

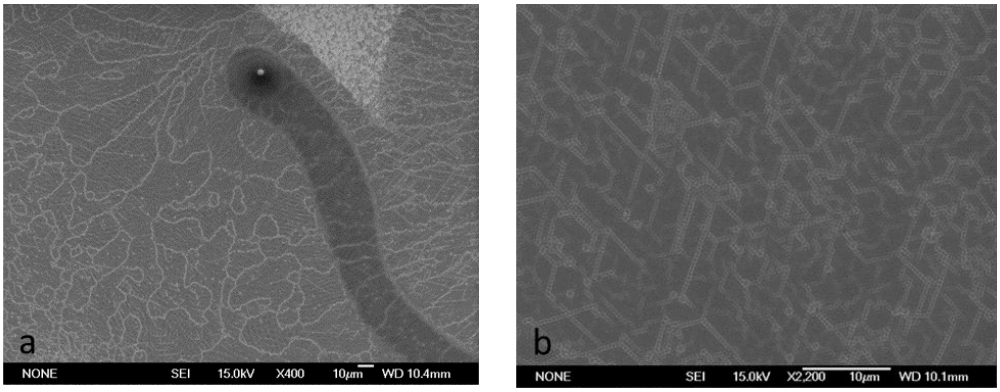

Figure 85: SEM images of particle distribution via spin coating. a) Carboxylate-NS at 33 rps and 10 wt%, b) Amino-coated NS at 17 rps and 5 wt% showing dense HCP monolayers. Images by Melina Becker.

For the modified AWISA deposition method, carboxylate-, hydroxylate- and amino-coated PS-NS were tested in various concentrations. Concentrations of 1.25 and 2.5 wt% were generally too low to create HCP monolayers. For this self-assembly technique, the particle concentration proved to be more difficult to optimize, since low concentrations could not create HCP monolayers and higher concentrations created multilayers easily. For carboxylate-coated NS both concentrations of 5 and 10 wt% could not produce a uniform distribution. Amino-coated NS created large areas of HCP monolayers at a concentration of 10 wt%, still leaving uncovered areas in a small ratio. The increase of concentration to 15 wt% proved to be difficult to handle with particles agglomerating in solution, which was overcome by intense resuspension of particles and freshly prepared solution for each deposition. Figure 86 shows the results for the 15 wt% concentration on a test substrate of discarded regular electrode arrays, used for NS coating tests, and containing pores in the top electrode. The Hydroxylate PS-NS could not produce a uniform monolayer without multilayers and agglomerated particles by AWISA too and were excluded also.

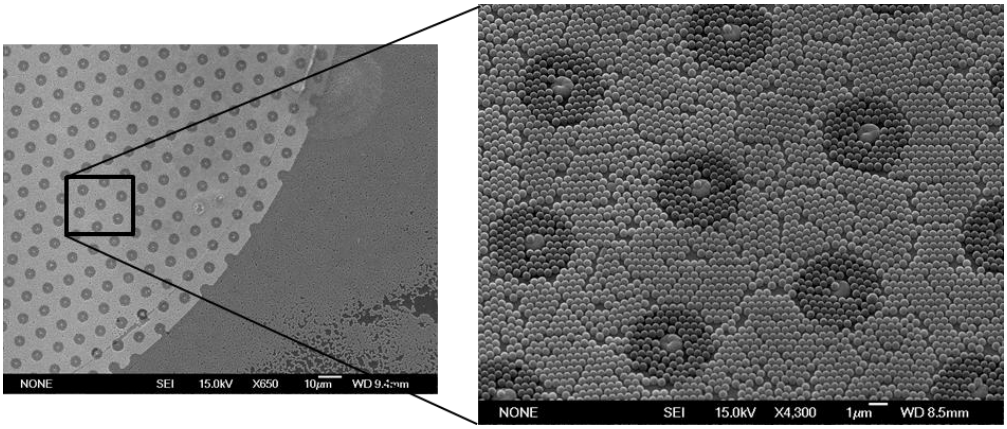

Figure 86: SEM images of modified AWISA with amino-coated PS-NS in 15 wt% concentration, deposited on a regular electrode array containing pores in the top electrode. Images by Melina Becker.

The experimental determination of the most suitable particle coating yielded the amino-coated PS-NS for both, spin coating and the AWISA. The amino-groups provide a polarity with fewer electrons in the functional group compared to sulphate-groups, thus not needing a cationic balance and being able to form hydrogen bonds. This reaction is more likely than one of sulphate with hydrogen to sulphuric acid. The transfer to ethanol as solvent was necessary to ensure fast solvent evaporation for spin coating and self-assembly, even though a change in characteristics such as solubility or interaction of functional groups can occur and influence the range of solubility for higher concentrations.

Both deposition techniques achieved similar results, with spin coating being generally more stable, controllable and thus reproducible than the modified AWISA technique. HCP monolayers could be achieved with both techniques over a limited area, with AWISA covering nearly every available space on the surface due to the uniform spreading and initially higher amount of deposited solution. For both deposition techniques, the area of interest is limited to the electrode surfaces in the micrometer scale and with large surface areas to be covered, the inhomogeneity and number of defect structures increases. Environmental conditions like temperature and air-flow can influence the particle deposition as well.

Once the particles were successfully deposited in a HCP monolayer on the electrode surfaces, the reduction of the sphere diameter was done by RIE in order to increase the space between particles, which later creates sufficient distance between the pores and allows for smaller pore diameters. For the parameters described in chapter 3.3.1 the etch rates are given in Table 5.

Table 6 lists the actual reduction in diameter with regard to the initial particle size, which was different for the various surface coatings, for the first 100 seconds of oxygen plasma RIE.

Table 5: Etch-rate of carboxylate-PS-NS by O_2 plasma

Etching time [s]	NS diameter [nm]
0	492
30	455
60	424
90	351
120	323
150	275

Table 6: Particle diameter reduction by RIE of various PS-particles in nm.

Etch Time [s]	Carboxylate PS-NS Diameter Midpoint [nm] Standard Deviation	Hydroxylate PS-NS Diameter Midpoint [nm] Standard Deviation	Amino PS-NS Diameter Midpoint [nm] Standard Deviation
0	500 8	461 17	467 29
90	387 11	325 8	325 8
90+10	312 14	224 20	189 23

A reaction time of 90 seconds proved to be sufficient to create adequate space between particles and the deposition of 100 nm chromium as sacrificial etch layer and mask followed.

The particle removal by MIBK in combination with ultrasonification was only partly successful, since the NS could not be completely removed and tended to remain in the chromium layer at the rim of initially deposited particle solution or on areas of multilayer formation. Since the particle dissolution by MIBK can only take place when the polystyrene is in direct contact with the solvent, the particle diameter and the layer thickness of chromium had to be matched. This resulted in a maximum layer thickness of 100 nm for the sacrificial etch layer. Since only the electrode surface areas were of interest, the remaining particles would not be etched and did not encumber the progress.

The etch success for the pore construction by RIE and IBE could not be verified satisfactorily by optical microscopy and SEM imaging, since the various layers of electrodes and passivation could not be distinguished. The SEM images in Figure 87 show the particle distribution by spin coating and the pore construction. The etch success however could only be confirmed by electrochemical measurements.

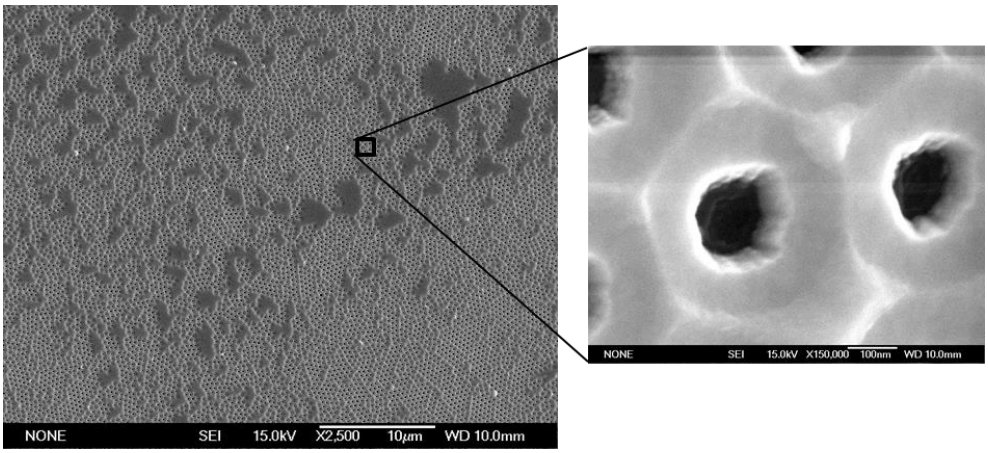

Figure 87: SEM image of nanopore distribution on top electrode and IBE success in pore production after 50 minutes. Images by Melina Becker.

Figure 88 and Figure 89 show the distribution of pores by spin coating and AWISA exemplary on electrodes without the alignment gap correction. The surfaces are covered with pores, in case of the large electrode in Figure 88 with a median diameter of 202 nm and only few areas remaining uncovered. The nanopore production by AWISA deposition, displayed in Figure 89 a and b, optically differs from these produced by spin coating, as pores often were much smaller with a median diameter of 141 nm. Many particles could not be removed or multilayers produced larger defect areas by taking away not only the nanospheres but also the surrounding chromium, leaving the surface unprotected during the IBE and RIE.

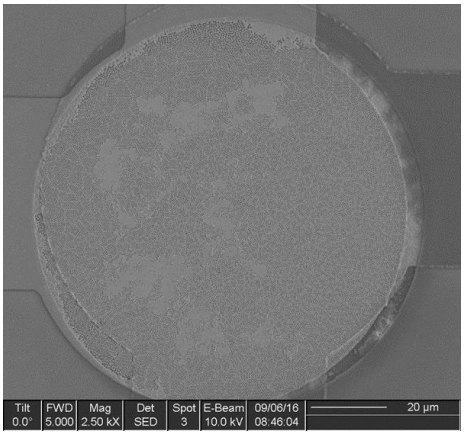

Figure 88: Nanopores produced by spin-coating deposition technique on a small electrode. Areas with pores and uncovered areas are present, alignment error clearly visible. Image by Melina Becker.

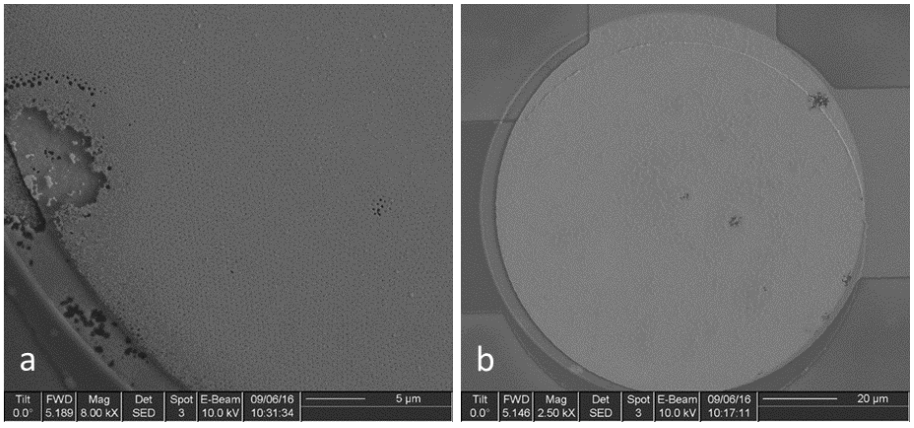

Figure 89: Nanopores produced by AWISA deposition technique on a) large electrode, b) small electrode. Areas with multilayer defects and alignment error clearly visible. Images by Melina Becker.

The design variation for the sensors produced by NSL described in chapter 3.3 became necessary because of the more intensive RIE, which was needed to completely open the smaller nanopore structures and which opened not only the desired pores to the bottom electrode but also the sides of the top electrodes, where the alignment with the bottom electrode did not completely overlap. This created an increased surface area for the redox reaction, if the bottom part of the electrode is exposed also and lead to a significantly higher reaction rate which distorted the measurement and was successfully overcome by the smaller top electrode design displayed in the optical image in Figure 90.

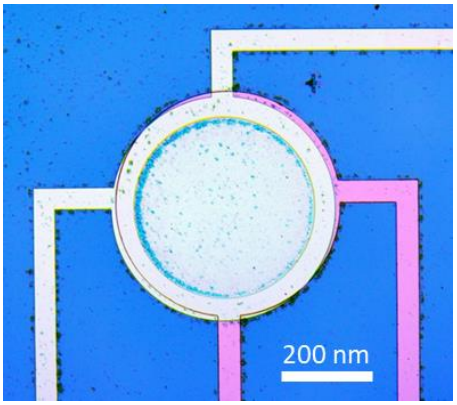

Figure 90: Optical image of large electrode with alignment gap correction by reduced top electrode diameter and nanopores.

Atomic force microscopy was taken into account for the analysis of the etch progression of the pore but could not be applied here, since the cantilever-tip would have been too large for the nanopore and not been able to reach the bottom of the pore without contact to the pore walls. The pore production and etch progress was therefore tested by electrochemical measurements via cycling either bottom or top electrode over the potential range from -0.4 to 0.7 V, while the respective partnering electrode is set to the fixed oxidation or reduction potential as described for the standard sensor in chapter 4.3.1.

The following graphs display the voltammetric current flow for the reduced form of hexacyanoferrate(II) on the sensor array modified by NSL (red) via spin-coating deposition, versus a standard design (black), with alignment gap correction, exemplary for large electrodes and the 4 electrode combinations.

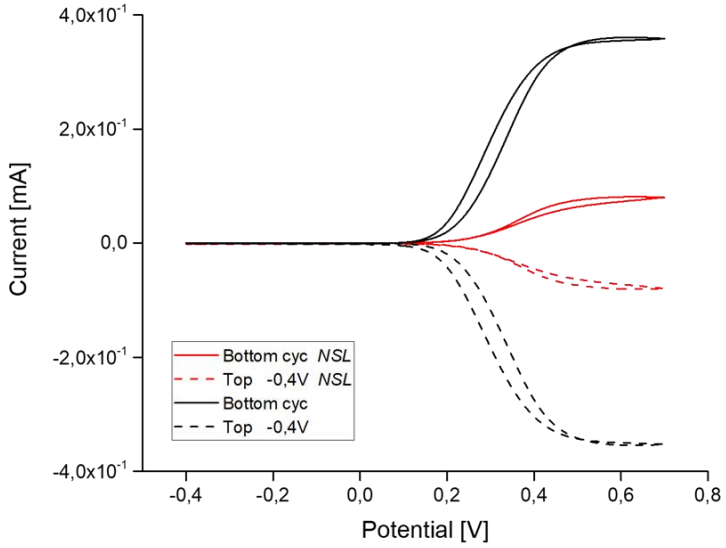

Figure 91: Redox current in 0.2 mol/l hexacyanoferrate(II), NSL vs. standard: Bottom electrode cycling (solid lines), top electrode at fixed reduction potential -0.4 V (dashed lines), scan rate 0.2 V/s.

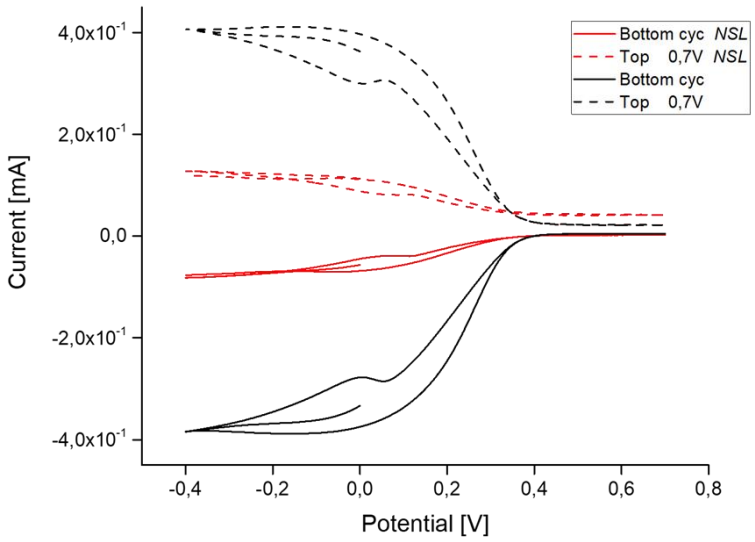

Figure 92: Redox current in 0.2 mol/l hexacyanoferrate(II), NSL vs. standard: Bottom electrode cycling (solid lines), top electrode at fixed oxidation potential 0.7 V (dashed lines), scan rate 0.2 V/s.

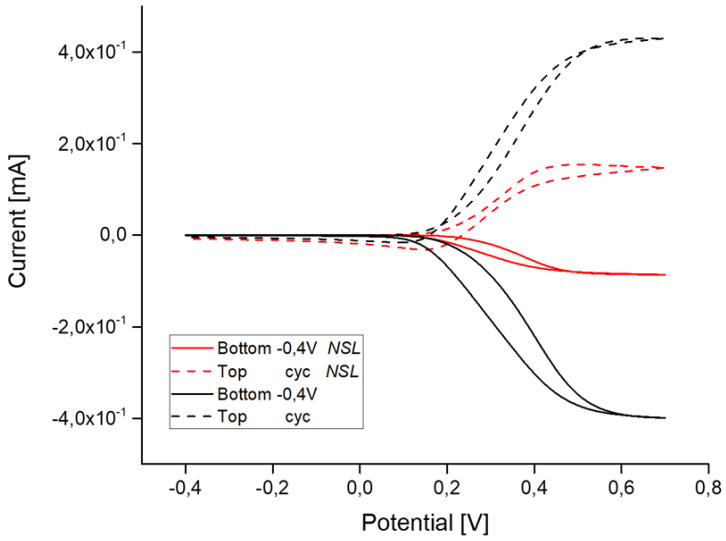

Figure 93: Redox current in 0.2 mol/l hexacyanoferrate(II), NSL vs. standard: Top electrode cycling (dashed lines), bottom electrode at fixed reduction potential -0.4 V (solid lines), scan rate 0.2 V/s.

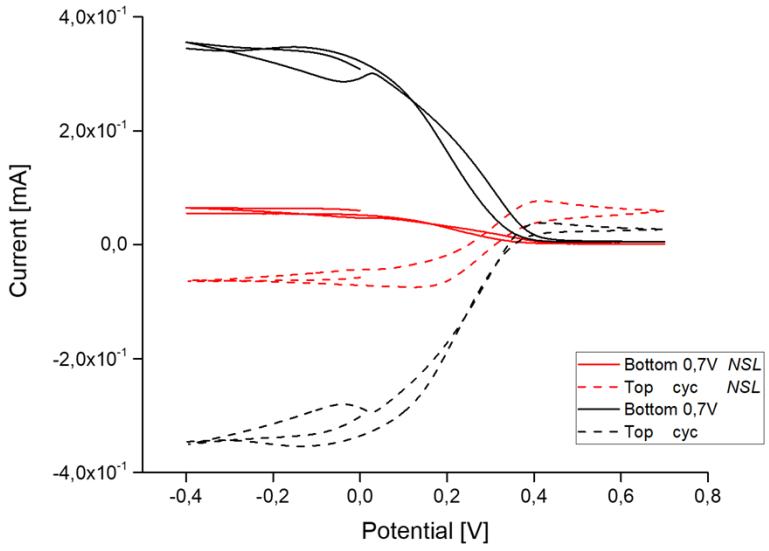

Figure 94: Redox current in 0.2 mol/l hexacyanoferrate(II), NSL vs. standard: Top electrode cycling (dashed lines), bottom electrode at fixed oxidation potential 0.7 V (solid lines), scan rate 0.2 V/s.

The performance of the standard sensor design can be characterized as identical to the performance described in chapter 4.3.1, with equal current for the oxidation and reduction at bottom and top electrode and a high efficiency. The electrodes produced by NSL show a consistently lower current yield for all electrode settings in comparison to the standard design. Both half-reactions of the redox process can be measured and current at bottom and top electrode is present in equal amount, which affirms the etch success in creating a nanopore

down to the surface of the bottom electrode. The efficiency seems to be very high, with only slightly more current produced by the top electrode when in cycling mode and the bottom electrode at the reduction potential (Figure 93). The consistently lower current produced by redox reactions on the nanopore-sensor electrodes was not expected, since the intention was an increase in sensitivity by decreasing the pore size and thus raise the probability of redox reactions of analyte molecules at the electrode surfaces. This outcome could be explained with a significantly reduced reactive surface area of the electrodes due to re-deposition of material in the physical etching process and the creation of micromasks, like described for SiN_x in chapter 2.5.4. The smaller diameter of the pore makes the evacuation of previously ablated material out of the pore more difficult. Although the IBE has a very high resolution [88], the consecutive etching by RIE and IBE may lead to redeposition and significant reduction of free electrode surface area. The consistently lower current is reflected throughout all tested electrodes and displayed in Table 7 in absolute current values for each electrode size exemplary and for the bottom and top electrode.

Table 7: Redox current values of nanopore electrodes vs. standard electrodes at 0.6 V for cycling and -0.4 V as reduction potential in mA.

Electrode setting	Large NSL	Large standard	Medium NSL	Medium standard	Small NSL	Small standard
Bottom cyc	0,07654	0,38340	0,02108	0,10080	0,00552	0,01691
Top 0.7 V	0,11910	0,40670	0,02995	0,10910	0,00808	0,01932
Bottom cyc	0,08112	0,36060	0,02082	0,09868	0,00581	0,01693
Top -0.4 V	0,08001	0,35380	0,02033	0,09654	0,00559	0,01637
Top cyc	0,05516	0,34610	0,02000	0,09486	9,079E-5	0,01641
Bottom 0.7 V	0,06228	0,34450	0,02100	0,09447	9,992E-5	0,01613
Top cyc	0,08541	0,42650	0,02178	0,10360	0,00350	0,01722
Bottom -0.4 V	0,15140	0,39140	0,03317	0,11470	0,00268	0,02023

Although the sensitivity could not be improved by the modification of the standard sensor design by NSL, the production process yielded working electrodes with nanopores.

4.5.2 Flexible Sensor Array

The results shown in this chapter were obtained in part by Fabienne Röschel during the direct supervision of her practical work experience [106].

The process described in section 3.3 and 3.3.2 allowed the production of a stable working flexible electrode array using Polyimide as substrate, passivation and insulation.

The PI 2610 polyimide layer thickness was verified for rotation speeds and time by surface profile measurements using a *Dektak 3030ST* Auto Surface Texture Profiler. For PI 2611 the manufacturer`s specifications were adopted. For each setting used, the thickness can be seen in Table 8.

Table 8: Polyimide Thickness

Polyimide Product	Rotation speed [rpm]	Spin Time [s]	Thickness [nm]
PI 2610	3000	90	~ 1260
PI 2610	9999	90	~ 460
PI 2611	3000	90	~ 6000 [HD Microsystems]
PI 2611	9999	90	< 4000 [HD Microsystems]

Since the inter-electrode spacing was desired to be as small as possible, polyimide 2610 was used at the highest rotation speed for 90 seconds, resulting in an electrode spacing of approximately 460 nm. In RIE tests of the two polyimides, the PI 2610 proved to be more quickly to etch and easier to be removed from the structure than the PI 2611. Therefore, it was used for the final passivation layer, while PI 2611 was used as the bottom layer.

Figure 95 shows an optical image of a medium-sized electrode. The top electrode opening is of reduced diameter to avoid the alignment gap error, the electrode surface and pores are etched free of PI and the rim as well as the feedlines are covered by transparent PI passivation.

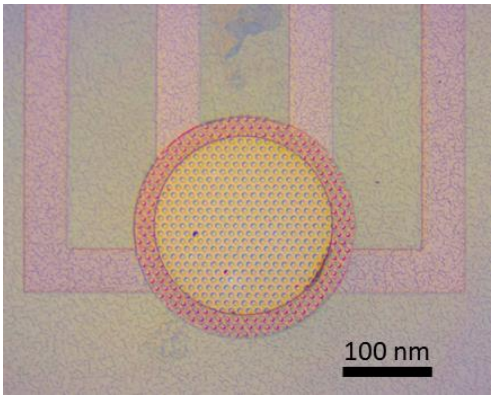

Figure 95: Medium-sized electrode on flexible substrate, top electrode and pores open (yellow), rim of top electrode and feedlines covered by PI (pink).

The evaluation of the sensor array was done by electrochemical measurements as described in sections 3.2.1 and 3.3.2 as well as by Helium Ion Microscopy (HIM), using the *Zeiss Orion Nanofab* microscope by LISA$^+$. The measurements were performed on single electrode pairs while the sensor is still attached to the glass substrate, thus in a planar position.

The following graphs show the cyclic voltammograms for the 2 electrode combinations for cycling and the reductive potential only, as well as the amperometric curves on 0,2 mol/l potassium hexacyanoferrate(II) exemplary for a medium-sized electrode of a flexible sensor (red) in comparison to a standard, non-flexible sensor of the original design (black), also with reduced diameter top electrode.

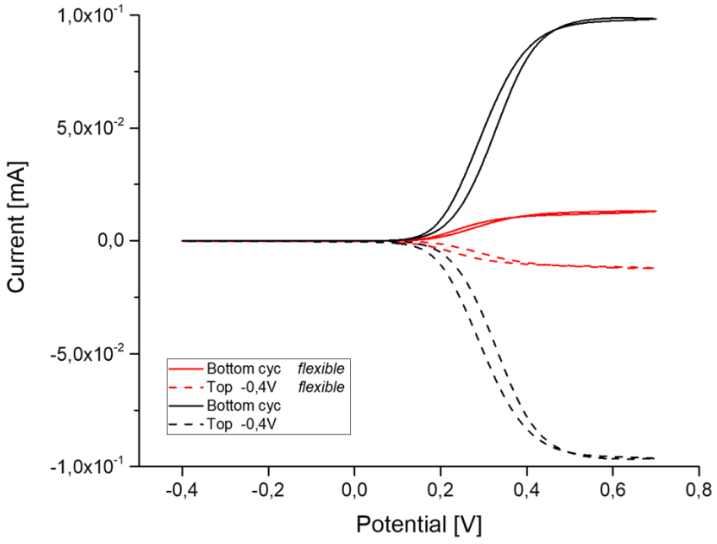

Figure 96: Redox current in 0.2 mol/l hexacyanoferrate(II): Flexible sensor array (red) vs. standard array (black), medium-sized electrode. Bottom electrode cycling, (solid lines), top electrode at fixed reduction potential -0.4 V (dashed lines), scan rate 0.2 V/s.

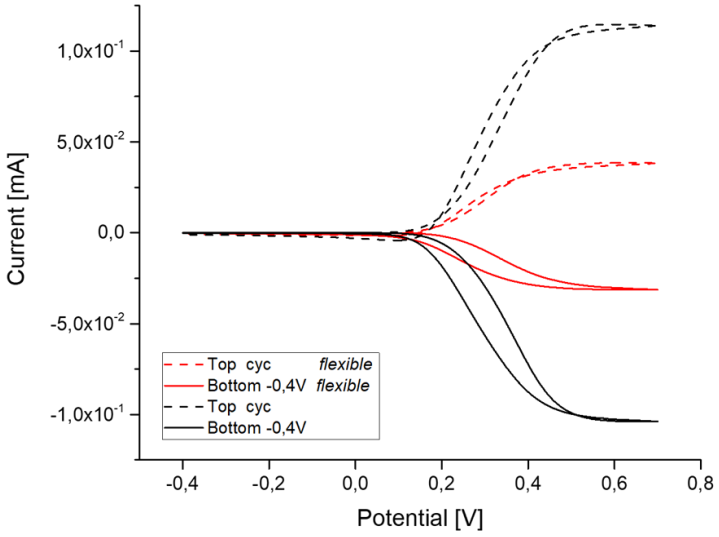

Figure 97: Redox current in 0.2 mol/l hexacyanoferrate(II): Flexible sensor array (red) vs. standard array (black), medium-sized electrode. Top electrode cycling, (dashed lines), bottom electrode at fixed reduction potential -0.4 V (solid lines), scan rate 0.2 V/s.

The current created on the flexible sensor electrode is significantly lower than that of a standard sensor with SiN_x passivation. Redox cycling is functionally possible and both half reactions are of the same amount and thus show the high efficiency of the designed sensor. The sensitivity is much lower for the flexible sensor array, which is also confirmed in amperometric measurements in Figure 98 and Figure 99 with both redox potentials tested for the bottom and top electrode respectively.

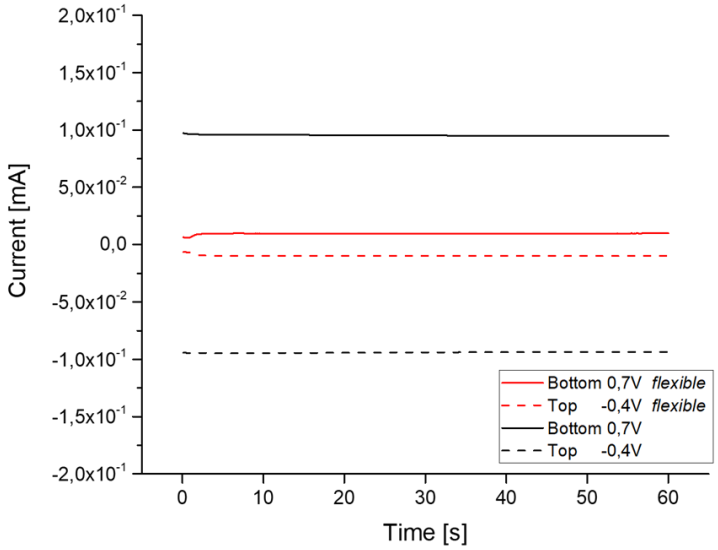

Figure 98: Amperometric measurement in 0.2 mol/l hexacyanoferrate(II): Flexible sensor array (red) vs. standard array (black), medium-sized electrode. Bottom electrode set to oxidative potential 0.7 V (solid lines), top electrode set to reductive potential -0.4 V (dashed lines).

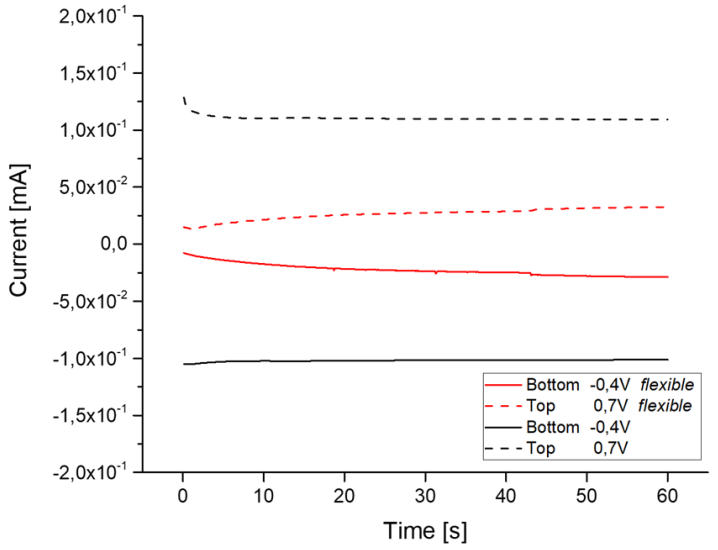

Figure 99: Amperometric measurement in 0.2 mol/l hexacyanoferrate(II): Flexible sensor array (red) vs. standard array (black), medium-sized electrode. Bottom electrode set to reductive potential -0.4 V (solid lines), top electrode set to oxidative potential 0.7 V (dashed lines).

Figure 99 shows a slightly higher current for the top electrode on the oxidation and the bottom electrode at the reduction potential. This can be explained by the size difference of the top and bottom electrode, that provides a higher surface area for the oxidation by the top electrode and thus more oxidized molecules to be reduced at the bottom electrode. The slight increase in current over time at the electrode on the flexible sensor is surprising, since the

establishing of a depletion zone in the proximity of the electrode surface and loss of created oxidized molecules to the bulk would indicate a decrease of current over time.

HIM imaging of the electrode surfaces was done to investigate the condition of the surface area, which is shown in Figure 100.

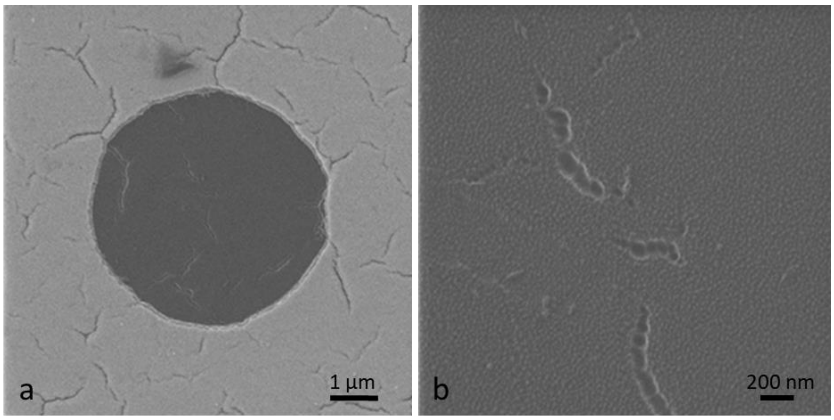

Figure 100: HIM images of flexible sensor electrode pore. a) Pore with top electrode structure, b) Bottom electrode surface inside a pore. Images taken by Markus Turad of LISA⁺.

The image of the top electrode reveals cracks in the surface and polymer residue on the bottom of the pore, covering the metal of the bottom electrode. This is explained by the RIE process using oxygen plasma on polyimide, where a residue of carbonized polymer is created as a form of RIE grass [107]–[109]. A removal of these residues was not possible by prolonged etching. This explaines the decrease in current, since the residue decreases the reactive surface area of the bottom and top electrode, which results in fewer electron transfer reactions with the hexacyanoferrate(II) molecules.

Figure 101 shows the detachment of the flexible sensor array from the glass substrate using adhesion tape. The edges of the substrate were cleaned from excessive polyimide, which was simply peeled off, and an adhesive tape was attached to one side of the sensor and used to peel back the layer structure. Afterwards, the sensor was cut to size (Figure 102).

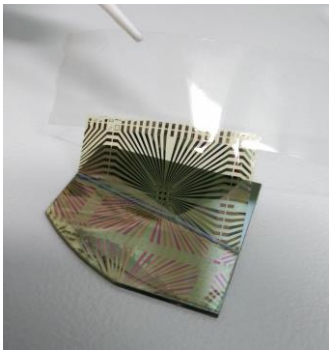

Figure 101: Detachment of a flexible sensor array from glass substrate by adhesion tape

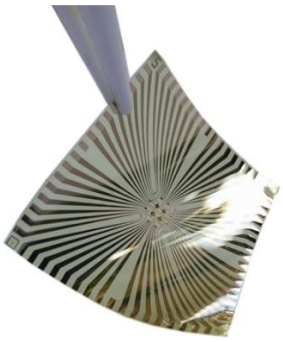

Figure 102: Flexible redox-sensor array, edge length 24.2 mm.

The flexible sensor was again tested by electrochemical measurements as described above. The following graphs show the cyclic voltammograms for the 2 electrode combinations for cycling and the reductive potential only, as well as the amperometric curves on 0.2 mol/l potassium hexacyanoferrate(II) exemplary for a medium-sized electrode of a detached flexible sensor (blue) in comparison to the flexible planar sensor prior to the detachment (red).

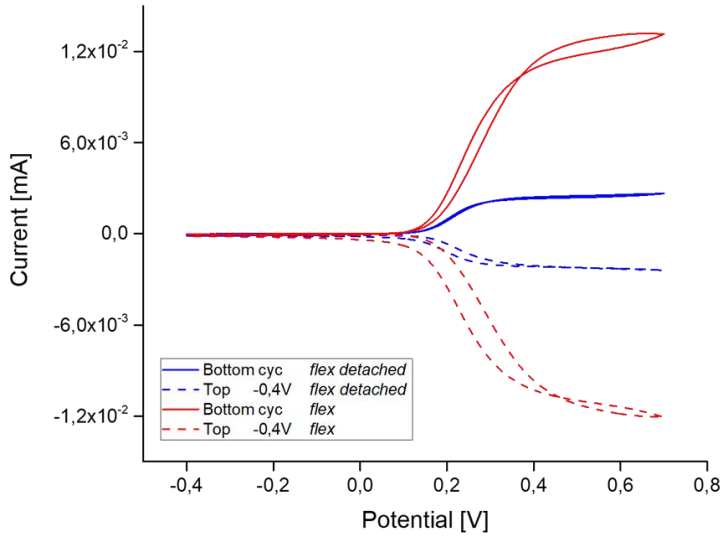

Figure 103: Redox current in 0.2 mol/l hexacyanoferrate(II): Flexible sensor array (red) vs. detached flexible array (blue), medium-sized electrode. Bottom electrode cycling, (solid lines), top electrode at fixed reduction potential -0.4 V (dashed lines), scan rate 0.2 V/s.

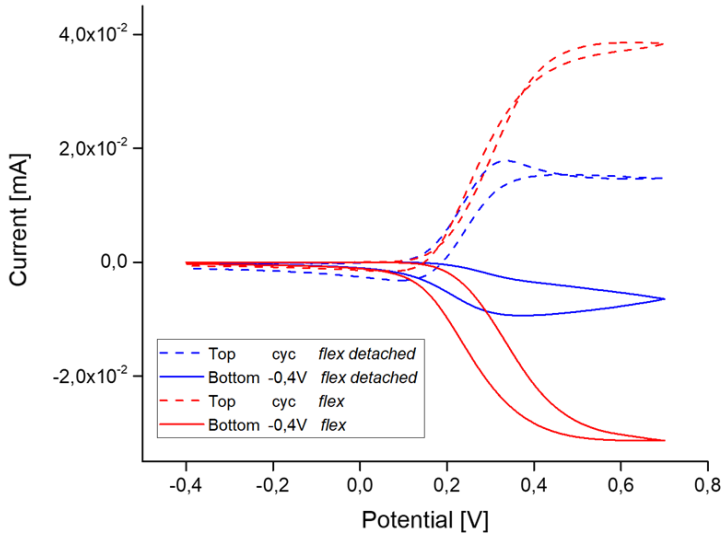

Figure 104: Redox current in 0.2 mol/l hexacyanoferrate(II): Flexible sensor array (red) vs. detached flexible array (blue), medium-sized electrode. Top electrode cycling, (dashed lines), bottom electrode at fixed reduction potential -0.4 V (solid lines), scan rate 0.2 V/s.

The detached flexible sensor is also functioning properly, showing the redox current as before detachment. Nevertheless, the current yield after detachment of the sensor array is decreased even further. This might be caused by changes in the thin metal structure due to bending and tearing during the detachment and is also visible in the amperometric comparison in Figure 105 and Figure 106. An increased electrical resistivity in conductive material is known to be

caused by the formation of micro-cracks due to mechanical stress as well as tensile stress, which can cause plastic rearrangement of grains and even grain growth on the nanoscale level [110].

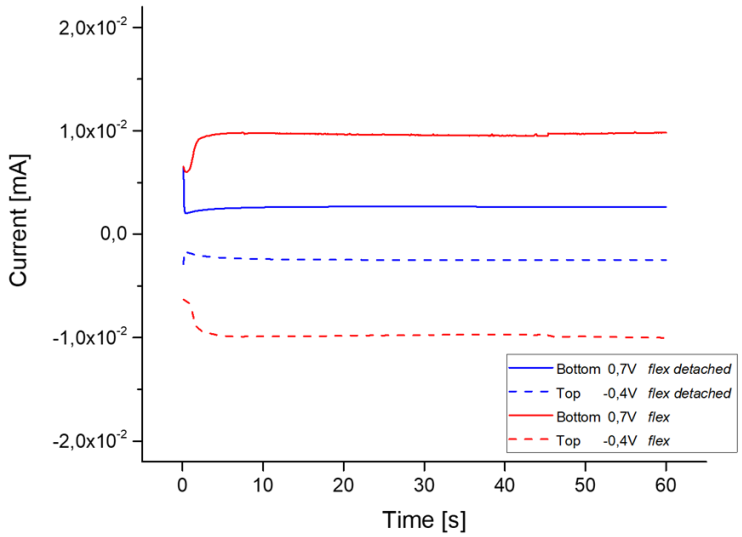

Figure 105: Amperometric measurement in 0.2 mol/l hexacyanoferrate(II): Flexible sensor array (red) vs. detached flexible array (blue), medium-sized electrode. Bottom electrode set to oxidative potential 0.7 V (solid lines), top electrode set to reductive potential -0.4 V (dashed lines).

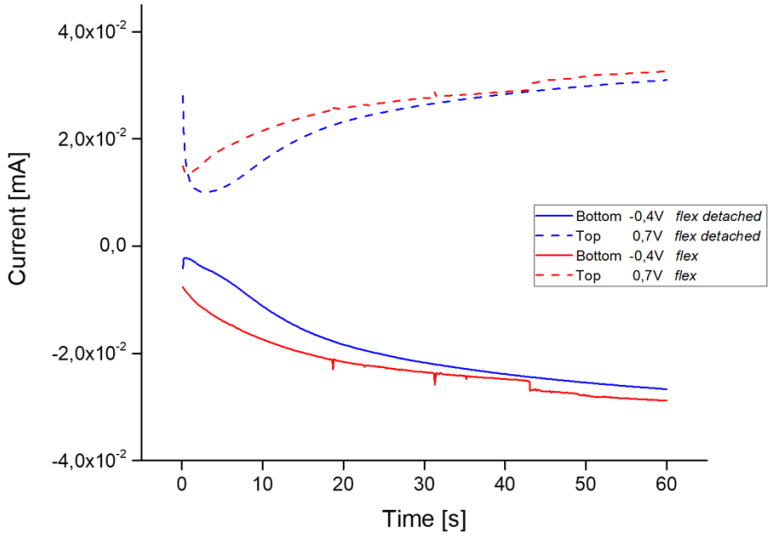

Figure 106: Amperometric measurement in 0.2 mol/l hexacyanoferrate(II): Flexible sensor array (red) vs. detached flexible array (blue), medium-sized electrode. Bottom electrode set to reductive potential -0.4 V (solid lines), top electrode set to oxidative potential 0.7 V (dashed lines).

Figure 106 shows again an increase of current over the time of 60 seconds for the top electrode as the generating and the bottom as the collecting electrode.

4.6 Desorption of DAQ

The adsorption and desorption of DAQ onto unprotected gold electrodes and the loss of sensitivity by electrode fouling, as described in chapter 2.2.1, was investigated by prolonged and repeated amperometric measurements with the standard sensor array. Therefore, the potential was alternated from 0.6 V oxidation potential to -0.1 V reduction potential repeatedly, with a delay of several seconds between switches where no potential was applied. The intention was to initiate a reverse adhesion reaction at the reduction potential and transfer the adsorbed DAQ back to a soluble state.

The stability of dopamine in solution is limited to a short time frame, since the initial concentration is reduced by steady natural oxidation of dopamine in solution. Therefore, the measurement time-frame was limited to < 10 minutes.

Figure 107 shows the current at a medium-sized top electrode for 1 µmol/l dopamine in 0.01 mol/l PBS at 3 measurements with 0.6 V oxidation potential. The interjected potential switches to -0.1 V are not shown and were done for the equal time frame of 60 seconds. Arrows indicate the start of the consecutive oxidation potential.

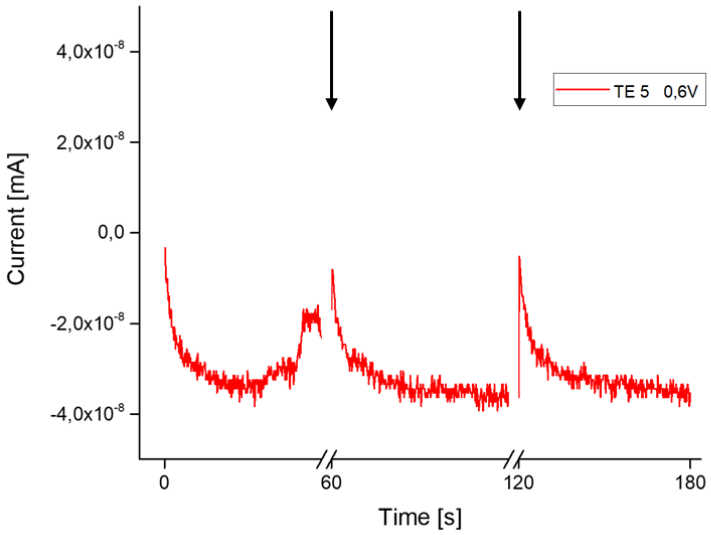

Figure 107: Amperometric measurements of repeated oxidation current at a medium-sized top electrode set to 0.6 V in 1 µmol/l dopamine in PBS.

The same measurement was repeated for a concentration of 10 µmol/l dopamine in PBS and is shown in Figure 108.

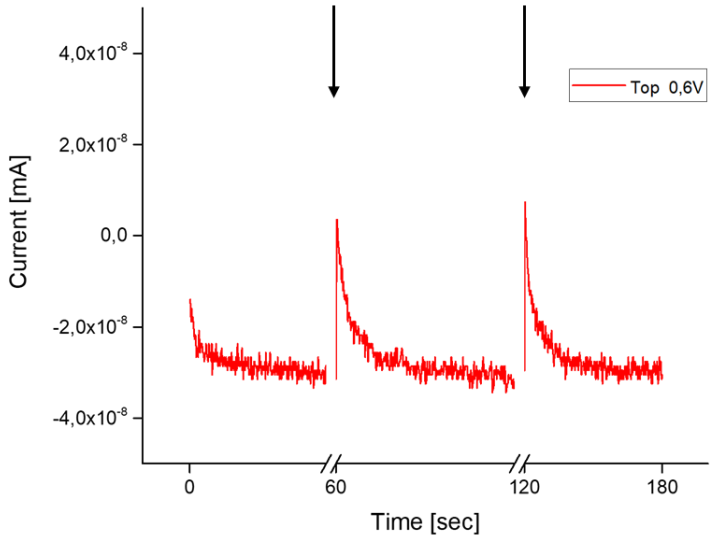

Figure 108: Amperometric measurements of repeated oxidation current at a medium-sized top electrode set to 0.6 V in 10 µmol/l dopamine in PBS.

For both concentrations, the second and third oxidation current reaches the same level as before, 30 seconds into the measurement interval. This shows that the reaction rate for 1 and 10 µmol/l dopamine concentration is the same and no electrode fouling can be detected with this short time interval and the small dopamine concentration. At this concentration, the current induced is in the range of 10^{-11} A and the background noise is visible. The concentration was increased to 1 mmol/l dopamine in PBS and prolonged measurements with several potential switches were tested.

Figure 109 shows the current at 1 mmol/l dopamine in 0.01 mol/l PBS at 6 measurements with 0.6 V oxidation potential. The first 2 intervals were 180 seconds each, the following intervals were 60 seconds long. The interjected potential switches to -0.1 V are again not shown and were done for the equal time frame. Arrows indicate the start of the consecutive oxidation potential.

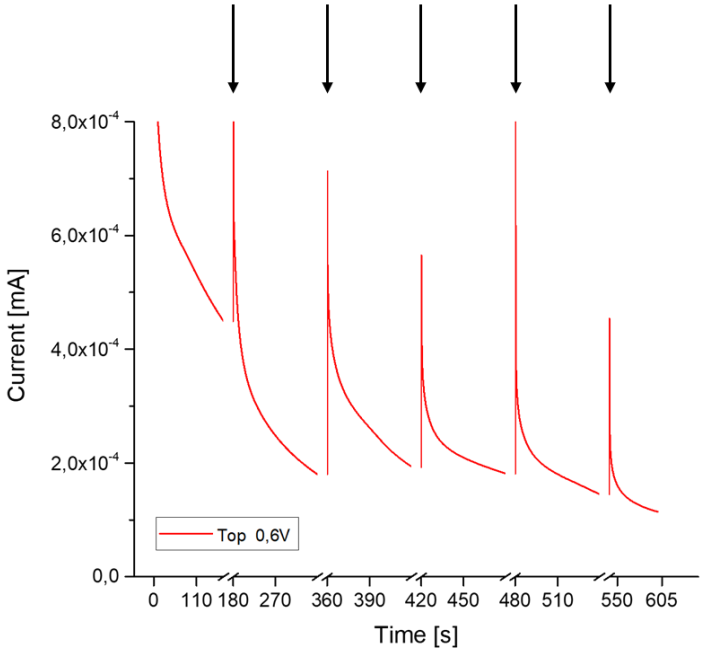

Figure 109: Amperometric measurements of repeated oxidation current at a medium-sized top electrode set to 0.6 V in 1 mmol/l dopamine in PBS.

At the concentration of 1 mmol/l dopamine in PBS, a constant decrease in current is visible during the first oxidation reactions. After the reduction reaction at the electrode (not shown) and a switch back to the oxidation potential, the current decreases further but starts initially at a higher level. This can be explained with the creation of a local concentration of reductive molecules due to the reversal of the potential. Right after the potential switch the number of reduced molecules is highest near the electrode surface and results in the initially higher current after the electrical double-layer formation. Nevertheless, the current at the electrode decreases over several oxidation periods with the concentration of 1 mmol/l dopamine, which constitutes a decrease in sensitivity or electrode fouling and a desorption could not be initiated.

5 Conclusions

The development of electrochemical sensors for sensing of dopamine was successfully achieved in this thesis. This chapter contains the assessment of the presented results.

The design of the sensor on the basis of a MEA proved to be convenient and feasible for the production of working sensor arrays. Central electrode positioning, shape and dimensions, pore size and a layout for batch processing allowed a fairly efficient production of the sensor by microtechnological methods, once the procedural obstacles were overcome.

The chosen materials and techniques, in combination with the design, allowed the successful production of working redox-sensor arrays with closely spaced electrodes in a 3-dimensional arrangement. The construction of pore channels between the electrodes with a 5 µm diameter proved to be an effective method to increase the top electrode surface area and at the same time provide spatial confinement for the redox-active molecules to enhance the sensitivity and efficiency of the sensor. The functionality of the designed sensor could successfully be established in electrochemical measurements of cyclic voltammetry and amperometry, where the 3D electrode arrangement and pore-channel effect on the redox-cycling of potassium hexacyanoferrate(II) was reflected in a variation of the generated oxidation and reduction current. A very high cycling efficiency for the bottom electrode set to the generating and the top electrode to the collecting potential for oxidation and reduction reactions could be confirmed. Next to the geometry-effect of the pore channel, a size-effect could be shown for the 3 electrode sizes of 500, 250 and 100 µm electrode diameter, which resulted in a size-dependent redox-current. The concentration-dependent sensitivity to redox-active molecules was investigated for a one-electron transfer reaction down to 1 mmol/l potassium hexacyanoferrate(II) and clearly showed the concentrations reflected in the redox current. Generally, a very high cycling efficiency in the range of 84 to 99 % could be established, with the electrode size reflected again and the best results achieved by the large electrodes for the inter-electrode passivation of 400 nm. The decreased inter-electrode distance of 300 nm even showed a cycling efficiency on a large electrode of 100 % for 0.01 and 0.05 mol/l potassium hexacyanoferrate(II). The main source of error was found to be the alignment error between the bottom and top electrode, resulting in a significant deviation of reactive surface area for the electrodes and thus a varying performance for electrodes of the same size, with the large electrode showing the lowest and the small electrode the largest alignment errors. This made

a significant comparison of the performance of same-sized electrodes unfeasible and the main systematic error overshadows the systematic measurement errors of setup and solution preparation.

The established fluidic setup allowed the successful performance of amperometric redox-measurements on dopamine in solution, provoking an immediate reaction to changes in the presence of dopamine molecules at the electrodes. The detection limit for the sensor array in the fluidic measurement was found to be 10 µmol/l dopamine in PBS solution. Despite the flux of fluid over the electrode array and the obvious flushing of the pore, the detection of previously generated, oxidized molecules from the bottom at the top electrode was measurable in reduction current, which proved the fluidic measurements as feasible despite the lack of complete control over the fluid flow by the control unit.

The cultivation of dopamine-releasing PC12 cells on the sensor arrays could successfully be established and allowed the in-vitro detection of physiological dopamine by amperometric measurements. A homogenous and dense cell layer could not be established over the complete electrode array, which made a comparison between currents of same-sized electrodes unfeasible due to the variation in cell concentration on different electrodes and the resulting variation in locally released dopamine molecules. Despite the unfavorable conditions during the measurement, the dopamine release could be induced by KCl as well as dopamine in solution and the redox current could be recorded for the physiological dopamine concentration as well as an L-Dopa-augmented concentration by loading the PC12 cells with the precursor for dopamine. The developed sensor allows the distinction between KCl-induced and dopamine-induced dopamine release in the reflected redox current as well as the measurement in cultivation medium. In addition, the repeated dopamine release by PC12 cells could be recorded also. The concentration-dependence as well as the electrode-size-dependence of the redox current was reflected again in the in-vitro measurements.

A modification by nanosphere lithography allowed the successful sensor production in a complicated top-down micro- and nano-technological production process by performing several intricate consecutive process steps and severe etching processes. The NSL could successfully be applied after a functioning surface coating of the spheres was determined and the deposition was successfully established, resulting in close-packed monolayers on the top electrodes of the standard sensor array. The deposition of amino-coated polystyrene

nanospheres by spin-coating yielded favorable results compared to the interface self-assembly method. RIE and IBE could effectively be adapted for the creation of nanopores with median diameters between 202 and 141 nm. After the alignment error was eliminated by a reduced diameter of the top electrode, electrochemical measurements successfully showed the creation of nanopores in electrochemical measurements and the creation of working nanopore-electrodes could be confirmed in redox cycling measurements. However, the sensitivity of the sensor array could not be increased compared to the standard design and all working nanopore-electrodes showed a significant decrease in redox current yield. Since the increase in sensitivity has been generally proven for nanopore designs, these results are attributed to the production process and likely an unseen reduction in reactive surface area of the electrodes.

The sensor modification towards a flexible sensor array was successfully accomplished by the substitution of the rigid silicon nitrate with flexible polyimide as substrate and passivation material. The production processes for the standard electrode array could effectively be adapted to the polymer, which resulted in working sensor arrays with open pores in the top electrode, an inter-electrode distance of approximately 460 nm and a functional passivation of the electrodes. Electrochemical measurements confirmed the working design and successfully showed the redox reactions on potassium hexacyanoferrate(II) solution in voltammetric as well as amperometric measurements. The redox current yield however was significantly decreased compared to the rigid standard design, which was attributed to the RIE process of polyimide. The oxygen-based RIE of polyimide covers the electrode surface with a polymer residue, which cannot be removed afterwards and effectively decreases the reactive electrode surface area. After the detachment from the carrier glass wafer further electrochemical measurements confirmed the lasting stability of the flexible passivation but showed even further reduction of the redox current yield. This change is assumed to be caused by an increased resistance in the conductive material due to mechanical and tensile stress, induced by the detachment process.

The known adhesion of oxidized dopamine derivatives on gold electrodes could not be shown with the designed sensor array on medium-sized top electrodes for dopamine concentrations of 1 and 10 µmol/l. At an increased concentration of 1 mmol/l dopamine in PBS the decrease in sensitivity could be observed but not reversed by a repetitive potential switch from oxidizing to reductive potential.

In conclusion, the successful production of a pore-based redox-cycling sensor with an inter-electrode distance of 300 – 400 nm is possible and allows a sensitive and effective detection of dopamine in solution as well as in physiological secretion. The established sensor represents a progress in design and development towards a closed-loop stimulation and detection system for the possible application in DBS.

6 Outlook

Based on the accomplished status and results in this thesis, this chapter gives a prospective outlook on future developments and modifications of the established sensor array.

Since the quality of micromechanical processes not only depends on experience and professional knowledge, but also a state-of-the art cleanroom environment and technology, the developed sensor array would greatly profit from production at industry production standards. The preliminary prototypes produced at the University of Tübingen already achieved a remarkable efficiency, which could be further increased by the elimination of such nuisances like alignment errors and non-uniform illumination due to technological limitations. With this, a closer electrode positioning, smaller than 300 nm inter-electrode distance, should be possible, which should increase the efficiency and thus sensitivity in redox cycling measurements and could generally result in more stable and durable arrays.

As for the materials chosen, implantability and biocompatibility have been kept in mind even for the non-flexible prototype sensor array. In the past years, amorphous silicon carbide (SiC) has been investigated as an insulation material as well as an adhesion promotor in micromechanical technology and as an implantable coating. SiC can be deposited by PECVD and has been found to be more stable than Si_3N_4 as well as biocompatible [111] and could further enhance the stability of the sensor array if used as passivation material.

In order to evaluate the sensor performance and to show the induced redox-cycling current the electrochemical measurements were done so far with only one redox-active substance present at a time. In physiological conditions, more than one redox-active substance is present, like other catecholamine neurotransmitters or ascorbic acid, which can be oxidized. Therefore, further measurements should be conducted with more than one electroactive substance present in order to investigate the possibility of filtering the current of interest by selecting a potential range or fast cycling times.

With regard to in-vitro measurements, the prolonged testing of the sensor with repeated measurements could be performed with the cell or tissue culture in a cell observer unit, where the array would be kept in physiological culture conditions for dopaminergic cell culture or tissue slices. Here, an electrical stimulation via the top electrode could be tested as well.

To enhance the sensor sensitivity by nanosphere lithography, the deposition of nanospheres could be achieved more stable and reproductive by use of the Langmuir-Blodgett enhanced dip-coating technique, where the nanospheres are forced to form a monolayer on an air-liquid interface and are transferred to an immersed solid substrate.

The flexible sensor array based on polyimide is mainly impeded by the RIE process to selectively remove the polyimide. The RIE process is well suited for bulk structuring of polyimide but has to be adjusted and perfected in order to eliminate the carbonized residue, which can be achieved by an oxygen - sulfur hexafluoride (SF_6) gas combination with the corresponding settings [107]. Further, the poor adhesion of polyimide to metal and glass could be overcome by PECVD SiC, which has been shown to be a very good adhesion promotor for polymers [112], [113].

The electrode fouling due to adhesion of oxidized dopamine derivatives like dopaminechrome has been a consisting problem for unprotected gold electrodes in electrochemical dopamine detection and is the reason for extensive research in electrode coatings for implantable gold electrodes. The electrically-induced reversal of the adhesive reaction with a resulting desorption of the polymer deposit should further be pursued, since it might solve the electrode fouling for implanted gold electrodes.

With the discussed refinements in mind, the designed sensor can be combined with the established design of DBS electrodes and thus lead to a closed-loop system of neurotransmitter detection and regulated stimulation. Such a concentration-dependent stimulation method would further improve the therapeutic success of DBS in Parkinson`s desease, depression and related deseases and simultaneously become a tool for general monitoring of the electroactive brain chemistry and advance the knowledge of brain function.

7 References

[1] E. Zrenner, “The subretinal implant: can microphotodiode arrays replace degenerated retinal photoreceptors to restore vision?,” *Ophthalmologica*, vol. 216, no. Suppl. 1, pp. 8–20, 2002.

[2] W. F. House and J. Urban, “Long term results of electrode implantation and electronic stimulation of the cochlea in man,” *Ann. Otol. Rhinol. Laryngol.*, vol. 82, no. 4, pp. 504–517, 1973.

[3] A. Schrag, M. Jahanshahi, and N. Quinn, “What contributes to quality of life in patients with Parkinson Disease?,” *J. Neurol. Neurosurg. Psychiatry*, vol. 69, pp. 308–312, 2000.

[4] S. K. Van Den Eeden, C. M. Tanner, A. L. Bernstein, R. D. Fross, A. Leimpeter, D. A. Bloch, and L. M. Nelson, “Incidence of Parkinson’s disease: variation by age, gender, and race/ethnicity,” *Am. J. Epidemiol.*, vol. 157, no. 11, pp. 1015–1022, 2003.

[5] J. T. Coyle, M. L. Leski, J. H. Morrison, K. L. Davis, D. Charney, and C. Nemeroff, “Neuropsychopharmacology: the fifth generation of progress,” *ACNP, Nahv.*, p. 13571366, 2002.

[6] M. K. Zachek, A. Hermans, R. M. Wightman, and G. S. Mccarty, “Electrochemical Dopamine Detection: Comparing Gold and Carbon Fiber Microelectrodes using Background Subtracted Fast Scan Cyclic Voltammetry,” vol. 614, no. 919, pp. 113–120, 2009.

[7] T. James, M. S. Mannoor, and D. V. Ivanov, “BioMEMS - Advancing the frontiers of medicine,” *Sensors*, vol. 8, no. 9, pp. 6077–6107, 2008.

[8] S.-Y. Chang, I. Kim, M. P. Marsh, D. P. Jang, S.-C. Hwang, J. J. Van Gompel, S. J. Goerss, C. J. Kimble, K. E. Bennet, P. a Garris, C. D. Blaha, and K. H. Lee, “Wireless fast-scan cyclic voltammetry to monitor adenosine in patients with essential tremor during deep brain stimulation.,” *Mayo Clin. Proc.*, vol. 87, no. 8, pp. 760–5, Aug. 2012.

[9] P. J. Grahn, G. W. Mallory, O. U. Khurram, B. M. Berry, J. T. Hachmann, A. J. Bieber, K. E. Bennet, H. K. Min, S. Y. Chang, K. H. Lee, and J. L. Lujan, “A neurochemical closed-loop controller for deep brain stimulation: Toward individualized smart neuromodulation therapies,” *Front. Neurosci.*, vol. 8, no. 8 JUN, pp. 1–11, 2014.

[10] R. S. Shah, B. Sc, S. Chang, and H. Min, “Deep Brain Stimulation : Technology at the Cutting Edge DBS for Psychiatric Disorders,” pp. 167–182, 2010.

[11] “Morbus Parkinson aktuell,” 2017. [Online]. Available: https://www.morbus-parkinson-aktuell.de/. [Accessed: 12-Jun-2017].

[12] J. Parkinson, “An essay on shaking palsy. Sherwood, Neeley and Jones.” London, 1817.

[13] S. Fahn, “Description of Parkinson’s disease as a clinical syndrome,” *Ann. N. Y. Acad. Sci.*, vol. 991, no. 1, pp. 1–14, 2003.

[14] M. C. Rodriguez-Oroz, M. Jahanshahi, P. Krack, I. Litvan, R. Macias, E. Bezard, and J. A. Obeso, “Initial clinical manifestations of Parkinson’s disease: features and pathophysiological mechanisms,” *Lancet Neurol.*, vol. 8, no. 12, pp. 1128–1139, 2009.

[15] J. M. Shulman, P. L. De Jager, and M. B. Feany, “Parkinson’s Disease: Genetics and Pathogenesis,” *Annu. Rev. Pathol. Mech. Dis.*, vol. 6, no. 1, pp. 193–222, 2011.

[16] J. W. Langston, “The Parkinson’s complex: Parkinsonism is just the tip of the Iceberg,” *Ann. Neurol.*, vol. 59, no. 4, pp. 591–596, 2006.

[17] M. A. Hely, J. G. L. Morris, W. G. J. Reid, and R. Trafficante, “Sydney Multicenter Study of Parkinson’s disease: Non-L-dopa-responsive problems dominate at 15 years,” *Mov. Disord.*, vol. 20, no. 2, pp. 190–199, 2005.

[18] ResearchGate, “Deep Brain Stimulation.” [Online]. Available: https://www.researchgate.net/figure/51696122_fig2_Figure-4-Deep-brain-stimulation-DBSDownload-Power-Point-slide-264-KB. [Accessed: 14-Jul-2017].

[19] S. Miocinovic, S. Somayajula, S. Chitnis, and J. L. Vitek, “History, Applications, and Mechanisms of Deep Brain Stimulation,” *JAMA Neurol.*, vol. 70, no. 2, p. 163, 2013.

[20] R. Kumar, A. M. Lozano, Y. J. Kim, W. D. Hutchison, and E. Sime, “Double-blind evaluation of subthalarnic nucleus deep brain stimulation in advanced Parkinson ’ s disease Completion of Diaries,” *Neurology*, 1998.

[21] R. Kumar, A. E. Lang, M. C. Rodriguez-Oroz, A. M. Lozano, P. Limousin, P. Pollak, A. L. Benabid, J. Guridi, E. Ramos, C. van der Linden, A. Vandewalle, J. Caemaert, E. Lannoo, D. van den Abbeele, G. Vingerhoets, M. Wolters, and J. A. Obeso, “Deep brain stimulation of the globus pallidus pars interna in advanced Parkinson’s disease,” *Neurology*, vol. 55, no. 12 Suppl 6, p. S34—9, 2000.

[22] N. P. Odekerken V J, Laar T van, Staal MJ, Mosch A, Hoffmann CF, V. J. J. Odekerken, T. van Laar, M. J. Staal, A. Mosch, C. F. E. Hoffmann, P. C. G. Nijssen, G. N. Beute, J. P. P. van Vugt, M. W. P. M. Lenders, and M. F. Contarino, “Subthalamic nucleus versus globus pallidus bilateral deep brain stimulation for advanced Parkinson’s disease (NSTAPS study): a randomised controlled trial,” *Lancet Neurol*, vol. 12, no. 1, pp. 37–44, 2013.

[23] Y. Koike, F. Shima, A. Nakamizo, and Y. Miyagi, “Direct localization of subthalamic nucleus supplemented by single-track electrophysiological guidance in deep brain stimulation lead implantation: Techniques and clinical results,” *Stereotact. Funct. Neurosurg.*, vol. 86, no. 3, pp. 173–178, 2008.

[24] M. Shin, J. P. Lefaucheur, M. F. Penholate, P. Brugières, J. M. Gurruchaga, and J. P. Nguyen, “Subthalamic nucleus stimulation in Parkinson’s disease: Postoperative CT-MRI fusion images confirm accuracy of electrode placement using intraoperative multi-unit recording,” *Neurophysiol. Clin.*, vol. 37, no. 6, pp. 457–466, 2007.

[25] D. K. Binder, G. M. Rau, and P. A. Starr, “Hemorrhagic Complications of Microelectrode-Guided Deep Brain Stimulation,” *Stereotact. Funct. Neurosurg.*, vol. 80, pp. 28–31, 2003.

[26] M. L. S. Bezerra, J. V. L. Martínez, and J. A. Nasser, “‘Transient acute depression induced by high-frequency deep-brain stimulation’: Comment.,” *The New England Journal of Medicine*, vol. 341, no. 13. Massachusetts Medical Society, US, p. 1003, 1999.

[27] M. D. Johnson, J. L. Vitek, and C. C. McIntyre, “Pallidal stimulation that improves parkinsonian motor symptoms also modulates neuronal firing patterns in primary motor cortex in the MPTP-treated monkey,” *Exp. Neurol.*, vol. 219, no. 1, pp. 359–362,

2009.

[28] C. R. Butson and C. C. McIntyre, “Current steering to control the volume of tissue activated during deep brain stimulation,” *Brain Stimul.*, vol. 1, no. 1, pp. 7–15, 2008.

[29] P. Hickey and M. Stacy, “Deep brain stimulation: A paradigm shifting approach to treat Parkinson’s disease,” *Front. Neurosci.*, vol. 10, no. APR, pp. 1–11, 2016.

[30] P. E. Holtzheimer and H. S. Mayberg, “Deep Brain Stimulation for Psychiatric Disorders,” *Annu. Rev. Neurosci.*, vol. 34, no. 1, pp. 289–307, 2011.

[31] R. Fisher, V. Salanova, and T. Witt, “Electrical stimulation of the anterior nucleus of thalamus for treatment of refractory epilepsy,” *Epilepsia*, vol. 51, no. 5, pp. 899–908, 2010.

[32] B. Jenkins and S. J. Tepper, “Neurostimulation for primary headache disorders: Part 2, review of central neurostimulators for primary headache, overall therapeutic efficacy, safety, cost, patient selection, and future research in headache neuromodulation,” *Headache*, vol. 51, no. 9, pp. 1408–1418, 2011.

[33] S. A. Shah and N. D. Schiff, “Central thalamic deep brain stimulation for cognitive neuromodulation - a review of proposed mechanisms and investigational studies,” *Eur. J. Neurosci.*, vol. 32, no. 7, pp. 1135–1144, 2010.

[34] E. Pothos, M. Desmond, and D. Sulzer, “L-3,4-dihydroxyphenylalanine increases the quantal size of exocytotic dopamine release in vitro.,” *J. Neurochem.*, vol. 66, no. 2, pp. 629–36, 1996.

[35] P. B. Molinoff and J. Axelrod, “BIOCHEMISTRY OF CATECHOLAMINESl,” 1971.

[36] B. Zhang, M. L. A. V Heien, M. F. Santillo, L. Mellander, and A. G. Ewing, “Temporal resolution in electrochemical imaging on single PC12 cells using amperometry and voltammetry at microelectrode Arrays,” *Anal. Chem.*, vol. 83, no. 2, pp. 571–577, 2011.

[37] B. Falkenburger, “Freisetzung von Dopamin aus Dendriten dopaminerger Neurone der Substantia nigra durch den Dopamin-Transporter,” 2002.

[38] N. K. Speed, “The Role of Insulin Signaling on Dopamine Transporter Trafficking,” *J. Chem. Inf. Model.*, vol. 53, no. 9, pp. 1689–1699, 2013.

[39] M. J. Berridge, “Neuronal Signalling,” *Cell Signal. Biol.*, pp. 1–91, 2009.

[40] R. N. Sternson, A.W. McCreery, R., Feinberg, B., Adams, “Electrochemical Studies of Adrenergic Neurotransmitters and Related Compounds,” *Electroanal. Chem. Interfacial Electrochem.*, vol. 46, pp. 313–321, 1973.

[41] Y. Li, M. Liu, C. Xiang, Q. Xie, and S. Yao, “Electrochemical quartz crystal microbalance study on growth and property of the polymer deposit at gold electrodes during oxidation of dopamine in aqueous solutions,” *Thin Solid Films*, vol. 497, no. 1–2, pp. 270–278, 2006.

[42] J. O. Zerbino and M. G. Sustersic, “Ellipsometric and Electrochemical Study of Dopamine Adsorbed on Gold Electrodes,” vol. 15, no. 24, pp. 7477–7481, 2000.

[43] S. Galan, “Klinische und Molekulargenetische Charakterisierung von Phäochromozytomen und Paragangliomen,” Philipps-Universität Marburg, 2012.

[44] R. H. S. Westerink and A. G. Ewing, “The PC12 cell as model for neurosecretion,” pp. 273–285, 2008.

[45] W. A. M. Hijnen, E. F. Beerendonk, and G. J. Medema, “Inactivation credit of UV radiation for viruses, bacteria and protozoan (oo)cysts in water: A review,” *Water Res.*, vol. 40, no. 1, pp. 3–22, 2006.

[46] R. Neumeier, E. Substrats, and A. Der Blutzellen, “Zell-Adhasion und Wachstumskontrolle,” no. 2, pp. 33–38, 1983.

[47] Schmitz S., *Der Experimentator Zellkultur*. 2011.

[48] E. Yavin, “Attachment and Culture of Dissociated Cells From Rat Embryo Cerebral Hemispheres on Polylysine-Coated Surface,” *J. Cell Biol.*, vol. 62, no. 2, pp. 540–546, 1974.

[49] L. R. Bard, A. J., Faulkner, *Electrochemical Methods Fundamentals and Applications*, vol. 8, no. c. John Wiley & Sons, Inc., 2001.

[50] E. Kätelhön, “Fluidic Redox Cycling Diplomarbeit in Physik,” Forschungszentrum Jülich, 2009.

[51] C. G. Zoski, Ed., *Handbook of Electrochemistry*. Elsevier.

[52] G. L. Gouy, “J. de Phys. 9, 457 (1910); DL Chapman,” *Phil. Mag*, vol. 25, p. 475, 1913.

[53] O. Z. Stern, “No Title,” *Electrochem*, vol. 30, 1924.

[54] J. O. Howell and R. M. Wightman, “Ultrafast voltammetry and voltammetry in highly resistive solutions with microvoltammetric electrodes,” *Anal. Chem.*, vol. 56, no. 3, pp. 524–529, 1984.

[55] C. Amatore, E. Maisonhaute, and G. Simonneau, “Ultrafast cyclic voltammetry: Performing in the few megavolts per second range without ohmic drop,” *Electrochem. commun.*, vol. 2, no. 2, pp. 81–84, 2000.

[56] E. Kätelhön and B. Wolfrum, “On-chip redox cycling techniques for electrochemical detection,” *Rev. Anal. Chem.*, vol. 31, no. 1, pp. 7–14, Jan. 2012.

[57] F.-R. F. Fan and A. J. Bard, “Electrochemical Detection of Single Molecules,” *Science (80-.).*, vol. 267, no. 5199, pp. 871–874, 1995.

[58] A. J. Bard, J. a. Crayston, G. P. Kittlesen, T. Varco Shea, and M. S. Wrighton, “Digital simulation of the measured electrochemical response of reversible redox couples at microelectrode arrays: consequences arising from closely spaced ultramicroelectrodes,” *Anal. Chem.*, vol. 58, no. 11, pp. 2321–2331, 1986.

[59] J. E. A. Thomas, “A Miniature Microelectrode Array to Monitor the Biolectric Activity of Cultured Cells,” *Exp. Cell Res.*, vol. 74, no. 972, pp. 61–66, 1972.

[60] M. Taketani and M. Baudry, *Advances in network electrophysiology*. Springer, 2010.

[61] P. Tomčík, M. Krajčíková, and D. Bustin, “Determination of pharmaceutical dosage forms via diffusion layer titration at an interdigitated microelectrode array,” *Talanta*, vol. 55, no. 6, pp. 1065–1070, 2001.

[62] “multichannel systems MCS.” [Online]. Available: http://www.multichannelsystems.com/. [Accessed: 01-Jul-2017].

[63] C. Hassler, T. Boretius, and T. Stieglitz, “Polymers for neural implants,” *J. Polym. Sci. Part B Polym. Phys.*, vol. 49, no. 1, pp. 18–33, 2011.

[64] K. Molina-Luna, M. M. Buitrago, B. Hertler, M. Schubring, F. Haiss, W. Nisch, J. B. Schulz, and A. R. Luft, “Cortical stimulation mapping using epidurally implanted thin-film microelectrode arrays,” *J. Neurosci. Methods*, vol. 161, no. 1, pp. 118–125, 2007.

[65] multichannel systems GmbH, “FlexMEA36,” *data sheet*, 2013. [Online]. Available: http://www.multichannelsystems.com/sites/multichannelsystems.com/files/documents/data_sheets/FlexMEA36_Layout.pdf. [Accessed: 02-Jul-2017].

[66] J. Pan, R. M. Pafchek, F. F. Judd, and J. B. Baxter, “Effect of chromium–gold and titanium–titanium nitride–platinum–gold metallization on wire/ribbon bondability,” *IEEE Trans. Adv. Packag.*, vol. 29, no. 4, pp. 707–713, 2006.

[67] V. K. Khanna, “Adhesion–delamination phenomena at the surfaces and interfaces in microelectronics and MEMS structures and packaged devices,” *J. Phys. D. Appl. Phys.*, vol. 44, no. 3, p. 34004, 2011.

[68] G. Voskerician, M. S. Shive, R. S. Shawgo, H. Von Recum, J. M. Anderson, M. J. Cima, and R. Langer, “Biocompatibility and biofouling of MEMS drug delivery devices,” *Biomaterials*, vol. 24, no. 11, pp. 1959–1967, 2003.

[69] “Material Property Database.” [Online]. Available: http://www.mit.edu/~6.777/matprops/matprops.htm. [Accessed: 03-Jul-2017].

[70] L. Zhang, F. Cosandey, R. Persaud, and T. E. Madey, “Initial growth and morphology of thin Au films on TiO/sub 2/(110),” *Surf. Sci.*, vol. 439, pp. 73–85, 1999.

[71] L. Zhang, R. Persaud, and T. E. Madey, “Ultrathin metal films on a metal oxide surface: Growth of Au on TiO2,” *Phys. Rev. B*, vol. 56, no. 16, pp. 549–557, 1997.

[72] F. Silly and M. R. Castell, “Bimodal growth of Au on SrTiO3(001),” *Phys. Rev. Lett.*, vol. 96, no. 8, pp. 3–6, 2006.

[73] M. Zinke-Allmang, L. C. Feldman, and M. H. Grabow, “Clustering on surfaces,” *Surf. Sci. Rep.*, vol. 16, no. 8, pp. 377–463, 1992.

[74] Y. Q. Xue, M. Z. Zhao, and W. P. Lai, “Size-dependent phase transition temperatures of dispersed systems,” *Phys. B Condens. Matter*, vol. 408, no. 1, pp. 134–139, 2013.

[75] H. O. Pierson, W. A. Publishing, and N. York, *Handbook of Chemical Vapor Deposition*, no. Cvd. 1999.

[76] A. Stoffel, A. Kovács, W. Kronast, and B. Müller, “LPCVD against PECVD for micromechanical applications,” *J. Micromechanics Microengineering*, vol. 6, no. 1, pp. 1–13, 1996.

[77] Y. Kuo, “Reactive Ion Etching of PECVD Amorphous Silicon and Silicon Nitride Thin Films with Fluorocarbon Gases,” *J. Electrochem. Soc.*, vol. 137, no. 4, p. 1235, 1990.

[78] W. T. Gmbh and C. Charakterisierung, “Sicherheitsdatenblatt TechniEtch 01,” no. 1907, pp. 2–10, 2010.

[79] Microchemicals GmbH, “Chromium Etching,” 2013. [Online]. Available: http://www.microchemicals.eu/technical_information/chromium_etching.pdf. [Accessed: 05-Jul-2017].

[80] P. Details, A. A. Promoter, and A. P. Precursor, “PI-2600 Series – Low Stress Applications,” *Stress Int. J. Biol. Stress*, no. September, pp. 1–4, 2009.

[81] B. Schultrich, “Korpuskularstrahlen in Forschung und Praxis,” *Vak. Forsch. und Prax. Sonderausgabe Dünnschichttechnologie Methoden und Verfahren*, vol. 2, 2016.

[82] U. Hilleringmann, “Mikrosystemtechnik Prozessschritte,” *Technol. Anwendungen Wiesbad. Teubner*, 2006.

[83] J. W. Coburn and H. F. Winters, “Plasma etching—A discussion of mechanisms,” *J. Vac. Sci. Technol.*, vol. 16, no. 2, pp. 391–403, 1979.

[84] H. Jansen, H. Gardeniers, and M. De Boer, “A survey on the reactive ion etching of silicon in microtechnology,” vol. 6, pp. 14–28, 1996.

[85] H. Jansen, M. de Boer, R. Legtenberg, and M. Elwenspoek, “The black silicon method: a universal method for determining the parameter setting of a fluorine-based reactive ion etcher in deep silicon trench etching with profile control,” *J. Micromechanics Microengineering*, vol. 5, no. 2, p. 115, 1995.

[86] PlasmaEtch, “What is Plasma Surface Activation?” [Online]. Available: http://www.plasmaetch.com/plasma-activation.php. [Accessed: 12-Jul-2017].

[87] A. U. Alam, M. M. R. Howlader, and M. J. Deen, “The effects of oxygen plasma and humidity on surface roughness, water contact angle and hardness of silicon, silicon dioxide and glass,” *J. Micromechanics Microengineering*, vol. 24, no. 3, p. 35010, 2014.

[88] A. N. Broers, W. W. Molzen, J. J. Cuomo, and N. D. Wittels, “Electron-beam fabrication of 80-A metal structures,” *Appl. Phys. Lett.*, vol. 29, no. 9, pp. 596–598, 1976.

[89] U. C. Fischer and H. P. Zingsheim, “Submicroscopic pattern replication with visible light,” *J. Vac. Sci. Technol.*, vol. 19, no. 4, pp. 881–885, 1981.

[90] T. Lohmüller, U. Müller, S. Breisch, W. Nisch, R. Rudorf, W. Schuhmann, S. Neugebauer, M. Kaczor, S. Linke, S. Lechner, J. Spatz, M. Stelzle, M. Ulrich, S. Breisch, W. Nisch, T. Lohm, R. Rudorf, W. Schuhmann, S. Neugebauer, M. Kaczor, S. Linke, S. Lechner, J. Spatz, and M. Stelzle, “Nano-porous electrode systems by colloidal lithography for sensitive electrochemical detection: fabrication technology and properties,” *J. Micromechanics Microengineering*, vol. 18, no. 11, p. 115011, 2008.

[91] P. Colson, C. Henrist, and R. Cloots, “Nanosphere lithography: A powerful method for the controlled manufacturing of nanomaterials,” *J. Nanomater.*, vol. 2013, 2013.

[92] R. Micheletto, H. Fukuda, and M. Ohtsu, “A Simple Method for the Production of a Two-Dimensional, Ordered Array of Small Latex Particles,” *Langmuir*, vol. 11, no. 9, pp. 3333–3336, 1995.

[93] P. a Kralchevsky and N. D. Denkov, “Capillary forces and structuring in layers of collid particles,” *Curr. Opin. Colloid Interface Sci.*, vol. 6, pp. 383–401, 2001.

[94] T. Laurvick, R. A. Coutu, and R. A. Lake, “Integrating nanosphere lithography in device

fabrication," in *Proc. SPIE*, 2016, vol. 9779, p. 97791S.

[95] J. Yu, Q. Yan, and D. Shen, "Co-Self-Assembly of Binary Colloidal Crystals at the Air−Water Interface," *ACS Appl. Mater. Interfaces*, vol. 2, no. 7, pp. 1922–1926, 2010.

[96] C. Geng, L. Zheng, J. Yu, Q. Yan, X. Wang, G. Shen, and D. Shen, "Monolayer colloidal mask with tunable interstice size for nanosphere lithography," *Thin Solid Films*, vol. 544, pp. 83–87, 2013.

[97] Fluigent GmbH, "Microfluidic Flow Control System." pp. 1–2, 2016.

[98] L. J. Lewis, P. Jensen, and J.-L. Barrat, "Melting, freezing, and coalescence of gold nanoclusters," *Phys. Rev. B*, vol. 56, no. 4, pp. 2248–2257, 1997.

[99] A. Einstein, "Die Ursache der Mäanderbildung der Flußläufe und des sogenannten Baerschen Gesetzes," *Naturwissenschaften*, no. 2, pp. 224–225, 1926.

[100] J. E. Baur and R. M. Wightman, "Diffusion-Coefficients Determined with Microelectrodes," *J. Electroanal. Chem.*, vol. 305, no. 1, pp. 73–81, 1991.

[101] R. Trouillon, Y. Lin, L. J. Mellander, J. D. Keighron, and A. G. Ewing, "Evaluating the diffusion coefficient of dopamine at the cell surface during amperometric detection: Disk vs ring microelectrodes," *Anal. Chem.*, vol. 85, no. 13, pp. 6421–6428, 2013.

[102] L. Bühler, "Establishment of a PC12 Cell Culture on Redox Cycling Sensors and Evaluation of Dopamine Release via Electrochemical Measurement," Eberhard-Karls Universität Tübingen, 2017.

[103] T. A. Mir, M. H. Akhtar, N. G. Gurudatt, J. I. Kim, C. S. Choi, and Y. B. Shim, "An Amperometric Nanobiosensor for the Selective Detection of K+-Induced Dopamine Released from Living Cells," *Biosens. Bioelectron.*, vol. 68, pp. 421–428, 2015.

[104] H.-F. F. Cui, J.-S. S. Ye, Y. Chen, S.-C. C. Chong, and F.-S. S. Sheu, "Microelectrode array biochip: tool for in vitro drug screening based on the detection of a drug effect on dopamine release from PC12 cells.," *Anal. Chem.*, vol. 78, no. 18, pp. 6347–6355, 2006.

[105] M. Becker, "Medical Sensor Improvement by Nanosphere Lithography," Eberhard-Karls Universität Tübingen, 2016.

[106] F. Röschel, "Transfer of Redox – Cycling – Array to Flexible Polyimide Substrate Report for Practical Work Experience," 2017.

[107] U. Buder, J. P. von Klitzing, and E. Obermeier, "Reactive ion etching for bulk structuring of polyimide," *Sensors Actuators, A Phys.*, vol. 132, no. 1 SPEC. ISS., pp. 393–399, 2006.

[108] A. Crockett, M. Almoustafa, and W. Vanderlinde, "Plasma delayering of integrated circuits," *Microelectron. Fail. Anal. Desk Ref.*, vol. 4, pp. 225–243, 2004.

[109] Y. L. Tsang, C. Miller, and T. Lii, "Investigation of polyimide residue due to reactive ion etching in O 2," *J. Electrochem. Soc.*, vol. 143, no. 4, pp. 1464–1469, 1996.

[110] J. R. Bautista, F. Avilés, A. I. Oliva, O. Ceh, and J. E. Corona, "Correlations between mechanical stress, electrical conductivity and nanostructure in Al films on a polymer substrate," *Mater. Charact.*, vol. 61, no. 3, pp. 325–329, 2010.

[111] S. F. Cogan, D. J. Edell, A. A. Guzelian, Y. Ping Liu, and R. Edell, "Plasma-enhanced

chemical vapor deposited silicon carbide as an implantable dielectric coating," *J. Biomed. Mater. Res.*, vol. 67A, no. 3, p. 856, 2003.

[112] J. Ordonez, M. Schuettler, C. Boehler, T. Boretius, and T. Stieglitz, "Thin films and microelectrode arrays for neuroprosthetics," *MRS Bull.*, vol. 37, no. 6, pp. 590–598, 2012.

[113] J. S. Ordonez, C. Boehler, M. Schuettler, and T. Stieglitz, "Long-term adhesion studies of polyimide to inorganic and metallic layers," *MRS Online Proc. Libr. Arch.*, vol. 1466, 2012.

List of Figures

List of Tables

Acknowledgments

For the support and motivation, I would like to thank all the people involved in this thesis work.

Prof. Dr. Boris Hofmann I would like to thank for the possibility to write my thesis in his workgroup with the Industry-On-Campus cooperation by B. Braun/Aesculap GmbH in Tuttlingen. I especially thank Prof. Hofmann for the excellent supervision, his patience and understanding as well as appreciation and the room to grow, which made working under his supervision a pleasure.

I would like to thank Prof. Dr. Tilman Schäffer for agreeing to be the second supervisor for this thesis, his interest in my work and the outstanding cooperation provided by his workgroup.

My colleague Markus Westerhausen I would like to thank dearly for his professional partnership, his support in trying times and the sharing of his knowledge in physics as well as the computational and technological assistance. It would not have been fun without you.

The Instrument Scientists Ronny Löffler, Markus Turad, Ralf Stiefel and Bertram Herzog I would like to thank for providing the excellent assistance in process technology, equipment operation and trouble-shooting as well as the sharing of their knowledge and experience to further the successful production.

Antje Treftz and Martin Ries and their teams I thank for the assistance in designing custom-made parts and for their production. The evaluation of my sensor was made possible by the flexibility and expert knowledge provided by the mechanical and electrical workshops.

My students, Yvonne Behres, Silje Völkerath, Melina Becker, Fabienne Röschel and Louisa Bühler I would like to thank for their dedication and determination to make this project a success. You let me grow as a supervisor and made the day-to-day work fun.